Discrete Shell Methods for Stimuli-Responsive and Deployable Structures: Buckling, Bistability, and Topology Optimization

Thesis by

Sathvik Sanagala

In Partial Fulfillment of the Requirements for the
Degree of
Doctor of Philosophy in Mechanical Engineering

Caltech

CALIFORNIA INSTITUTE OF TECHNOLOGY
Pasadena, California

2026
Defended May 29th, 2026

Sathvik Sanagala
ORCID: 0000-0002-7490-7540

ACKNOWLEDGEMENTS

This thesis is the culmination of my work at Caltech, and I could not have made it here without the support and influence of many people, and I am eternally grateful for them.

First, I wanted to sincerely thank my advisor, Kaushik Bhattacharya. It would be underselling to state that I learned a lot from him. Beyond just his knowledge and expertise, his ability to distill complex thoughts and mechanics into understandable concepts and ideas was something I constantly relied on and appreciated. He also displayed a high amount of patience with me, when I struggled. Beyond being an academic mentor, he is someone I look up to and respect for his attitude and outlook, and enjoyed when our meetings strayed from research, and turned into fun conversations about random topics, ranging from Indian food to career goals. I am extremely grateful for this experience he provided me, and how is a role model for me, both professionally and personally.

I am also grateful to my thesis committee members, Sergio Pelligrino, Ryan Watkins, and Angkur Shaikeea. I am grateful to Sergio for agreeing to be the chair of my thesis committee, and am excited to discuss much of my more recent research with him, as work done by his group serves as a foundation for much of my work, and was instrumental in me learning and understanding deployable structures. I met Ryan when he was a visiting researcher from JPL, and enjoyed thought provoking discussions started by him in our group meetings, and picking his brain for potential research projects earlier on in my PhD. Finally, while Angkur has been a more recent addition to our group meetings, I have enjoyed learning X-ray mechanics from his presentations, and am excited to have him on my committee.

I would also like to thank Guruswami Ravichandran, as he has been a big part of my experience at Caltech, starting from taking first year classes from him in COVID, to him proctoring my qualifying exams and chairing my candidacy committee, as well as his presence, discussions, and support in group meetings. I am sad that the timing of my defense did not work out in such a way for him to join my committee.

I am also grateful for the environment I was a part of, and the friends I made during my journey. My office was a fun environment to both goof around but also work in. In particular, I wanted to mention just a small, and definitely not complete, list of some of the people who have made this experience memorable: Shengduo Liu, Adeline Wihardja, Barry Lawlor, Vatsa Gandhi, Maximo Cravero Baraja, Carter Cocke, Mary Agajanian, and Eric Ocegueda. Additionally, there are a few people I have met outside my program that I wish to name: Gyllie, Kristin, and Emily. While not part of my academic environment, they have become great friends I met during my time here who have made it all the better.

There are a couple of former group members I wanted to thank in particular. First, Andrew Akerson has been one of the best research mentors I could have asked for, and helped me get started when I felt extremely in over my head at the beginning of my journey. Even after that, he has been an extremely supportive mentor, checking in on me often during his time in our group, but also after leaving as well. He also has been a good friend, and was one of the reasons I had so much fun working late in the office every night during the first few years of my PhD, and was an integral part of sillier adventures, like hoisting a couch up to our second floor balcony.

Another member of that particular escapade I wanted to thank is Aakila Rajan. Not just for his ability to lift a couch, but also for being an extremely close friend, research group member, and roommate, even if he did leave his coffee cups everywhere. My first experience with him was collaborating through discord on chemistry homework while he was stuck in India during Covid, and it quickly became a common occurrence when stuck on homework to be waiting for him to wake up so I could ask him for help. This proceeded well past first-year classes, especially when we became roommates, when I often walked into his room at 1am, asking him to be my sounding board when I was confused and needed help/a second opinion. Outside of just research, he is also one of my closest friends. As much as he helped me with research, he also has severely hindered my progress, as I spent far too long grabbing tacos, watching South Park, discussing world events, and preparing for competitive eating events with him.

I also want to thank my family for their impact on my life. My dad installed the ‘work hard, play hard’ mentality in me from such a young age. My brother Vinny was a constant in my life (the constant was usually an argument/fight which he most definitely started), and was someone I looked up to and still do, especially seeing his work ethic. My mom has been extremely supportive throughout my entire life, pushing me to do better and work harder, but also supporting me through the stressful times, and providing unwavering support and love.

Lastly, I want to thank my girlfriend Vivan. She has been my biggest cheerleader and who I share the great times with, and also my biggest supporter during the most

stressful times. From leaving supportive notes for me after especially tiring and stressful days, to coming to conferences with me to hear my talks, she puts so much time and effort into helping me be the best version of myself, and I don't know how I could have gotten through this journey without her. While everyone mentioned above (and even many not mentioned) have been part of making a home for me here, she has, by far, been the biggest part. Her family has also become like mine, and it's clear why she has been so kind and generous to me, because those values are reflected in them as well; her mom always prepares food for me when she knows I'm busy, and her dad dropped everything to help me out when our car broke down 400 miles away, driving there and back to tow us, and her sister Jess has become like the sister I never had and an exceptional source of gossip. There's infinitely more I can say, but I'll leave it with this: there is no one else besides Vivian that I would rather have by my side as I complete this endeavor.

And with that, let's talk about mechanics!

ABSTRACT

Shells - thin curved structures such as eggshells, insect wings, and pressure vessels - are ubiquitous in nature and engineering. They are slender yet structurally capable, supporting many times their own weight. They can also undergo dramatic geometric transitions, such as buckling, snap-through, and bistability. This combination of strength and geometric nonlinearity stems from the interplay between bending and stretching in thin geometries. As a result, simulating shells is numerically demanding. Finite-element methods are the standard tool, but thin shells require high order elements that adds substantial formulation and implementation complexity. An alternative approach to address some of these problems comes from the computer graphics community. Discrete differential geometry methods discretize the shell on a triangulated mesh using only nodal positions as degrees of freedom. This sidesteps the need for high order elements in finite element analysis. However, existing formulations are typically developed for visual realism rather than mechanical accuracy, and lack the physically meaningful energy formulations required for engineering design.

This thesis develops a discrete Kirchhoff-Love shell framework that combines a triangulated-mesh discretization with the mechanical rigor required for engineering design. The formulation employs a Koiter energy with standard engineering material constants, supports a spontaneous-curvature field for active materials, and provides analytic gradients and Hessians that enable Newton-Raphson equilibrium solving, adjoint sensitivity analysis, and energy-landscape path-finding. The framework is verified against four canonical shell benchmarks.

The framework is first applied to photoactive liquid crystal elastomer shells, governed by a spontaneous-curvature evolution law that couples illumination intensity and direction to surface geometry. Simulations capture a flat sheet that bifurcates to a cylindrical configuration under uniform illumination, resulting from the Gauss curvature coupling between bending and stretching. A second example shows a thin active sheet that reorients to track a moving light source, analogous to a sunflower.

Tape springs are thin curved strips used as deployable booms in spacecraft; they fold compactly via snap-through buckling and recover a stiff deployed state on release. The framework is then applied to simulate their forward bending response in opposite-sense and equal-sense loading modes. The opposite-sense results match

analytical predictions for the propagation moment and localized fold geometry.

Building on the tape spring analysis, a multi-equilibrium topology optimization method computes adjoint sensitivities through the deployed and folded states simultaneously. A parameter sweep over volume fraction, design region, and folded-state moment threshold reveals non-intuitive topologies, including hourglass designs that single-state optimizers cannot access.

Finally, the nudged elastic band method is applied within the discrete-shell framework to compute the minimum-energy path for the eversion of a bistable spherical cap. The path passes through a non-axisymmetric saddle, illustrating the energetic favorability of asymmetric eversion, which stems from the interplay between Gauss curvature and stretch.

Together, these applications establish the framework as a versatile, mechanically grounded platform for simulating the nonlinear mechanics of thin shells.

PUBLISHED CONTENT AND CONTRIBUTIONS

[1] Sathvik Sanagala and Kaushik Bhattacharya. "Artificial sunflower: Light-induced deformation of photoactive shells". In: *Extreme Mechanics Letters* 76 (2025), p. 102302. ISSN: 2352-4316. DOI: https://doi.org/10.1016/j.eml.2025.102302. URL: https://www.sciencedirect.com/science/article/pii/S2352431625000148.

Contributions: S.S. developed the computational code and performed the simulations. S.S. and K.B. wrote the manuscript.

TABLE OF CONTENTS

LIST OF ILLUSTRATIONS

LIST OF TABLES

Chapter 1

INTRODUCTION

1.1 Shells

Shells – thin curved structures – are ubiquitous in both nature and engineered applications. Natural examples include eggshells [1, 2], insect wings [3, 4], and cell membranes [5, 6], and engineered examples include pressure vessels [7, 8], contact lenses [9, 10], and soft robots [11]. What unites these examples is the relative ease of bending compared to stretching: bending a sheet of paper is trivial, while stretching it requires substantial force. This stems from shell thinness: stretching stiffness scales linearly with thickness while bending stiffness scales with the cube [12–14], so for sufficiently thin shells, bending becomes energetically favorable relative to stretching. Therefore, a shell prefers deformations that change curvature while preserving the in-plane metric. This preference is constrained by Gauss's remarkable theorem [15], which states that Gaussian curvature is an intrinsic surface property, meaning not every curvature change is achievable without stretching. Thus, the low-energy bending mode becomes coupled to the high-energy stretching mode, leading to localized buckling or snap-through transitions [16–20].

This interplay between stretching and bending means that thin shells display a rich range of mechanical behaviors. Take, for example, an empty soda can. It can withstand a very large purely axial load, but crumbles dramatically with even the slightest lateral load [21, 22]. This complexity is exploited in nature, for example the Venus flytrap [23] and the folding of pollen grains [24]. They are also exploited in engineering. Shells provide unexpected rigidity but can also fail dramatically (e.g., domed structures [18]). Deployable space structures fold by exploiting buckling and snap back into stiff equilibria on release [25–27].

This complexity also makes shells challenging to analyze with standard numerical methods. An alternative approach comes from the computer graphics community, where discrete shells were developed to render deformable surfaces [28, 29]. This thesis adapts the framework to incorporate the mechanics of shells, demonstrating its efficacy on a series of accepted benchmarks. The thesis then uses this framework to study three applications: (i) stimuli-responsive shells in which light reshapes the structure, (ii) the forward analysis and inverse design of multistable tape-spring structures, and (iii) the saddle configurations between stable states using the nudged elastic band method.

1.2 Modeling Challenges

Finite element analysis (FEA) is a widely used method for studying the mechanics of solids [30–32]. However, shells present a fundamental difficulty: bending energy involves second derivatives of the displacement field, leading to fourth-order nonlinear equations that require C^1 continuity of the shape functions across element boundaries [33, 34]. Standard C^0 elements interpolate displacements continuously but leave normal rotations discontinuous at interfaces. This produces an ill-defined curvature field and leads to locking, spurious stiffness, or incorrect bending behavior. The standard treatment is to use higher-order elements with C^1 continuity, but these require degrees of freedom for both displacements and their gradients at each node, substantially increasing the number of degrees of freedom. An alternative is to relax the strict C^1 requirement by introducing additional kinematic variables or weakly enforcing the Kirchhoff constraints [35–37]. For example, Discrete Kirchhoff Triangle (DKT) elements enforce the zero-transverse-shear condition only in a discrete sense [38], while Mixed Interpolation of Tensorial Components (MITC) elements, typically formulated in the Reissner–Mindlin setting, interpolate selected strain components to alleviate locking [39, 40]. These approaches have been successful in practice, but they come with added formulation and implementation complexity.

Reduced-order discrete formulations offer an alternative that sidesteps the C^1 requirement entirely. Discrete differential geometry (DDG) methods for thin shells, originating largely in the computer graphics community [29], discretize shell kinematics directly on triangulated meshes. By expressing stretching and bending energies in terms of edge lengths and dihedral angles, these methods achieve a coordinate-free formulation that naturally handles large rotations and only requires nodal positions as degrees of freedom: there is no need for tracking function gradients.

This combination of geometric flexibility, sparse linear algebra, and ease of implementation has made DDG shells the standard tool for physically-based animation, powering cloth simulation, character deformation, and morphing surfaces in computer graphics and film. Their adoption in engineering mechanics has been more limited: most DDG formulations were designed for visual realism rather than physical accuracy, approximating bending through geometric hinge-angle proxies rather than the physical Koiter energy, and lack the mechanically grounded material models and analytic derivative structure that engineering design requires. Recent efforts have begun to push DDG shells toward more mechanically rigorous formulations [41]; for a broader survey of DDG methods for flexible systems, see [42]. However, no single framework yet brings together the capabilities engineering design demands.

To our knowledge, no existing DDG shell framework combines all of the following: a Kirchhoff-Love energy on arbitrary unstructured meshes with physically meaningful elastic constants, support for active materials through a spontaneous curvature field, and explicitly derived analytic derivatives of the discrete energy. Chapter 2 presents a framework that closes these gaps; its specific contributions are enumerated in Section 1.4.

1.3 Applications

While external mechanical loads drive shape change in many shells, stimuli-responsive materials offer a complementary mechanism: the shell itself deforms in response to environmental fields. These materials have received increased attention due to their ability to convert external fields into mechanical work, offering promising applications including artificial muscles [43], soft robotics [11], and actuators [44]. Within this class, photomechanically active materials are particularly attractive because they deform when exposed to light, allowing for remote, tether-free actuation [45]. An important class of photomechanically active materials is liquid crystal elastomers, which are embedded with photoactive molecules such as azobenzene [46, 47]. Most prior modeling of photomechanical materials has focused on 1D strips and beams. Chapter 3 develops a 2D model for photoactive LCE shells, where light-induced spontaneous curvature couples with the stretching-bending interplay introduced in Section 1.1 to produce rich shape change.

Tape springs are thin cylindrical shells with an open cross-section, widely used as deployable booms in space structures owing to their high stiffness-to-weight ratio. Under opposite-sense bending, a localized fold forms via snap-through buckling, enabling reversible switching between a compact folded configuration and a stiff deployed state [25, 26]. This multistability, driven by geometric nonlinearity and a rich energy landscape, makes tape springs a natural test case for multi-equilibrium design: performance requirements span two geometrically distinct configurations, and the transition between them involves a snap-through event inaccessible to linear or single-equilibrium methods. Stiffness in the deployed state and low resistance to folding are competing requirements, since denser cross-sections improve deployed stiffness but also store more bending energy in the fold. Chapter 4 applies the discrete shell model to the tape spring forward problem, and Chapter 5 formulates a multi-equilibrium topology optimization that designs across both equilibria, balancing deployed-state stiffness against folded-state moment.

The stable states of a multistable shell are only part of the picture. The paths between them, and the barriers that separate them, govern actuation force, deployment dynamics, and failure modes. A canonical example is the bistable spherical cap, which inverts via snap-through, similar to a popper toy. Predicting the inversion path, including the intermediate shapes the structure passes through and the magnitude of the energy barrier separating the stable states, is a numerical problem distinct from locating equilibria. The nudged elastic band method computes minimum-energy paths between such stable states [48, 49], but existing applications have been largely confined to continuum FEM [50] and origami [51] settings, leaving shell-specific transitions largely unexplored. Chapter 6 brings the nudged elastic band method to the discrete shell framework, computing the inversion path of a bistable spherical cap.

1.4 Contributions

Chapter 2 develops the discrete-shell framework that underpins this thesis. The framework discretizes a Koiter shell energy on a triangulated mesh, incorporates a spontaneous curvature field for active materials, and provides analytic gradients and Hessians for equilibrium solving and adjoint sensitivity analysis needed for topology optimization. The framework is validated against canonical shell benchmarks: a patch test, a cantilever with tip force, a pinched cylinder, and a clamped circular plate.

Chapter 3 applies the framework to photoactive liquid crystal elastomer shells, using a spontaneous-curvature evolution law that couples illumination intensity and direction to surface geometry. Simulations included involve a flat sheet that bifurcates to a cylindrical configuration under uniform illumination and a thin active sheet that reorients to track the source of light, similar to an artificial sunflower.

Chapter 4 applies the discrete shell framework to simulate the forward bending response of a tape spring in both opposite-sense and equal-sense loading modes. The opposite-sense results match published finite-element and analytical references for the peak and propagation moments and the localized fold geometry, and the equal-sense bifurcation is captured directly by Newton Raphson, without the imperfection seeding or arc-length continuation that prior treatments have required.

Chapter 5 develops a multi-equilibrium topology optimization method for thin shells, computing adjoint sensitivities through two distinct equilibrium states simultaneously. A parameter sweep over volume fraction, design region, and moment threshold reveals non-intuitive topologies, including hourglass designs that single-state optimizers cannot access. A first-principles analysis interprets these designs via classical beam mechanics.

Chapter 6 applies the nudged elastic band method to compute the minimum-energy path for the eversion of a bistable spherical cap, identifying the unforced energy barrier between its two stable configurations. The path passes through a non-axisymmetric saddle, a localized fold. The barrier increases monotonically with shell thickness and cap depth. The thickness scaling sits between the bending and membrane limits, reflecting the saddle's coupled bending-membrane deformation, while the cap-depth dependence tracks the strength of bistability.

1.5 Outline

The remainder of the thesis is organized as follows. Chapter 2 develops the discrete-shell framework and its validation. Chapter 3 applies the framework to photoactive liquid crystal elastomer shells. Chapter 4 treats the tape-spring forward problem in opposite-sense and equal-sense bending. Chapter 5 develops multi-equilibrium topology optimization for tape-spring design. Chapter 6 applies the nudged elastic band method to cap inversion. Chapter 7 synthesizes the contributions and discusses future directions.

References

[1] David Taylor et al. "The fracture toughness of eggshell". In: *Acta biomaterialia* 37 (2016), pp. 21–27.

[2] Eric N. Hahn et al. "Nature's technical ceramic: the avian eggshell". In: *Journal of The Royal Society Interface* 14.126 (Jan. 2017), p. 20160804. ISSN: 1742-5689. DOI: 10.1098/rsif.2016.0804. eprint: https://royalsocietypublishing.org/rsif/article-pdf/doi/10.1098/rsif.2016.0804/468443/rsif.2016.0804.pdf. URL: https://doi.org/10.1098/rsif.2016.0804.

[3] Antonia B Kesel, Ute Philippi, and Werner Nachtigall. "Biomechanical aspects of the insect wing: an analysis using the finite element method". In: *Computers in Biology and Medicine* 28.4 (1998), pp. 423–437. ISSN: 0010-4825. DOI: https://doi.org/10.1016/S0010-4825(98)00018-3. URL: https://www.sciencedirect.com/science/article/pii/S0010482598000183.

[4] SR Jongerius and DJEM Lentink. "Structural analysis of a dragonfly wing". In: *Experimental Mechanics* 50.9 (2010), pp. 1323–1334.

[5] Wolfgang Helfrich. "Elastic properties of lipid bilayers: theory and possible experiments". In: *Zeitschrift für Naturforschung c* 28.11-12 (1973), pp. 693–703.

[6] Mingyang Hu, John J Briguglio, and Markus Deserno. "Determining the Gaussian curvature modulus of lipid membranes in simulations". In: *Biophysical journal* 102.6 (2012), pp. 1403–1410.

[7] Dennis R Moss. *Pressure vessel design manual*. Elsevier, 2004.

[8] Hassan Mohamed Abdelalim Abdalla, D Casagrande, and F De Bona. "Thin-walled pressure vessels of minimum mass or maximum volume". In: *Structural and Multidisciplinary Optimization* 61.1 (2020), pp. 111–121.

[9] Tarnveer Singh Bhamra and Brian J Tighe. "Mechanical properties of contact lenses: The contribution of measurement techniques and clinical feedback to 50 years of materials development". In: *Contact Lens and Anterior Eye* 40.2 (2017), pp. 70–81.

[10] W Wang et al. "Mechanical characterization of a convex shell (contact lens) with meridional thickness variation". In: *Experimental Mechanics* 58.6 (2018), pp. 997–1002.

[11] Cecilia Laschi, Barbara Mazzolai, and Matteo Cianchetti. "Soft robotics: Technologies and systems pushing the boundaries of robot abilities". In: *Science Robotics* 1.1 (2016), eaah3690. DOI: 10.1126/scirobotics.aah3690. URL: https://www.science.org/doi/abs/10.1126/scirobotics.aah3690.

[12] Warner Tjardus Koiter. "On the nonlinear theory of thin elastic shells". In: *Proc. Koninkl. Ned. Akad. van Wetenschappen, Series B* 69 (1966), pp. 1–54.

[13] C. R. Calladine. *Theory of Shell Structures*. Cambridge University Press, 1983.

[14] Basile Audoly and Yves Pomeau. "Elasticity and geometry". In: *Peyresq Lectures on Nonlinear Phenomena*. World Scientific, 2000, pp. 1–35.

[15] Carl Friedrich Gauss. *Disquisitiones generales circa superficies curvas*. Dieterich, 1827.

[16] L. Pauchard and S. Rica. "Contact and compression of elastic spherical shells: the physics of a 'ping-pong' ball". In: *Philosophical Magazine B* 78.2 (1998), pp. 225–233.

[17] Alice Nasto and Pedro M. Reis. "Localized Structures in Indented Shells: A Numerical Investigation". In: *Journal of Applied Mechanics* 81.12 (Oct. 2014), p. 121008. ISSN: 0021-8936. DOI: 10.1115/1.4028804. eprint: https://asmedigitalcollection.asme.org/appliedmechanics/article-pdf/81/12/121008/6080452/jam_081_12_121008.pdf. URL: https://doi.org/10.1115/1.4028804.

[18] Michael Gomez, Derek E Moulton, and Dominic Vella. "The shallow shell approach to Pogorelov's problem and the breakdown of 'mirror buckling'". In: *Proceedings of the Royal Society A: Mathematical, Physical and Engineering Sciences* 472.2187 (2016).

[19] Matteo Taffetani et al. "Static bistability of spherical caps". In: *Proceedings of the Royal Society A: Mathematical, Physical and Engineering Sciences* 474.2213 (2018).

[20] Lucia Stein-Montalvo et al. "Efficient snap-through of spherical caps by applying a localized curvature stimulus". In: *The European Physical Journal E* 45.1 (2022), p. 3.

[21] Theodore Von Kármán and Hsue-Shen Tsien. "The buckling of thin cylindrical shells under axial compression". In: *Journal of the Aeronautical Sciences* 8.8 (1941), pp. 303–312.

[22] John D Reid, Robert W Bielenberg, and Brian A Coon. "Indenting, buckling and piercing of aluminum beverage cans". In: *Finite elements in analysis and design* 37.2 (2001), pp. 131–144.

[23] Yoël Forterre et al. "How the Venus flytrap snaps". In: *Nature* 433.7024 (2005), pp. 421–425.

[24] Eleni Katifori et al. "Foldable structures and the natural design of pollen grains". In: *Proceedings of the National Academy of Sciences* 107.17 (2010), pp. 7635–7639.

[25] K. A. Seffen and S. Pellegrino. "Deployment dynamics of tape springs". In: *Proceedings of the Royal Society of London. Series A: Mathematical, Physical and Engineering Sciences* 455.1983 (1999), pp. 1003–1048. DOI: 10.1098/rspa.1999.0347. URL: https://royalsocietypublishing.org/doi/10.1098/rspa.1999.0347.

[26] K. A. Seffen. "On the behavior of folded tape-springs". In: *Journal of Applied Mechanics* 68.3 (2001), pp. 369–375. DOI: 10.1115/1.1365153. URL: https://asmedigitalcollection.asme.org/appliedmechanics/article-abstract/68/3/369/462849.

[27] Chinthaka Mallikarachchi and Sergio Pellegrino. “Quasi-Static Folding and Deployment of Ultrathin Composite Tape-Spring Hinges”. In: *Journal of Spacecraft and Rockets* 48 (Jan. 2011). DOI: 10.2514/1.47321.

[28] David Baraff and Andrew Witkin. “Large steps in cloth simulation”. In: *Proceedings of the 25th Annual Conference on Computer Graphics and Interactive Techniques*. SIGGRAPH ’98. New York, NY, USA: Association for Computing Machinery, 1998, pp. 43–54. ISBN: 0897919998. DOI: 10.1145/280814.280821. URL: https://doi.org/10.1145/280814.280821.

[29] Eitan Grinspun et al. “Discrete Shells”. In: *Proceedings of the 2003 ACM SIGGRAPH/Eurographics Symposium on Computer Animation*. SCA ’03. San Diego, California: Eurographics Association, 2003, pp. 62–67. ISBN: 1581136595.

[30] Thomas JR Hughes. *The finite element method: linear static and dynamic finite element analysis*. Courier Corporation, 2003.

[31] Olgierd C Zienkiewicz and Robert Leroy Taylor. *The finite element method set*. Elsevier, 2005.

[32] Klaus-Jürgen Bathe. *Finite element procedures*. Klaus-Jurgen Bathe, 2006.

[33] Fehmi Cirak, Michael Ortiz, and Peter Schröder. “Subdivision surfaces: a new paradigm for thin-shell finite-element analysis”. In: *International Journal for Numerical Methods in Engineering* 47 (2000). DOI: 10.1002/(SICI)1097-0207(20000430)47:123.0.CO;2-1. URL: http://www.multires.caltech.edu/pubs/thinshell.pdf.

[34] J. Kiendl et al. “Isogeometric shell analysis with Kirchhoff–Love elements”. In: *Computer Methods in Applied Mechanics and Engineering* 198.49–52 (2009), pp. 3902–3914. DOI: 10.1016/j.cma.2009.08.013. URL: https://www.sciencedirect.com/science/article/abs/pii/S0045782509002680.

[35] Eric Reissner. “The effect of transverse shear deformation on the bending of elastic plates”. In: (1945).

[36] R. D. Mindlin. “Influence of rotatory inertia and shear on flexural motions of isotropic, elastic plates”. In: (1951).

[37] Sohrabuddin Ahmad, Bruce M Irons, and OC Zienkiewicz. “Analysis of thick and thin shell structures by curved finite elements”. In: *International journal for numerical methods in engineering* 2.3 (1970), pp. 419–451.

[38] Jean-Louis Batoz, Klaus-JÜRgen Bathe, and Lee-Wing Ho. “A study of three-node triangular plate bending elements”. In: *International journal for numerical methods in engineering* 15.12 (1980), pp. 1771–1812.

[39] Klaus-Jürgen Bathe and Eduardo N Dvorkin. "A four-node plate bending element based on Mindlin/Reissner plate theory and a mixed interpolation". In: *International Journal for Numerical Methods in Engineering* 21.2 (1985), pp. 367–383.

[40] Klaus-Jürgen Bathe and Eduardo N Dvorkin. "A formulation of general shell elements—the use of mixed interpolation of tensorial components". In: *International journal for numerical methods in engineering* 22.3 (1986), pp. 697–722.

[41] Weicheng Huang et al. "Discrete differential geometry-based model for nonlinear analysis of axisymmetric shells". In: *International Journal of Mechanical Sciences* 283 (2024), p. 109742. DOI: 10.1016/j.ijmecsci.2024.109742. URL: https://www.sciencedirect.com/science/article/pii/S0020740324007835.

[42] Dezhong Tong et al. *Discrete Differential Geometry for Simulating Nonlinear Behaviors of Flexible Systems: A Survey*. 2025. eprint: arXiv:2510.17546. URL: https://arxiv.org/abs/2510.17546.

[43] Seyed M. Mirvakili and Ian W. Hunter. "Artificial Muscles: Mechanisms, Applications, and Challenges". In: *Advanced Materials* 30.6 (2018), p. 1704407. DOI: 10.1002/adma.201704407. URL: https://onlinelibrary.wiley.com/doi/abs/10.1002/adma.201704407.

[44] Liang Hu et al. "Stimuli-responsive polymers for sensing and actuation". In: *Materials Horizons* 6 (9 2019), pp. 1774–1793. DOI: 10.1039/C9MH00490D. URL: http://dx.doi.org/10.1039/C9MH00490D.

[45] Timothy J White. *Photomechanical Materials, Composites, and Systems*. Wireless Transduction of Light into Work. John Wiley & Sons, 2017.

[46] Yanlei Yu, Makoto Nakano, and Tomiki Ikeda. "Directed bending of a polymer film by light". In: *Nature* 425.145 (2003). DOI: 10.1038/425145a. URL: https://www.nature.com/articles/425145a.

[47] Anne Helene Gelebart et al. "Making waves in a photoactive polymer film". In: *Nature* 546 (2017). DOI: 10.1038/nature22987. URL: https://www.nature.com/articles/nature22987.

[48] Hannes Jónsson, Greg Mills, and Karsten W. Jacobsen. "Nudged elastic band method for finding minimum energy paths of transitions". In: *Classical and Quantum Dynamics in Condensed Phase Simulations*. Ed. by B. J. Berne, G. Ciccotti, and D. F. Coker. Singapore: World Scientific, 1998, pp. 385–404. DOI: 10.1142/9789812839664_0016.

[49] Graeme Henkelman, Blas P. Uberuaga, and Hannes Jónsson. "A climbing image nudged elastic band method for finding saddle points and minimum energy paths". In: *The Journal of Chemical Physics* 113.22 (2000), pp. 9901–9904. DOI: 10.1063/1.1329672. URL: https://pubs.aip.org/aip/jcp/article/113/22/9901/185050.

[50] Guangchao Wan et al. “Finding transition state and minimum energy path of bistable elastic continua through energy landscape explorations”. In: *Journal of the Mechanics and Physics of Solids* 183 (2024), p. 105503. DOI: 10.1016/j.jmps.2023.105503. URL: https://www.sciencedirect.com/science/article/abs/pii/S0022509623003071.

[51] Hao Zhou et al. “Low energy fold paths in multistable origami structures”. In: *International Journal of Solids and Structures* 265–266 (2023), p. 112125. DOI: 10.1016/j.ijsolstr.2023.112125. URL: https://www.sciencedirect.com/science/article/pii/S0020768323000239.

Chapter 2

DISCRETE SHELL FORMULATION AND NUMERICAL METHODS

2.1 Introduction

There are numerous approaches for studying the mechanics of plates and shells [1–5]. The Föppl-von Kármán equations [6, 7] are commonly used for small deformations and shallow shells, but the study of large deformation requires higher-order nonlinear differential equations. This in turn requires higher-order discretization, resulting in more challenging numerical problems. An alternate approach with origins in computer graphics [8, 9] begins in the discretized setting and yields a lower-order model. In recent years, a strong connection to differential geometry has risen, enabling the development of discrete models for shells [10–12]. We integrate this approach with the energetics of shells to develop an efficient yet physically meaningful computational method for thin-shell mechanics.

Existing mechanically-oriented DDG formulations each address parts of what engineering design requires, but none achieves the full combination. Many DDG bending models, including the foundational formulation of Grinspun et al. [9], approximate curvature through dihedral angles between adjacent faces rather than constructing the second fundamental form $b_{\alpha\beta}$ explicitly; such hinge-based models treat bending energy as a geometric proxy, a function of face-normal angles rather than an expression tied to E, ν, and thickness through the Koiter formula, and while they support equilibrium solving and can be differentiated, the resulting sensitivities do not correspond to physical material response and are therefore unsuitable for quantitative engineering design. Huang et al. [13] formulate a DDG shell with explicit Koiter stiffness tensors depending on E, ν, and thickness, but restrict to axisymmetric geometries via a one-dimensional meridional discretization; Weischedel [12] derives a mechanically grounded discrete shell energy but within a Cosserat framework, reintroducing rotational degrees of freedom that DDG was designed to bypass. Mechanically rigorous Kirchhoff-Love formulations exist in the isogeometric analysis (IGA) literature [14], which builds on Non-Uniform Rational B-Splines (NURBS) to achieve C^1 continuity on CAD-compatible structured patch geometries. The structured patch requirement, however, limits topological flexibility and is ill-suited to the large-deformation, unstructured-mesh setting that DDG targets.

We present such a framework, a discrete formulation that serves as a standalone, general-purpose computational tool. The framework discretizes the Koiter shell energy on an unstructured triangulated mesh, computing stretching and bending contributions element-wise from discrete covariant bases and mid-edge normals. It incorporates a spontaneous curvature field h^*: setting $h^* = 0$ recovers the passive elastic shell, while prescribing h^* models active materials such as liquid crystal elastomers. Analytic derivatives of the discrete energy with respect to nodal positions are derived explicitly, yielding Newton-Raphson solving capabilities, consistent tangent stiffness matrices, and adjoint sensitivities suitable for large-scale design optimization. The result is a framework suited for both forward simulation and gradient-based inverse design for robust topology optimization.

2.2 Continuum formulation

We present the discrete Kirchhoff-Love shell framework that forms the computational foundation of this thesis. We focus here on the framework in its general form, emphasizing the structure of the discrete energy and its derivatives that enable equilibrium solving, adjoint sensitivity analysis, and energy-landscape path-finding.

We adopt the Kirchhoff-Love assumption [2], so the deformation is fully described by the shell midsurface and its associated unit normal. Let $\eta = (\eta^1, \eta^2)$ be a local parameterization of the midsurface, with $S_0 \subset \mathbb{R}^3$ and $S \subset \mathbb{R}^3$ the reference and current domains, respectively. Material particles $R \in S_0$ map to $r \in S$ via the deformation $r = \Phi(R)$.

From these embeddings, we can define covariant bases $\{E_\alpha\}_{\alpha=1}^2$ and $\{e_\alpha\}_{\alpha=1}^2$ for the tangent spaces of the reference and current configurations respectively, as

$$E_\alpha = \frac{\partial R}{\partial \eta^\alpha}, \quad e_\alpha = \frac{\partial r}{\partial \eta^\alpha}, \quad \alpha = 1, 2. \tag{2.1}$$

We denote the corresponding contravariant bases as $\{E^\alpha\}_{\alpha=1}^2$ and $\{e^\alpha\}_{\alpha=1}^2$ respectively ($E_\alpha \cdot E^\beta = e_\alpha \cdot e^\beta = \delta_\alpha^\beta$).

The elastic state of the shell is characterized by the stretch g and material curvature h,

$$g = (\nabla_R r)^T (\nabla_R r), \quad h = -(\nabla_R r)^T (\nabla_R n), \tag{2.2}$$

where $n = (e_1 \times e_2)/|e_1 \times e_2|$ is the unit normal in the current configuration. Differentiating with respect to η^α, g and h take component form through standard differential geometric operators: the first and second fundamental forms $a_{\alpha\beta}$ and $b_{\alpha\beta}$,

$$g = \sum_{\alpha,\beta} a_{\alpha\beta}(E^\alpha \otimes E^\beta), \quad h = \sum_{\alpha,\beta} b_{\alpha\beta}(E^\alpha \otimes E^\beta), \tag{2.3}$$

where $a_{\alpha\beta} = e_\alpha \cdot e_\beta$ and $b_{\alpha\beta} = -e_\alpha \cdot (\partial n/\partial \eta^\beta)$. In the undeformed configuration ($r = R$), g reduces to the identity and h to the reference curvature.

Following Koiter [15], the total elastic energy decomposes into stretching and bending contributions:

$$\mathcal{E} = \int_{S_0} \left(t\, W_s + \frac{t^3}{12} W_b \right) dA, \tag{2.4}$$

where t denotes the shell thickness. The stretching and bending energy densities W_s and W_b can in principle be chosen independently; here we adopt a Neo-Hookean model for stretching to accommodate large deformations [16]:

$$W_s = \frac{E}{4(1+\nu)} \Big(\mathrm{tr}(g) - 2 - \ln(\det(g)) \Big) + \frac{E\nu}{2(1-\nu^2)} \Big(\det(g)^{\frac{1}{2}} - 1 \Big)^2. \tag{2.5}$$

For bending, we adopt an energy quadratic in the relative curvature:

$$W_b = \frac{E\nu}{2(1-\nu^2)} tr(\tilde{h})^2 + \frac{E}{2(1+\nu)}\, tr(\tilde{h}^2), \tag{2.6}$$

where the relative curvature is

$$\tilde{h} = h - h^*, \tag{2.7}$$

where h^* is the spontaneous curvature, encoding the shell's preferred intrinsic geometry. Setting $h^* = 0$ recovers the passive elastic shell; prescribing a spatially varying h^* models active materials such as liquid crystal elastomers (Chapter 3).

2.3 Discretization

Triangulated midsurface and discrete bases

We represent the shell midsurface as a triangulated mesh, with nodes $\{R^a\}$ in the reference domain and corresponding nodes $\{r^a\}$ in the current configuration [9, 10], as illustrated in Figure 2.1.

Now consider an individual element, defined by the three nodes $\{R^a, R^b, R^c\}$ and $\{r^a, r^b, r^c\}$ in the reference and deformed configurations respectively. To obtain a discrete covariant basis, we choose a local parameterization $\{\xi^1, \xi^2\}$, going from node a to node b, and node a to node c respectively. This yields local discrete covariant bases in the reference and current configurations as

$$E_1 = R^b - R^a, \quad E_2 = R^c - R^a, \quad e_1 = r^b - r^a, \quad e_2 = r^c - r^a, \tag{2.8}$$

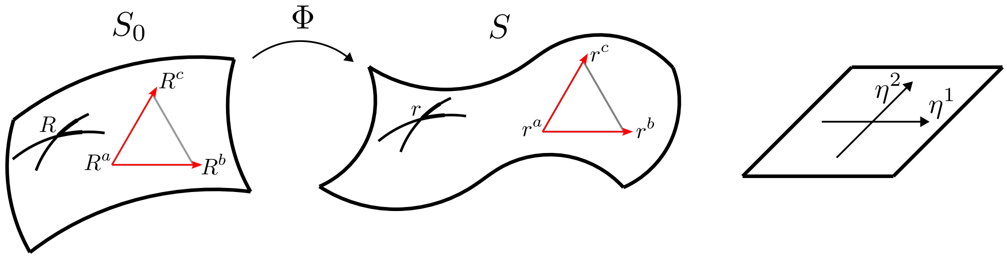

Figure 2.1: Kinematics. The reference shell is represented through its midsurface S_0 where the position of a particle R is parameterized by parameters $\{\eta^1, \eta^2\}$. The deformation Φ maps R on S_0 to the deformed position r on the midsurface of the deformed shell S. The reference and current images of a discrete element are also shown with nodes $\{R^a, R^b, R^c\}$ and $\{r^a, r^b, r^c\}$ respectively.

and the corresponding discrete contravariant bases follow from this result. This is sufficient for computing the element-wise discrete stretch g via (2.3).

For the material curvature h, we must define a curvature approximation [11, 12]. For an individual element, we enumerate the edges by the vertex opposite the edge. We define the mid-edge normal as the unit bisector of the normal vectors of the elements adjacent to the edge. The triangle constructed from the edge mid-points is congruent with the element at half size, yielding the approximation:

$$\frac{\partial n}{\partial \xi^1} = -2(n^b - n^a), \quad \frac{\partial n}{\partial \xi^2} = -2(n^c - n^a), \tag{2.9}$$

allowing computation of the material curvature h using (2.3). Explicit representations are given in the appendix.

The element-wise reference area can be computed as

$$A = \frac{1}{2}|E_1 \times E_2| = \frac{1}{2}(\det(E_\alpha \cdot E_\beta))^{1/2}. \tag{2.10}$$

The edge vectors $E_1 = R^b - R^a$, $E_2 = R^c - R^a$ serve directly as the discrete covariant basis, implicitly defining a local parameterization for each element, one that varies element-by-element and is never explicitly computed. No global parameterization is needed; constructing one would in fact complicate implementation. Only nodal positions are required.

Energy and equilibrium

The total discrete energy is

$$\mathcal{E} = \sum_e A_e \left(t\, W_s(g_e) + \frac{t^3}{12} W_b(\tilde{h}_e) \right), \tag{2.11}$$

where e indexes the elements, A_e, g_e, and $\tilde{h}_e$ are the area, stretch, and relative curvature of element e, respectively.

Equilibrium is found by minimizing (2.11) over the nodal positions $\{r^a\}$ via Newton-Raphson iteration.

Derivatives

Newton-Raphson iteration requires the gradient $\partial\mathcal{E}/\partial r^a$ (internal force vector) and the Hessian $\partial^2\mathcal{E}/\partial r^a \partial r^b$ (tangent stiffness matrix) with respect to nodal positions. Both are derived analytically, yielding exact, efficient expressions. These same derivatives underlie the adjoint sensitivity maps used in topology optimization and the force evaluations in the nudged elastic band method. Full expressions are given in the Appendix.

Loading and boundary-condition conventions

The discrete formulation carries only nodal positions as degrees of freedom (no independent function gradients). Therefore, external forces are applied as nodal force vectors. Specifically, they are applied as pointwise loads concentrated on individual nodes, or an area-weighted distribution for distributed loads and body forces. External moments are realized as force couples on two opposing rows of boundary nodes. A couple delivers the desired resultant moment while contributing zero net force.

Fully fixed/clamped displacement boundary conditions require a similar two-row treatment, for a related reason. The bending energy at each triangle is computed from the differences between that triangle's surface normal and the normals of its three neighbor triangles across its three edges (the midedge-average formulation; see Appendix A). When a triangle has an edge on the mesh boundary, it has no neighbor across that edge and the corresponding contribution drops to zero, removing the bending stiffness associated with rotation about that edge. Clamping only a single line of nodes at the boundary therefore leaves the first row of triangles free to hinge, and the structure cannot support a transverse load. The remedy, used uniformly across all benchmarks below, is to clamp a band of nodes spanning at least two triangle rows (width $w_{\text{band}} \gtrsim 2\bar{h}_{\text{edge}}$). This allows rotations to be fixed for the boundary triangles, therefore adding full bending stiffness. The cost is a small $O(h)$ reduction of the structurally active domain (denoted L_{eff} or R_{eff} within this section).

2.4 Verification

We verify the discrete shell framework on four classical benchmarks spanning the regimes of interest: (i) a patch test on a cantilever, which isolates the discrete energy's consistency with the continuum model from any effects of the solver or boundary-condition; (ii) a cantilever under end load, which tests the Newton solver in one-dimensional bending-dominated regime; (iii) the pinched cylinder, a standard shell benchmark that exercises bending-dominated response on a closed curved surface under radial point loads; and (iv) a clamped circular plate under center point load, testing two-dimensional bending. Each benchmark is run on a sequence of uniformly refined meshes, with edge length successively refined by half, to investigate convergence behavior.

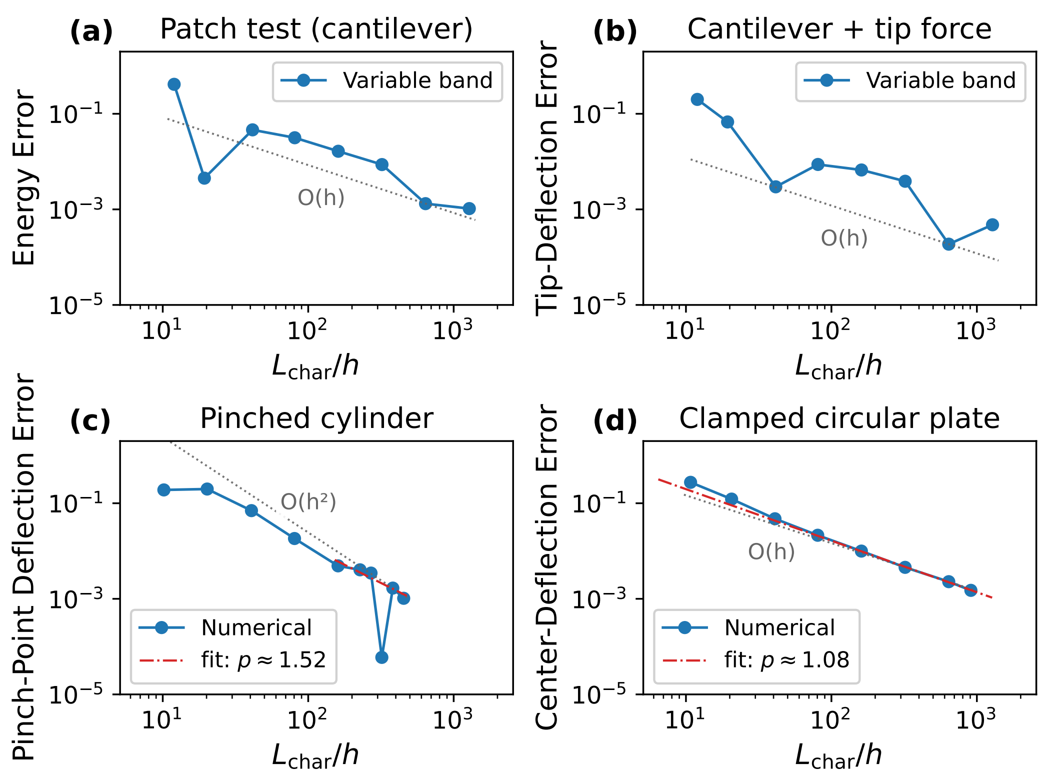

Figure 2.2: Convergence of relative error against mesh refinement for the four verification benchmarks. The abscissa is L_{char}/h (elements per characteristic length: L for the patch test and cantilever strip, L for the pinched cylinder, $2R$ for the circular plate). Variable (mesh-scaled) and fixed (constant-width) band-clamp variants are overlaid where both are available. O(h) reference slope is drawn through the asymptotic tail. For the circular plate a least-squares fit to the last four meshes is also shown (observed order p). For the pinched cylinder, a least-squares fit is shown for the last 5 meshes barring the outlier, explained more in the discussion.

n_{verts}	h	W_{num}	W_{ana}	$W_{\text{num}}/W_{\text{ana}}$	rel. err.
32	0.835	1.362×10^{-2}	9.634×10^{-3}	1.414	41.4 %
66	0.517	1.196×10^{-2}	1.201×10^{-2}	0.996	0.4 %
248	0.241	1.503×10^{-2}	1.437×10^{-2}	1.046	4.6 %
849	0.124	1.595×10^{-2}	1.546×10^{-2}	1.032	3.2 %
3 179	0.0621	1.632×10^{-2}	1.605×10^{-2}	1.016	1.6 %
12 302	0.0311	1.650×10^{-2}	1.636×10^{-2}	1.009	0.9 %
48 083	0.0156	1.653×10^{-2}	1.651×10^{-2}	1.001	0.1 %
190 889	0.00781	1.661×10^{-2}	1.659×10^{-2}	1.001	0.1 %
760 653	0.00390	1.664×10^{-2}	1.663×10^{-2}	1.001	0.1 %

Table 2.1: Patch test: discrete vs. analytical strain energy on the cantilever strip with variable band clamp $w_{\text{band}} = 2\bar{h}_{\text{edge}}$. Rows are ordered from coarsest to finest; vertex count identifies each mesh.

Patch test on a cantilever strip

The patch test, introduced by Irons & Razzaque [17], asks whether the discrete energy reproduces the energy of an analytically prescribed displacement field, isolating the consistency of the discrete formulation from the solver and boundary conditions. We place the nodes of a rectangular cantilever strip at the analytical small-deflection tip-loaded beam displacement,

$$w(x) = -\frac{P\,x_{\text{rel}}^2\,(3L_{\text{eff}} - x_{\text{rel}})}{6EI}, \qquad u(x) = -\frac{1}{2}\int_0^{x_{\text{rel}}} \left(\frac{dw}{dx'}\right)^2 dx', \tag{2.12}$$

where $x_{\text{rel}} = x - w_{\text{band}}$ and u is the von Kármán axial-shortening correction [7], ensuring zero in-plane stretch in the linearized theory. The discrete stretching, bending, and residual energies are evaluated for these imposed positions. Two convergence criteria establish consistency: (i) $W_{\text{num}}/W_{\text{ana}} \to 1$ as $h \to 0$, where $W_{\text{ana}} = P^2 L_{\text{eff}}^3/(6EI)$ and W_{num} is the evaluated energy, and (ii) the stretching contribution W_{stretch} remains negligible.

Table 2.1 shows the results for $L = 10$, width $b = 1$, thickness $t = 0.1$, $E = 1.2 \times 10^6$, $\nu = 0$, and tip load $P = 0.1$, and confirms both criteria. The ratio $W_{\text{num}}/W_{\text{ana}}$ converges monotonically to unity at the observed $O(h)$ rate from the 248-vertex mesh onward, as shown in Figure 2.2a. The two coarsest meshes (32 and 66 vertices) lie below the resolution at which $O(h)$ convergence sets in. W_{stretch} stays of order 10^{-8}, approximately six orders of magnitude below the bending energy $W_{\text{bend}} \sim 10^{-2}$.

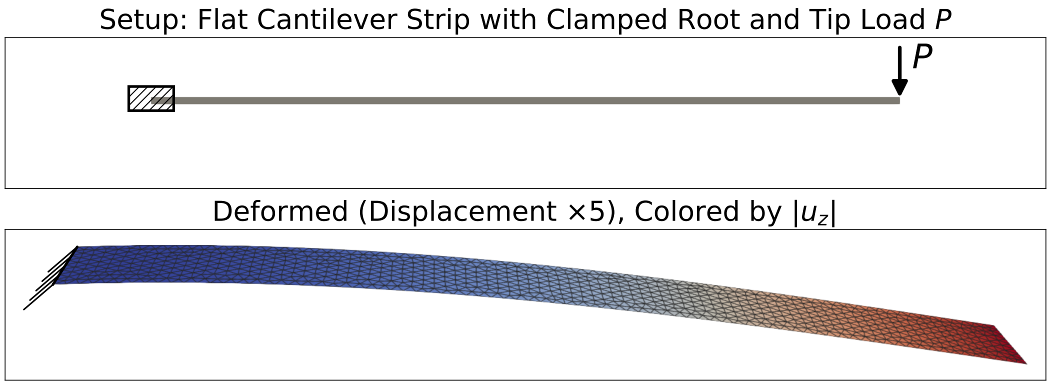

Figure 2.3: Cantilever under tip load. Top: flat strip with clamped root band (hatched) and tip line-load P. Bottom: deformed configuration (displacement magnified $\times 5$), colored by transverse displacement magnitude $|u_z|$. The band clamp spans two triangle rows.

Cantilever under tip force

Using the same strip geometry and material, we now apply the tip force as a distributed Neumann boundary condition and solve for the configuration via Newton-Raphson iteration (setup and deformed state shown in Figure 2.3). This is compared to the analytical small-deflection tip deflection: $w_{\text{tip}} = -PL_{\text{eff}}^3/(3EI)$. Table 2.2 reports the numerical tip deflection, analytical reference corrected for the $O(h)$ effective-length reduction $L_{\text{eff}} = L - w_{\text{band}}$, and their ratio, as a function of mesh refinement. The ratio converges monotonically to unity: the relative error drops below 1% at 248 vertices and below 0.1% at 48k vertices, as shown in Figure 2.2b. This benchmark exercises the complete nonlinear solver: Hessian assembly, sparse linear solve, Newton iteration with line-search globalization, and band-clamp boundary conditions.

Pinched Cylinder

The pinched cylinder is a standard shell-FEM verification problem that tests a method's ability to deal with inextensional bending modes and complex membrane states [18]. We use the parameters reported by Cirak et al.: a closed cylindrical shell with radius $R = 300$, length $L = 600$, and thickness $t = 3$, material properties $E = 3 \times 10^6$, $\nu = 0.3$. The cylinder is oriented along the y-axis, so that the circular cross-section lies in the xz-plane and the radius R is the in-plane distance from the central axis, as shown in Figure 2.4. Two equal and opposite radial point loads of magnitude $P = 1$ are applied at the midspan, one at $(0, L/2, +R)$ and one at $(0, L/2, -R)$, pinching the shell along the diameter. End-diaphragms at $y = 0$

n_{verts}	w_{band}	L_{eff}	$w_{\text{num}}/w_{\text{ana}}$	rel. err.
32	1.67	8.33	0.800	20.0 %
66	1.03	8.97	1.067	6.7 %
248	0.483	9.52	1.003	0.30 %
849	0.248	9.75	0.991	0.87 %
3 179	0.124	9.88	0.993	0.67 %
12 302	0.0622	9.94	0.996	0.39 %
48 083	0.0312	9.97	1.0002	0.02 %
190 889	0.0156	9.98	0.9995	0.05 %

Table 2.2: Cantilever beam under tip force: Newton solve vs. Euler-Bernoulli with effective length $L_{\text{eff}} = L - w_{\text{band}}$, variable band clamp. Rows are ordered coarsest to finest; vertex count identifies each mesh.

n_{verts}	$\bar{h}_{\text{edge}}$	$\lvert w\rvert$	$\lvert w\rvert/w_{\text{ref}}$	rel. err.
414	58.9	2.172×10^{-5}	1.190	19.0 %
1 550	29.7	2.187×10^{-5}	1.198	19.8 %
6 162	14.7	1.953×10^{-5}	1.070	7.01 %
23 794	7.45	1.858×10^{-5}	1.018	1.83 %
93 891	3.74	1.834×10^{-5}	1.005	0.490 %
187 768	2.64	1.817×10^{-5}	0.996	0.404 %
265 816	2.22	1.818×10^{-5}	0.997	0.346 %
374 282	1.87	1.825×10^{-5}	1.000	0.006 %
529 660	1.57	1.828×10^{-5}	1.002	0.168 %
746 892	1.32	1.827×10^{-5}	1.001	0.103 %

Table 2.3: Pinched cylinder: radial deflection magnitude $|w|$ at the pinch point versus the analytical reference $w_{\text{ref}} = 1.82488 \times 10^{-5}$ [18]. Rows are ordered coarsest to finest. $\bar{h}_{\text{edge}}$ is the average edge length.

and $y = L$ constrain the in-plane displacement ($u_x = u_z = 0$) while leaving the axial displacement free. The diaphragm condition is enforced as a single row pin constraint, and no effective-length correction is applied. The reference quantity is the magnitude of the radial deflection at each pinch point. We use the established target $|w|_{\text{ref}} = 1.82488 \times 10^{-5}$ [18]. The peak deflection is $\sim 6 \times 10^{-6}$ times the shell thickness, placing the response in the typical linear regime.

Table 2.3 summarizes the results across ten mesh refinements. The convergence trajectory has two distinct regimes. Across the coarser meshes, the ratio $|w|/w_{\text{ref}}$ descends monotonically from $\sim$ 1.20 down through $\sim$ 1.02. Refining further,

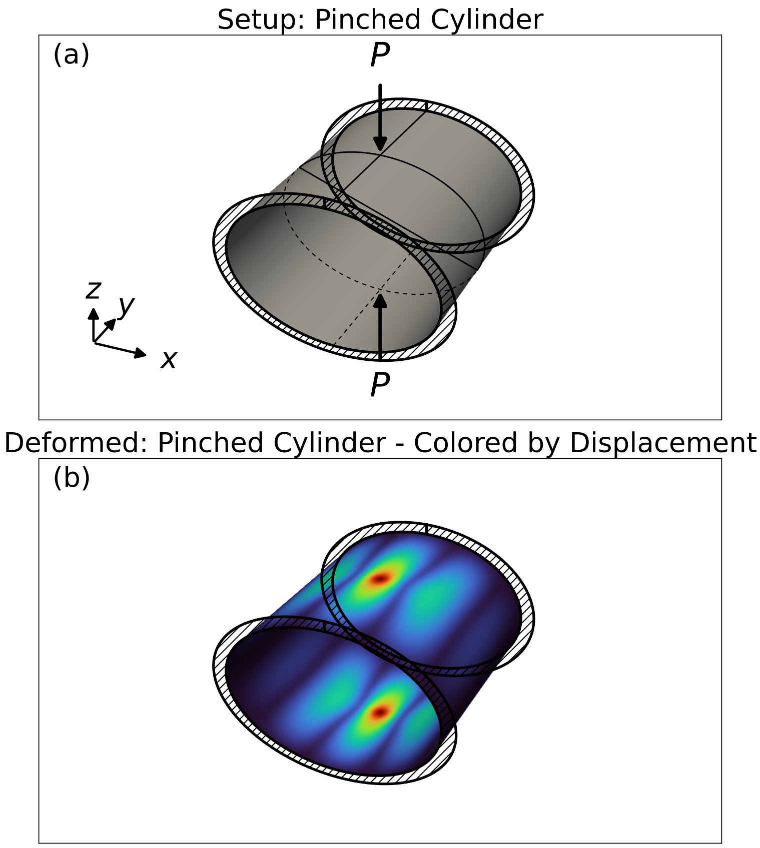

Figure 2.4: The pinched cylinder (a) consists of a closed cylindrical shell of radius R and length L, aligned along the y axis, with the circular cross-section in the xz-plane. The two ends are supported, with constraints against displacement in the x and z directions. Two equal and opposite point loads P are applied at midspan: one at the top of the cylinder ($+z$) and one at the bottom ($-z$). The deformed state (b) shows the radial deflection pattern from our discrete shell solver, with displacement magnified for visibility and colored by displacement magnitude.

beyond approximately 100k vertices, the trajectory enters a fine-mesh regime in which $|w|/w_{\text{ref}}$ oscillates within $\pm 0.5\%$ of unity. It approaches from above the analytical value, then dips below the reference, and crosses the same value again further on, as shown in Figure 2.5. The relative error is shown in Figure 2.2c. We do not observe a standard power law with refinement. A least-squares fit over the finest five meshes excluding the 374k-vertex point (where the trajectory crosses the reference value, resulting in a deceivingly small relative error) gives an observed order $p \approx 1.5$. The observed rate sits between $O(h)$ and $O(h^2)$.

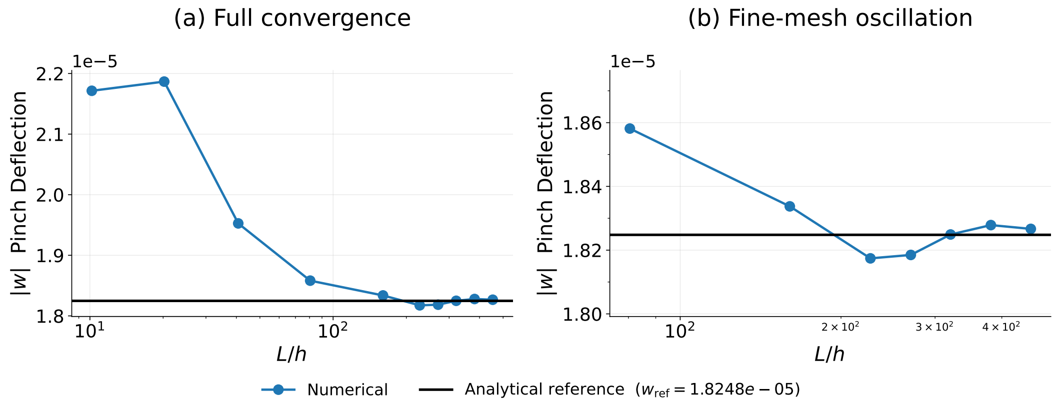

Figure 2.5: The deflection at the point load for the pinched cylinder is the reference value of interest. Panel (a) plots the full mesh range, where the deflection initially descends monotonically, reducing the over prediction of deflection, heading toward the analytical reference (horizontal black line). Panel (b) zooms into the finer mesh region, where the deflection trajectory oscillates around the reference value, reducing the relative error.

n_{verts}	w_{band}	R_{eff}	$w_{\text{num}}/w_{\text{ana}}$	rel. err.
123	0.372	0.814	0.726	27.4 %
419	0.194	0.903	0.878	12.2 %
1 586	0.0977	0.951	0.953	4.7 %
6 011	0.0497	0.975	0.979	2.1 %
23 691	0.0249	0.988	0.990	1.0 %
94 004	0.0125	0.994	0.995	0.45 %
373 420	0.00623	0.997	0.998	0.23 %
751 536	0.00440	0.998	0.9985	0.15 %

Table 2.4: Clamped circular plate under center point load: center deflection vs. Kirchhoff thin-plate solution with effective radius $R_{\text{eff}} = R - \frac{1}{2}w_{\text{band}}$. Rows are ordered coarsest to finest; vertex count identifies each mesh.

Clamped circular plate under center point load

The final benchmark we test is a flat circular plate of radius $R = 1$, thickness $t = 0.01$, $E = 10^7$, $\nu = 0.3$, loaded by a concentrated force $P = 10^{-4}$ at its center and clamped on the entire circumference (setup and deformed state shown in Figure 2.6). The Kirchhoff thin-plate reference solution for small deflection is [3]

$$w_{\text{center}} = -\frac{PR^2}{16\pi D}, \qquad D = \frac{Et^3}{12(1-\nu^2)}. \tag{2.13}$$

As with the other benchmarks, the clamped boundary is enforced on a band of rim nodes rather than a single ring, and the analytical reference is evaluated with the

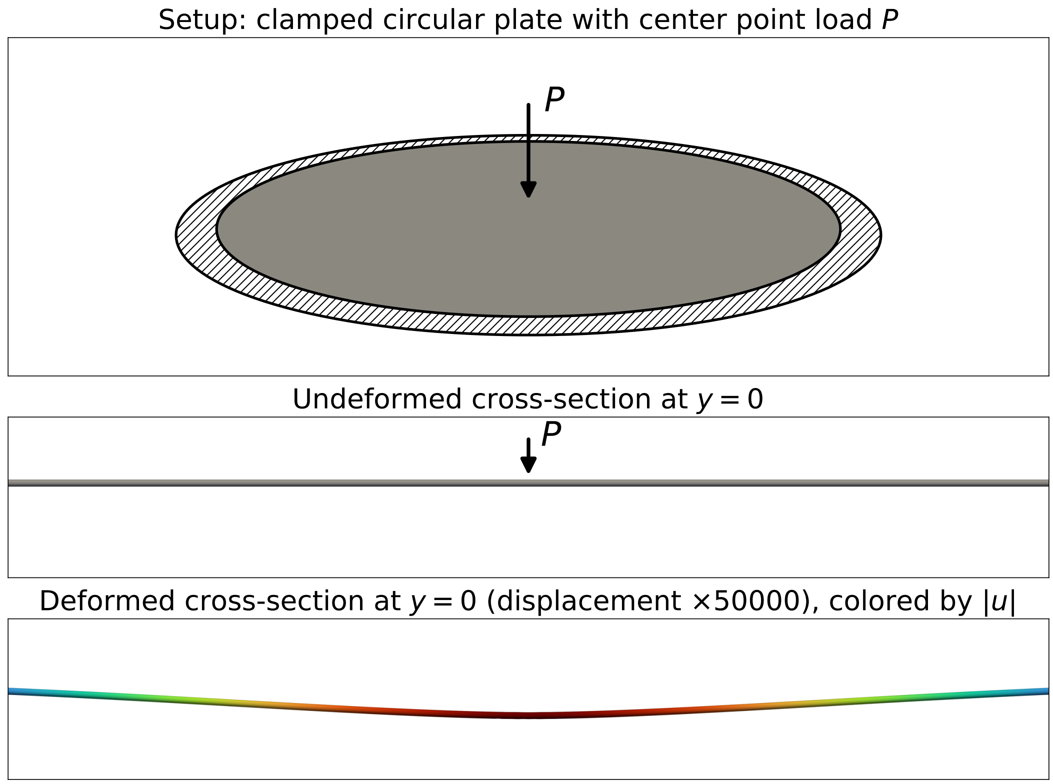

Figure 2.6: Clamped circular plate benchmark. Top: perspective view of the flat disc with clamped rim (hatched annulus) and central point load P. Middle/bottom: cross-section at $y = 0$ before and after loading (displacement magnified $\times 5 \times 10^4$), colored by displacement magnitude $|u|$. The rim clamp spans a two-row band of width w_{band}, so the analytical reference uses effective radius $R_{\text{eff}} = R - \frac{1}{2} w_{\text{band}}$.

corresponding effective radius $R_{\text{eff}} = R - \frac{1}{2} w_{\text{band}}$. Table 2.4 reports the displacement of the center, which approaches the Kirchhoff reference monotonically from below with clean $O(h)$ behavior, as seen in Figure 2.2d. This is because the band clamp trims an $O(h)$ ring off the load-bearing domain, so the computed deflection is systematically softer than the analytical reference (which assumes an ideal point clamp at the rim) and recovers it as the band vanishes.

Summary

Figure 2.2 aggregates the convergence data across all four benchmarks. The patch test and flat-cantilever benchmarks converge at $O(h)$, with the cantilever reaching relative errors below 0.1% by ∼48k vertices. The clamped circular plate converges at approximately linear order ($p \approx 1.1$), comparable to the flat benchmarks. The analytical reference in the plate table is already evaluated at the reduced effective domain $R_{\text{eff}} = R - \frac{1}{2}w_{\text{band}}$, so the residual rate is not an uncorrected domain-size effect; it reflects the fact that the band-clamp correction itself is only first-order accurate. Substituting R_{eff} in the analytical reference captures the leading-order shift of the support inward by $w_{\text{band}}/2$, but the ideal clamp and the discrete band clamp still differ in how they transfer load into the interior: the ideal clamp enforces zero rotation on an infinitely thin line, while the discrete clamp does so across a band of width $2\bar{h}_{\text{edge}}$. This residual structural difference produces an $O(h)$ mismatch in the computed deflection that vanishes only as the band shrinks with $h \to 0$. The pinched cylinder converges faster, with $p \approx 1.5$ over the finest five meshes (excluding the 374k-vertex alignment point), where the single-row pin diaphragm and the midspan point-load determine the rate. Together, these rates reflect the boundary mechanics specific to each benchmark, rather than a limitation of the discrete energy itself.

2.5 Conclusion

This chapter describes the discrete-shell framework used throughout the thesis. The Kirchhoff-Love energy is discretized on a triangulated mesh. The stretching energy is a Neo-Hookean model using the discrete first fundamental form, and the bending energy is a quadratic function of the discrete second fundamental form.

The verification benchmarks of Section 2.4 demonstrate that the discrete energy is consistent with a continuum shell PDE. The Newton solver converges across mesh refinement, and the formulation reproduces classical shell reference solutions with refinement.

References

[1] Basile Audoly and Yves Pomeau. "Elasticity and geometry". In: *Peyresq Lectures on Nonlinear Phenomena*. World Scientific, 2000, pp. 1–35.

[2] Junuthula Narasimha Reddy. *Theory and analysis of elastic plates and shells*. CRC press, 2006.

[3] Stehan Timoshenko. "Theory of plates and shells". In: *McGRAWC HILL* (1959).

[4] L. Angela Mihai and Alain Goriely. "A plate theory for nematic liquid crystalline solids". In: *Journal of the Mechanics and Physics of Solids* 144 (2020), p. 104101. ISSN: 0022-5096. DOI: `https://doi.org/10.1016/j.jmps.2020.104101`.

[5] Lucas Bouck, David Padilla-Garza, and Paul Plucinsky. *Plate theory for metric-constrained actuation of liquid crystal elastomer sheets*. 2024. eprint: `arXiv:2410.00333`.

[6] August Föppl. *Vorlesungen über technische Mechanik*. Vol. 6. BG Teubner, 1921.

[7] Th V Kármán. "Festigkeitsprobleme im maschinenbau". In: *Mechanik* (1907), pp. 311–385.

[8] David Baraff and Andrew Witkin. "Large steps in cloth simulation". In: *Proceedings of the 25th Annual Conference on Computer Graphics and Interactive Techniques*. SIGGRAPH '98. New York, NY, USA: Association for Computing Machinery, 1998, pp. 43–54. ISBN: 0897919998. DOI: 10.1145/280814.280821. URL: https://doi.org/10.1145/280814.280821.

[9] Eitan Grinspun et al. "Discrete Shells". In: *Proceedings of the 2003 ACM SIGGRAPH/Eurographics Symposium on Computer Animation*. SCA '03. San Diego, California: Eurographics Association, 2003, pp. 62–67. ISBN: 1581136595.

[10] Keenan Crane. "Discrete differential geometry: An applied introduction". In: *Notices of the AMS, Communication* 1153 (2018).

[11] Hsiao-Yu Chen et al. "Physical Simulation of Environmentally Induced Thin Shell Deformation". In: *ACM Transactions on Graphics* 37.4 (July 2018). ISSN: 0730-0301. DOI: 10.1145/3197517.3201395. URL: https://doi.org/10.1145/3197517.3201395.

[12] Clarisse Weischedel. "A discrete geometric view on shear-deformable shell models". PhD thesis. Universität Göttingen, 2012. URL: https://api.semanticscholar.org/CorpusID:119867289.

[13] Weicheng Huang et al. "Discrete differential geometry-based model for nonlinear analysis of axisymmetric shells". In: *International Journal of Mechanical Sciences* 283 (2024), p. 109742. DOI: 10.1016/j.ijmecsci.2024.109742. URL: https://www.sciencedirect.com/science/article/pii/S0020740324007835.

[14] J. Kiendl et al. "Isogeometric shell analysis with Kirchhoff–Love elements". In: *Computer Methods in Applied Mechanics and Engineering* 198.49–52 (2009), pp. 3902–3914. DOI: 10.1016/j.cma.2009.08.013. URL: https://www.sciencedirect.com/science/article/abs/pii/S0045782509002680.

[15] Warner Tjardus Koiter. "On the nonlinear theory of thin elastic shells". In: *Proc. Koninkl. Ned. Akad. van Wetenschappen, Series B* 69 (1966), pp. 1–54.

[16] Javier Bonet and Richard D. Wood. *Nonlinear Continuum Mechanics for Finite Element Analysis*. Cambridge University Press, 1997.

[17] Bruce M. Irons and Abdur Razzaque. "EXPERIENCE WITH THE PATCH TEST FOR CONVERGENCE OF FINITE ELEMENTS". In: *The Mathematical Foundations of the Finite Element Method with Applications to Partial Differential Equations*. Ed. by A.K. Aziz. Academic Press, 1972, pp. 557–

587. ISBN: 978-0-12-068650-6. DOI: https://doi.org/10.1016/B978-0-12-068650-6.50025-3. URL: https://www.sciencedirect.com/science/article/pii/B9780120686506500253.

[18] Fehmi Cirak, Michael Ortiz, and Peter Schröder. "Subdivision surfaces: a new paradigm for thin-shell finite-element analysis". In: *International Journal for Numerical Methods in Engineering* 47 (2000). DOI: 10.1002/(SICI)1097-0207(20000430)47:123.0.CO;2-1. URL: http://www.multires.caltech.edu/pubs/thinshell.pdf.

Chapter 3

PHOTOACTIVE LIQUID CRYSTAL ELASTOMER SHELLS

3.1 Introduction

Liquid crystal elastomers are crosslinked polymer networks which incorporate rod-like liquid crystal molecules (mesogens) into their polymer chains [1]. These materials undergo an isotropic to nematic transformation accompanied by a large shape change. When photoactive molecules are embedded into the polymer structure, liquid crystal elastomers undergo a light-induced deformation due to the illumination-controlled *trans*-to-*cis* isomerization of these molecules [2–4]. Azobenzene is a common choice for photomechanically functionalizing liquid crystal elastomers because it has a high absorption coefficient across various wavelengths with fast photo-chemistry [5]. Lower wavelengths (~300-400nm) of ultraviolet light induces to *trans*-to-*cis* isomerization while visible illumination (>400nm) reverses the process, causing *cis*-to-*trans* isomerization. These transitions couple with the nematic order of the liquid crystal elastomer, resulting in photomechanically-induced deformation. The azobenzene molecules are linear in shape in the *trans* state, and bent in shape in the *cis* state. Consequently, the *t*rans state promotes the nematic order in the liquid crystal elastomer while the *c*is state reduces the nematic order. Further, illumination with linearly polarized light selectively isomerizes the appropriately oriented azobenzene molecules, further promoting nematic director alignment. This change in nematic order and director alignment is accompanied by spontaneous stretch.

When a sheet of photomechanically active material is illuminated, the light intensity decreases with depth as it absorbed, resulting in limited penetration. When the penetration depth is small, the intensity is described by Beer's law

$$I = I_0 e^{-\frac{x}{d}}, \tag{3.1}$$

where I_0 is the light intensity at the illuminated surface, x is the position within the material (where $x = 0$ corresponds to the surface of illumination), and d is the penetration depth [6]. The photo-isomerization decays throughout the thickness, and consequently, the deformation decays as well, resulting in the sheet bending [6–8]. When the penetration depth is large, there can be non-monotone dependence on illumination [6, 9]. In this chapter, we assume shallow penetration and the Beer's limit.

The light-induced bending deformation leads to a non-local shape change, which in turn alters the illumination conditions across the deformed structure. This phenomenon creates complex deformations of a photomechanical strip under illumination [3]. Gelebart *e*t al. [10] exploited this behavior to generate light-induced, periodic flapping of a doubly clamped liquid crystal elastomer film, and proposed that such motion can be used for a remotely actuated walker. Korner *e*t al. [8] developed a theoretical model which demonstrated how steady illumination can give rise to periodic motion. However, these studies have focused on one-dimensional strips and beams.

In this chapter, we study photomechanically active sheets and shells, or two-dimensional structures. The behavior of such structures is expected to be more complex due to the inherent coupling between stretching and bending, as a consequence of Gauss's remarkable theorem [11]. In recent years, the thermally induced shape-morphing of sheets and shells has been the topic of intense interest [12–16]. Applying heat to liquid crystal elastomer sheets with a patterned director gives rise to non-uniform spontaneous stretch, resulting in out-of-plane deformations. In contrast, photomechanical actuation induces spontaneous bending, altering the Gauss curvature and, consequently, the stretch. This coupling can give rise to instabilities, necessitating care when studying these deformations.

We apply this method to a series of examples involving photomechanical sheets and shells to demonstrate the richness of phenomena associated with the interplay between photoactuation, bending, and stretching. A noteworthy example is one where a shell follows the source of illumination, much like a sunflower follows the sun.

3.2 Photomechanical spontaneous curvature

The discrete-shell formulation of Chapter 2 represents a material's preferred shape through the spontaneous curvature h^* in its bending energy. We are interested in photomechanically active materials, where one can induce a spontaneous curvature with illumination [8, 17], and therefore we take

$$h^* = \overline{h} - \kappa(t), \quad \tau\dot{\kappa} = \alpha\tilde{I}(m \cdot n)\kappa_0, \quad \kappa(0) = 0, \tag{3.2}$$

where m is the light propagation direction, κ_0 is the unit spontaneous curvature depending on the symmetry of material, $\alpha = c_p G$ is a material and geometry dependent constant where c_p is the photo-compliance (defined as the contractile strain accumulated along the nematic director per unit intensity [18]), G is a geometric

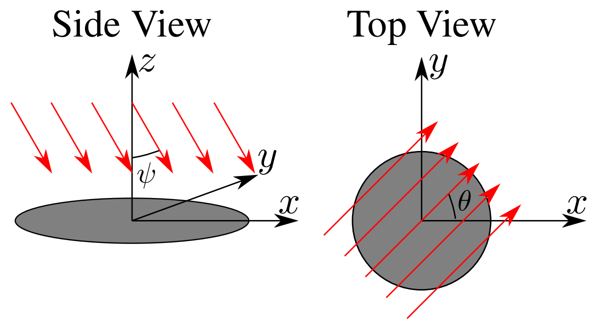

Figure 3.1: The light illuminates a disc set in the $x - y$ plane, with ψ denoting the angle of illumination relative to the vertical z axis, and θ denoting the projection of the illumination in the $x - y$ in-plane relative to the x axis.

factor, τ is the relaxation time (defined as the inverse of the thermal decay rate of *cis* azobenzene molecules), $\tilde{I}$ is the intensity of illumination, and $\overline{h}$ is the curvature of the structure in the absence of illumination. In this chapter, we consider a fixed time, and therefore take $\kappa = \alpha\tilde{I}(m \cdot n)\kappa_0$. Since n is the normal to the surface in the current configuration, it and consequently κ changes with deformation.

3.3 Flat reference: Isotropic spontaneous curvature

Flat reference

We consider a flat thin circular film with diameter 2 cm and thickness 30 μm unless otherwise specified. We discretize the domain with 12417 nodes, or 37251 degrees of freedom. We illuminate the entire film with a wide circularly polarized parallel beam propagating in a direction

$$m = \{\sin\psi\cos\theta, \sin\psi\sin\theta, -\cos\psi\}, \tag{3.3}$$

where ψ is the angle from the vertical z axis, and θ denotes an arbitrary direction in the $x - y$ plane, as shown in Figure 3.1. We non-dimensionalize the length with the film radius r, take $\alpha = 0.194$ m/W [8], and non-dimensionalize the intensity as $I = \tilde{I}/\bar{I}$, with reference intensity $\bar{I} = 515$ W/m^2, so the common intensity used in this chapter is $I = 1$ in non-dimensional units.

We start with a film synthesized in the isotropic state such that $\kappa_0 = \mathrm{Id}_2$.

Normal illumination

We take $m = \{0, 0, -1\}$ such that the illumination is normal to the initial flat state. We start with a (non-dimensional) illumination intensity of $I = 0$ and gradually increase it to $I = 1$. We fix five nodes at the center of the sheet to simulate a

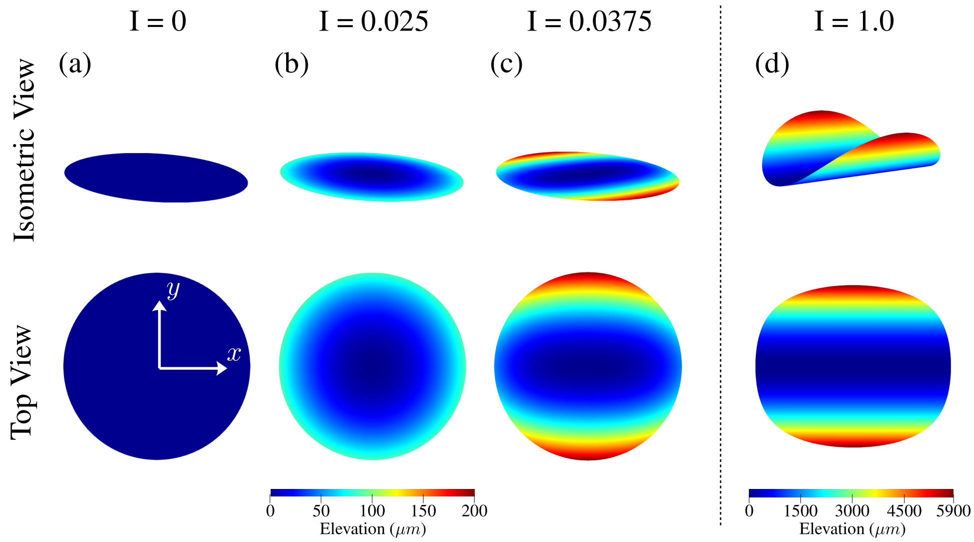

Figure 3.2: A flat isotropic liquid crystal elastomer sheet is illuminated vertically source of light. The reference state at intensity (a) $I = 0$ is a flat sheet. When increasing the light intensity to (b) $I = 0.025$, the film edges begin to curve up due to the increase in spontaneous curvature. Further increasing the light intensity to (c) $I = 0.0375$ results in a large buckling deformation, and the film morphs into a cylindrical shell. Further increasing the light intensity to (d) $I = 1.0$ increases the spontaneous curvature, further elevating the edges of this cylindrical shell.

clamped flat constraint at the center. The results are shown in Figure 3.2.

When the light is turned on, spontaneous curvature increases, driving the system towards forming a spherical bowl of uniform curvature. However, this deformation induces a change in Gauss curvature and, consequently, stretch (according to Gauss's Theorema Egregium [11]). Since the stretching energy scales with thickness while bending scales with thickness cubed, the stretching behavior dominates in thin shells. Therefore the stretching energy suppresses the curvature, leading to a flat sheet with the edges curved up, as shown at $I = 0.025$ (Figure 3.2(b)). The sheet eventually bifurcates into a cylindrical shape, again to minimize stretch, at $I = 0.0375$ (Figure 3.2(c))[1]. Post bifurcation, the deformed shell retains this cylindrical shape, and the curvature continues to increase with illumination, shown at $I = 1$ (Figure 3.2(d)). This bifurcation to a cylindrical shape is consistent with other works regarding thermally induced spontaneous curvature [19, 20].

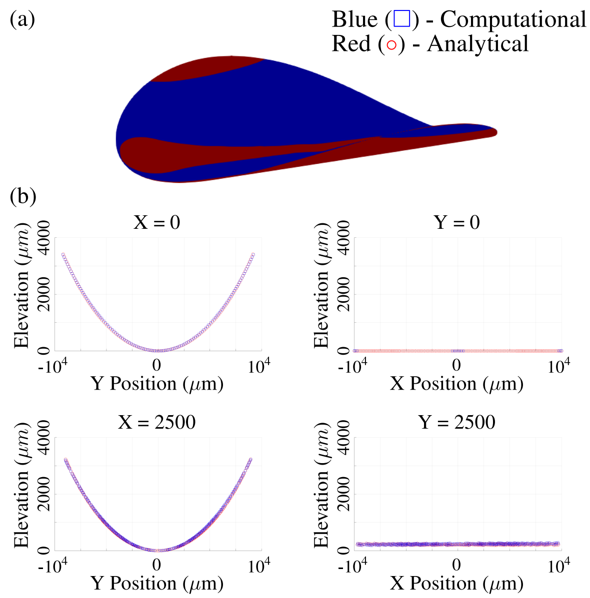

Figure 3.3: (a) The deformation computed from the discrete shell computational model is shown in blue, overlain with the deformation computed analytically in red. Cross-sections comparing the position of the analytical deformation to the computational result are shown in (b), at $\tilde{x} = 0, 0.25$ and $\tilde{y} = 0, 0.25$.

Analytic model

We briefly examine the post-buckled shape using a simple analytic model. Informed by the observations made from Figure 3.2, we make the ansatz that the shell deforms to a perfect cylinder with zero stretch, and minimize the energy over the cylinder radius ρ to obtain the deformed shape.

Let x, y parameterize the disc (such that $\eta^1 = x, \eta^2 = y$ in the notation of Chapter 2), and we assume that the shell deforms such that the axis of the cylinder is parallel to the x-axis. We may then respectively write the deformation, curvature, and spontaneous curvature as:

$$r = \begin{pmatrix} x \\ \rho \sin \frac{y}{\rho} \\ \rho \left(1 - \cos \frac{y}{\rho}\right) \end{pmatrix}, \quad h = \frac{1}{\rho} \begin{pmatrix} 0 & 0 \\ 0 & 1 \end{pmatrix}, \quad h^* = I \cos \frac{y}{\rho} \begin{pmatrix} 1 & 0 \\ 0 & 1 \end{pmatrix}, \tag{3.4}$$

The total energy consists only of the bending contribution:

$$\mathcal{E} = \frac{Eh^3}{12} \int_{-1}^{1} \int_{-\sqrt{1-y^2}}^{\sqrt{1-y^2}} \frac{\nu}{2(1-\nu^2)} \left(\operatorname{tr}(\tilde{h})\right)^2 + \frac{1}{2(1+\nu)} \operatorname{tr}(\tilde{h}^2)\, dx dy, \tag{3.5}$$

[1]The orientation of the axis of the cylindrical shell is arbitrary, depending on mesh and perturbations in the simulation.

where

$$\tilde{h} = h - h^* = \begin{pmatrix} -I\cos\frac{y}{\rho} & 0 \\ 0 & \frac{1}{\rho} - I\cos\frac{y}{\rho} \end{pmatrix} \tag{3.6}$$

is the bending matrix. We fix $I = 0.5$, and minimize this energy over the cylinder radius ρ to obtain the deformed shape. We compare the results of this simplified analytical model to the complete computational model, with the results shown in Figure 3.3. Figure 3.3(a) depicts the deformations for illumination intensity $I = 0.5$. We plot various cross-sections of the two deformations in Figure 3.3(b). The error between the total energy computed for the analytical deformation relative to the computationally-computed deformation is 8.1%. Visually, we see excellent agreement between the analytical and computational deformations. Therefore, this simple analytic model is able to accurately capture the deformed shape of the cylinder.

Illumination Direction

We now break the in-plane isotropy by slanting the direction of illumination from the vertical. We study two boundary conditions, one where a small region (five nodes) in the center is clamped flat like the previous cases, and a second condition where the sheet is allowed to pivot using an elastic hinge joint (one node fixed and four nodes fitted with elastic springs) attached to the center point.

Center clamped

We begin with the case where the five nodes nearest to the center are fixed (clamped flat). We illuminate the sheet at an angle $\psi = 30°$ from the vertical and $\theta = 0°$ in-plane direction, with the resulting deformation shown in Figure 3.4. We observe a similar sequence as in the case of vertical illumination, with two key differences.

First, bifurcation occurs at a higher intensity for the angled light ($\psi = 30°$) at $I = 0.0375$, when compared to normal illumination ($\psi = 0°$) which occurs at $I = 0.0325$. A greater intensity is required because the angled light less directly illuminates the shell, resulting in a lower effective light intensity. Notably, the vertical component of the angled light at bifurcation is identical to the corresponding intensity for vertical illumination within 3 significant figures.

Secondly, the post-bifurcated shape is conical, and the axis of the cone is aligned with the direction of illumination. This conical deformation forms due to the non-zero angle of incidence of the illumination, which creates an energetically favorable

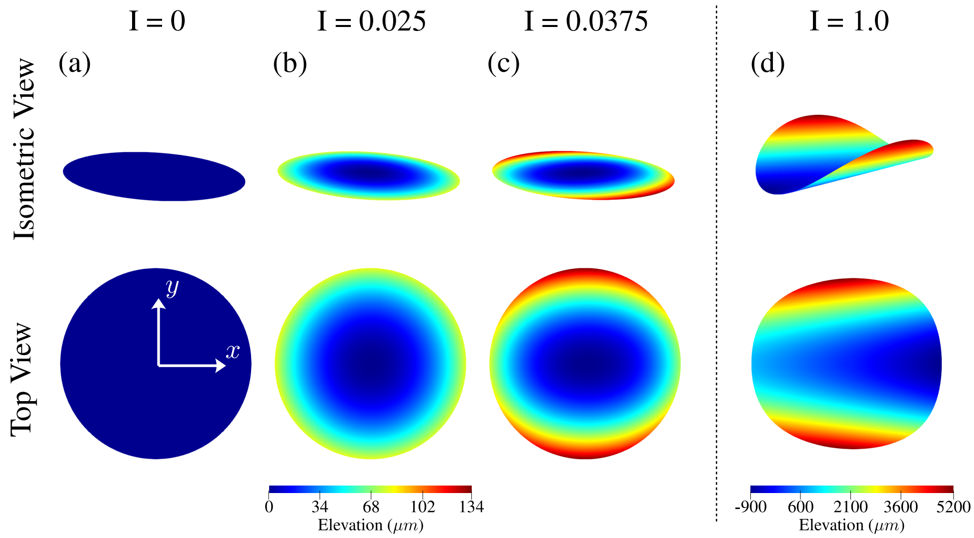

Figure 3.4: A flat isotropic liquid crystal elastomer sheet is illuminated from a parallel source of light angled $\psi = 30°$ from the vertical, along the x axis. The reference state at intensity (a) $I = 0$ is a flat sheet. Increasing the light intensity to (b) $I = 0.025$, the edges of the sheet begin to curve up due to the increase in spontaneous curvature. Further increasing the light intensity to (c) $I = 0.0375$ results in a large buckling deformation, and the film morphs into a cylindrical shell. Further increasing the light intensity to (d) $I = 1.0$ increases the spontaneous curvature, further elevating the edges of this cylindrical shell.

direction for the shell to bifurcate along. The spontaneous curvature is minimized when the illumination direction lies within the tangent space of the shell; bifurcating along the in-plane axis achieves said minimization.

We now compare the effects of varying the direction of illumination, both the in-plane angle θ and the vertical angle ψ. Figure 3.5 shows the post-bifurcated shape for the various illumination directions at $I = 1.0$. Figures 3.5(a-e) show that changing the in-plane direction θ controls the orientation of the conical deformation, but not the overall behavior. The spontaneous curvature is minimized when the edges of the conical deformation align parallel to the illumination. In short, the deformed cylinder follows the source of illumination, much like a sunflower tracks the sun's position.

Figures 3.5(f-j) show the effect of varying the vertical angle of illumination ψ. The phenomena remains similar qualitatively: a conical deformation emerges along the direction of the in-plane angle θ. However, as the angle of incidence increases, the magnitude of the deformation decreases. Note that $m \cdot n = \cos\psi$, and therefore, the effective illumination decreases with increasing ψ. We compare the critical

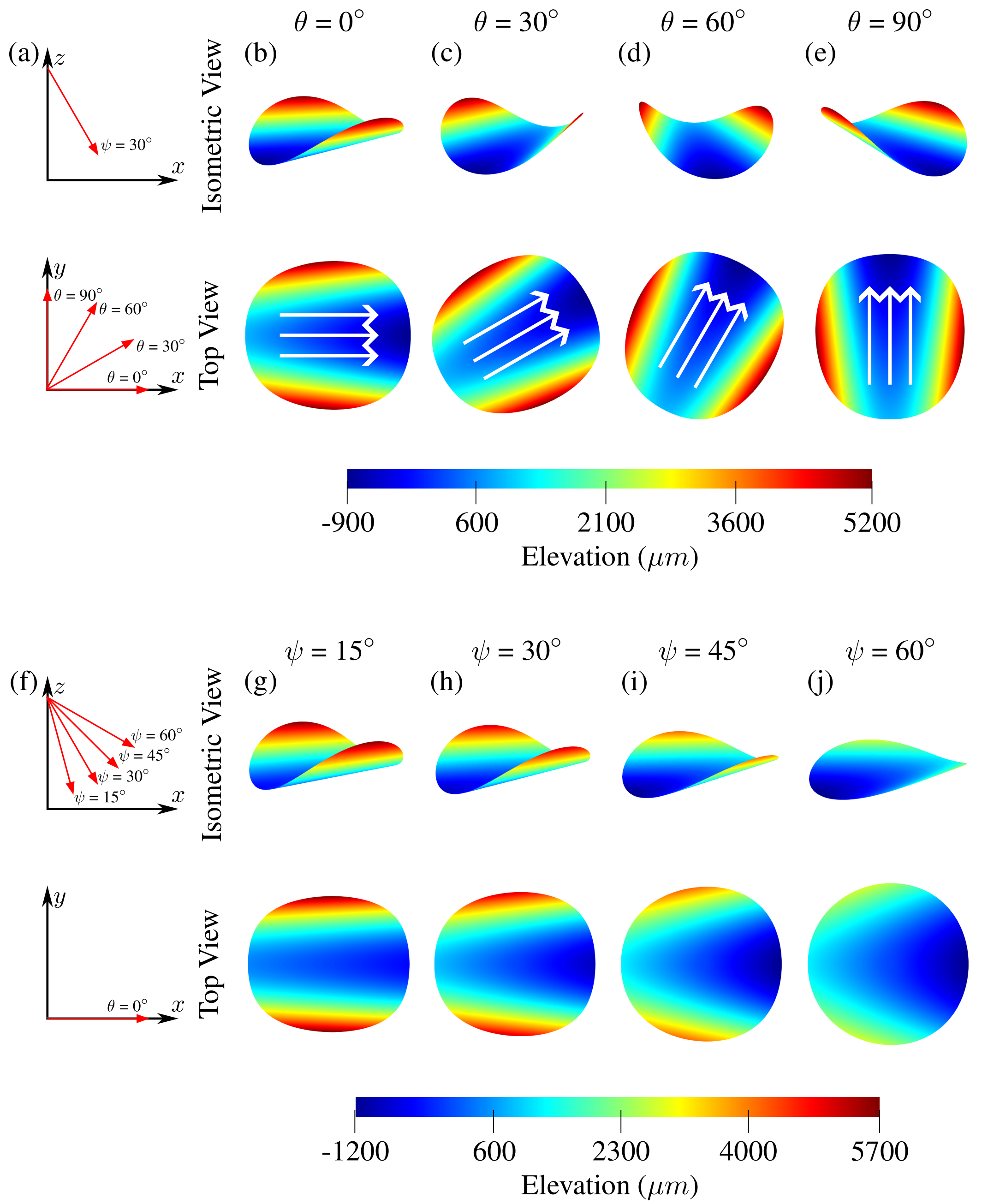

Figure 3.5: A flat sheet is illuminated from the (a) given orientation, corresponding to states (b)-(e). The light intensity and vertical angle are $I = 1.0$ and $\psi = 30°$ respectively. Further, (b)-(e) show an isometric view of the deformed states as well as a top-down view of the corresponding deformations. The in-plane $x - y$ component of the illumination is represented by the white arrows. The deformation aligns along in-plane angle θ equal to (b) 0°, (c) 30°, (d) 60°, and (e) 90°. Separately, a flat sheet is illuminated from the (f) given orientation, corresponding to states (g)-(j). The light intensity and in-plane angle are $I = 1.0$ and $\theta = 0°$ respectively. Further, (g)-(j) show an isometric view of the deformed states as well as a top-down view of the corresponding deformations. The deformations are shown for vertical angles ψ equal to (g) 15°, (h) 30°, (i) 45°, and (j) 60°.

Case	$\psi = 0°$	$\psi = 15°$	$\psi = 30°$	$\psi = 45°$	$\psi = 60°$
Flat	0.0325	0.0375	0.0375	0.0450	0.0625
Spherical	0.0575	0.0625	0.0650	0.0775	0.1100

Table 3.1: Critical intensity for bifurcation

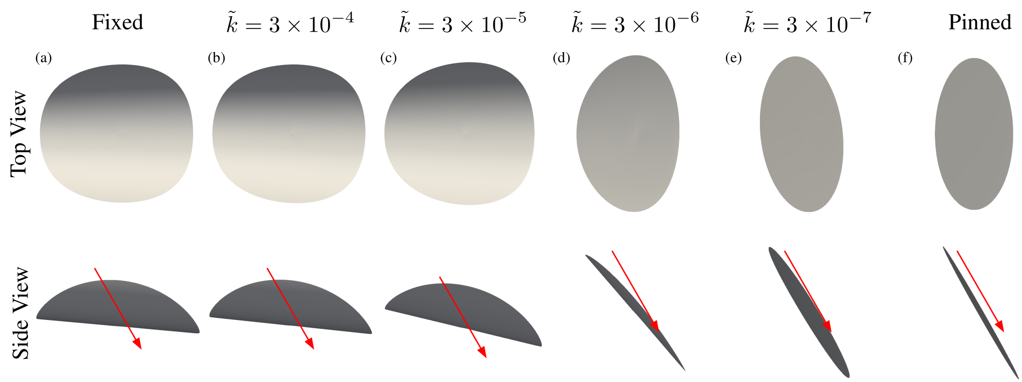

Figure 3.6: An artificial sunflower: a sheet with a pin joint at the center and torsional spring. The top view in the $x - y$ plane is shown in the top row, and the side view in the $x - z$ plane is shown in the bottom row. The deformation is shown for intensity $I = 1.0$, $\psi = 30°$ and $\theta = 0°$. We model a (a) fixed center, (b) $\tilde{k} = 3 \times 10^{-4}$, (c) $\tilde{k} = 3 \times 10^{-5}$, (d) $\tilde{k} = 3 \times 10^{-6}$, (e) $\tilde{k} = 3 \times 10^{-7}$, and (f) a pinned center. The direction of illumination is depicted by a red arrow.

value of intensity at which bifurcation occurs in Table 3.1. We observe that the critical intensity increases with ψ. As the light less directly illuminates the shell, the intensity required to achieve bifurcation increases.

Pinned: The artificial sunflower

We now alter the system constraints: we fix a single center point and attach springs to the four surrounding nodes to imitate a torsional spring. We modify the energy as

$$\tilde{\mathcal{E}}^{new} = \tilde{\mathcal{E}} + \frac{1}{2}\tilde{k}\sum_{i=1}^{4}|r^i - R^i|^2, \tag{3.7}$$

where $\tilde{\mathcal{E}}^{new}$ is the new energy to minimize, $\tilde{\mathcal{E}}$ is the non-dimensional energy, $\tilde{k}$ is the non-dimensional spring constant, and vertices i are the four nodes adjacent to the center. A torsional spring allows for rotation with an energy penalty dependent on the spring constant. We investigate this deformation for a fixed angle of incidence $\psi = 30°$. We model a fully clamped center (Figure 3.6(a)), torsional springs of varied strength (Figure 3.6(b-e)), and a pinned center (Figure 3.6(f)).

As the stiffness of the simulated elastic hinge decreases, the shell rotates further towards the light and undergoes a smaller bending deformation. For a fully pinned shell, there is zero deformation, just pure rotation. This behavior can be predicted from (3.2), as the change in spontaneous curvature scales with $m \cdot n$, and pure rotation can satisfy equilibrium with zero spontaneous curvature. Thus, these solutions reflect that for a specific value of spring constant, the sheet trades bending energy for spring energy; changing the spring constant can alter this balance.

We can exploit this behavior for various applications, such as fabricating self-aligning structures. Instead of expensive sensors and actuators, space structures can incorporate azobenzene-doped liquid crystal elastomers as passive alignment devices. One concrete example is thermal regulation on spacecrafts; radiators must be appropriately oriented to reject excess heat into dead space. Incorporating liquid crystal elastomers can allow for the replacement of expensive, manually-controlled actuation systems with passive alignment mechanisms, enabling radiators to automatically adjust their alignment for optimal heat rejection.

3.4 Flat reference: Patterned director

Various researchers have developed techniques to synthesize nematic liquid crystal elastomer films with a specified director orientation in the natural reference state [14, 21–23]. Such films have been extensively studied for thermal actuation, where altering the temperature leads to spontaneous stretch [24]. However in this chapter, we hold the temperature constant, resulting in zero spontaneous stretch. Instead, we examine systems where illumination generates anisotropic spontaneous curvature determined by the written director orientation. In particular, we consider unit spontaneous curvature

$$\kappa_0 = \hat{d} \otimes \hat{d} - \frac{1}{2}\hat{d}^{\perp} \otimes \hat{d}^{\perp}, \tag{3.8}$$

where $\hat{d}$ is the local orientation of the liquid crystal director, and $\hat{d}^{\perp}$ is the perpendicular in-plane direction with respect to the director. Consequently, the film is anisotropic. Additionally, the director does not have to be uniform across the film. We model a similar problem as before: shining light at a liquid crystal elastomer sheet clamped at the center.

Circular Sheet with Azimuthal Defect

We consider a liquid crystal elastomer film with a director field having a +1 azimuthal defect, illustrated in Figure 3.7(a). The pattern and the illumination are axisymmetric in-plane, resulting in an initially axisymmetric deformation. Similar to the isotropic

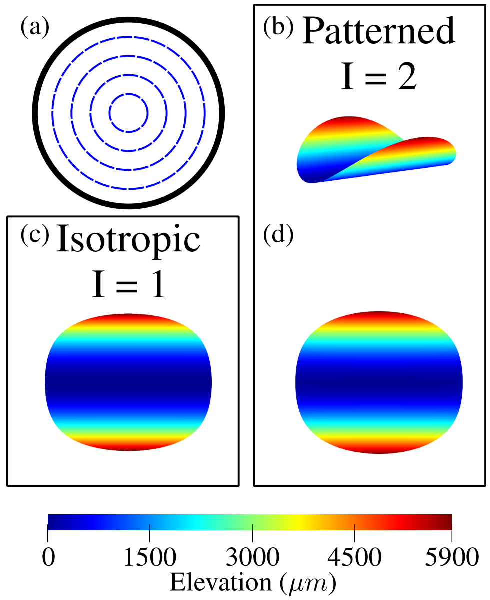

Figure 3.7: (a) We program a +1 azimuthal defect into a flat disc. The illumination is directly vertical with $\psi = 0°$. The patterned sheet is then illuminated to $I = 2.0$ (b)(d). We compare the deformation of the patterned sheet to the deformation of the isotropic film (c) at lower intensity $I = 1$.

disc, the film bifurcates into a cylindrical shell at a critical intensity, with the final deformation shown in Figures 3.7(b,d) for intensity $I = 2$. However, the curvature is smaller than that of the isotropic sheet: Figure 3.7(c) shows the result for an isotropic sheet at lower intensity $I = 1$. The unit spontaneous curvature κ_0 in the patterned film causes positive bending along one direction and negative curvature in the perpendicular direction. This difference in the bending directions reduces the effective spontaneous curvature relative to the isotropic film.

Rectangular Sheet with Constant Director Orientation

We now turn to the seminal experiments of Yu *et al.* [7], who used linearly polarized light to illuminate a rectangular sheet, with Figure 3.8(a) adapted from their work. We consider various uniform director patterns over rectangular liquid crystal films, depicted in Figure 3.8(b). The uniform alignment of the director field imitates the effect of linearly polarized light illuminating an isotropic film. By varying the alignment of the director field by 45° and using a circularly polarized light source, we can replicate the effects of varying the linear polarization of a light source over an isotropic film.

We consider a rectangular sheet 2 cm by 1.3 cm with a 0.5 cm diameter circular

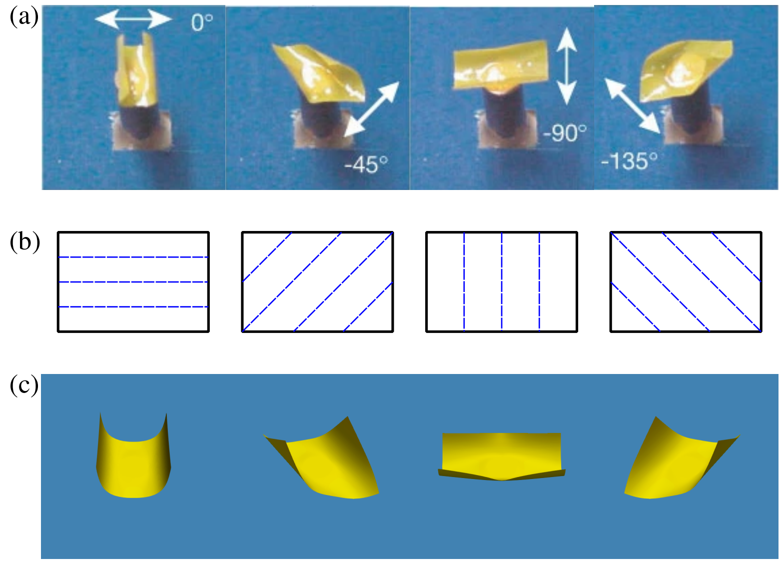

Figure 3.8: The (a) experiments from Yu *et al.* [7] are shown for various linear polarizations of light. Rather than using linearly polarized light, circularly polarized light is used to illuminate various liquid crystal elastomer sheets with (b) constant patterned director orientations. The (c) resulting deformations are shown for $I = 5.0$.

region clamped flat. We discretize the domain with 10965 nodes, or 32895 degrees of freedom. The simulation results for the given director orientations are shown in Figure 3.8(c). The film bends perpendicular to the director orientation, due to the contraction along that direction. We observe good qualitative agreement between these simulations and the experimental observations.

It is worth noting that Yu *et al.* varied the polarization direction of light over a constant isotropic film, while we maintained a circularly polarized illumination source and varied the director orientation. These setups are functionally equivalent, as both approaches control the relative alignment between the nematic director and polarized light.

3.5 Shells

We now examine the deformation of curved shells, which have an inherent curvature prior to illumination. Therefore, the spontaneous curvature will have a contribution from both the photo-responsive behavior and the reference geometry of the shell.

Spherical Cap

We consider the deformation of a spherical cap, under similar conditions as previous analysis: the shell is an isotropic liquid crystal and the center is clamped flat. The

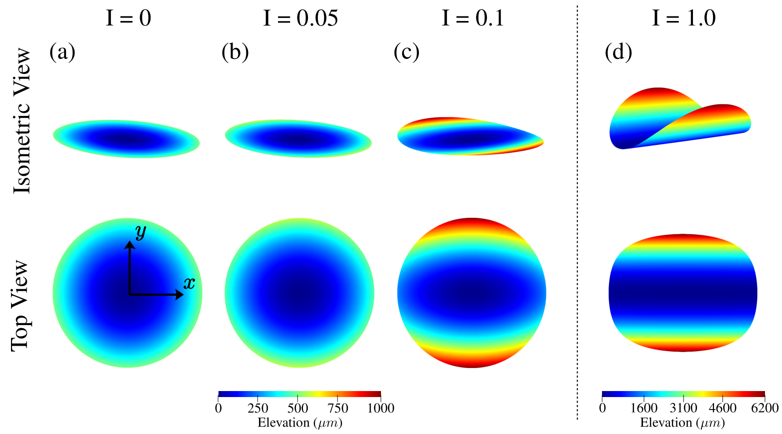

Figure 3.9: A curved spherical shell made from an isotropic liquid crystal elastomer is illuminated from a directly vertical source of light. The reference state at intensity (a) $I = 0$ is a flat sheet. Increasing the light intensity to (b) $I = 0.05$, the edges of the sheet begin to curve up due to the increase in spontaneous curvature. Further increasing the light intensity to (c) $I = 0.1$ results in a large buckling deformation and the spherical cap morphs into a cylindrical shell. Further increasing the light intensity to (d) $I = 1.0$ increases the spontaneous curvature, further elevating the edges of this cylindrical shell.

spherical cap has diameter 2 cm and thickness 30 μm, and has radius of curvature 10.025 cm. We discretize the domain with 12417 nodes, or 37251 degrees of freedom.

We illuminate the spherical cap vertically, starting with illumination intensity $I = 0$ and gradually increasing to $I = 1.0$. The results are shown in Figure 3.9. The initial behavior is qualitatively similar to the normal illumination of a flat sheet (Figure 3.2): the edges of the shell rise up in the shape of a cap, and upon some reaching some critical intensity, the shell bifurcates into a cylindrical shape. However, the intensity required for bifurcation is greater for the spherical cap when compared to the flat sheet, as shown in Table 3.1. This increased critical intensity arises from the inherent reference curvature of the spherical cap, which provides additional rigidity [25]. Figure 3.11 plots the bifurcation intensity as a function of reference radius of curvature. The behavior as we vary the angle of illumination is also similar as in the case of a sheet, as shown in Figure 3.10. The corresponding energy decomposition into stretching and bending contributions is shown in Figure 3.12.

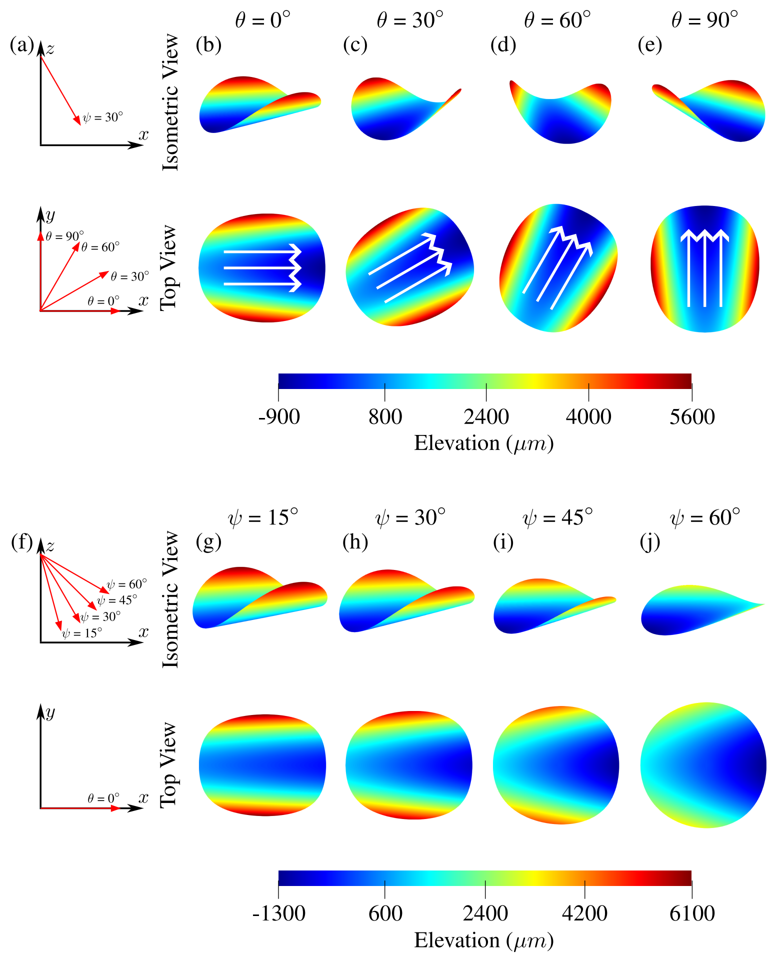

Figure 3.10: A spherical shell is illuminated from the (a) given orientation, corresponding to states (b)-(e). Further, (b)-(e) show an isometric view of the deformed states as well as a top-down view of the corresponding deformations. The in-plane $x - y$ component of the illumination is represented by the white arrows. The deformation aligns along the (b) 0°, (c) 30°, (d) 60°, and (e) 90° in-plane angle θ. The light intensity and vertical angle are $I = 1.0$ and $\psi = 30°$ respectively. A spherical shell is illuminated from the (f) given orientation, corresponding to states (g)-(j). Further, (g)-(j) show an isometric view of the deformed states as well as a top-down view of the corresponding deformations. The vertical angle from the z axis is given for (g) $\psi = 15°$, (h) $\psi = 30°$, (i) $\psi = 45°$, and (j) $\psi = 60°$. The light intensity and in-plane angle are $I = 1.0$ and $\theta = 0°$ respectively.

Cylindrical Shells

We now turn to a shell with a non-axisymmetric reference configuration. In the preceding examples of axisymmetric shells, the symmetry was broken by the direction of illumination. In non-axisymmetric shells we anticipate competition between the reference shape and the illumination direction. To explore this behavior, we exam-

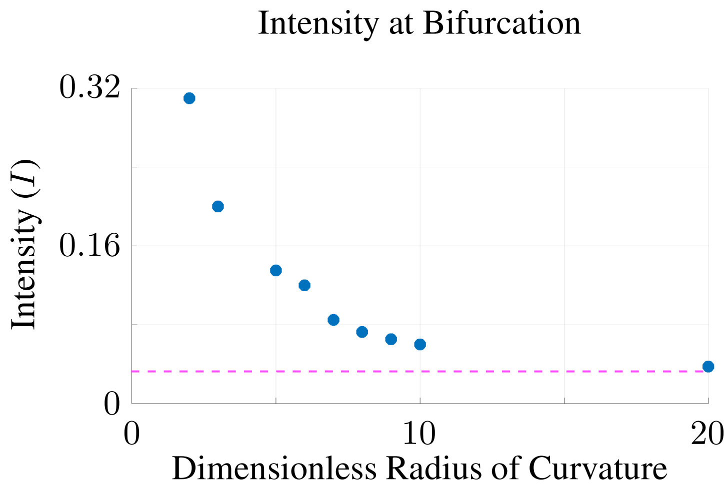

Figure 3.11: The illumination intensity at bifurcation is plotted against the dimensionless radius of curvature for various spherical caps. The dotted line represents the illumination intensity at bifurcation for a flat sheet. As the reference curvature increases (i.e., as the radius of curvature decreases), the shell becomes more rigid, requiring a greater illumination intensity to induce bifurcation.

ine cylindrical shells with radius of curvature 10.025 cm, initially aligned along the x axis. We then illuminate the structure from various directions, with the results shown in Figure 3.13.

We hold the vertical angle $\psi = 30°$, and vary the in-plane angle θ relative to the axis of the reference cylinder, with the results shown in Figures 3.13(b-e). When the illumination aligns with the axis of the reference cylinder (Figures 3.13(b)), we see an increase in curvature (the edges rise higher), and that cylinder morphs into a cone. The axis of the resulting cone is aligned with both the illumination and reference cylinder. As we change the (horizontal) angle of illumination (Figures 3.13(c,d)), the deformed shape is still conical, but the axis of the cone lies in between the axis of the reference cylinder and direction of illumination. The axis is restored when the illumination is perpendicular to cylinder axis, and the shape is that of a distorted cylinder.

3.6 Conclusions

Stimuli-responsive materials have garnered significant attention for their potential applications in soft robotics and actuators. Among this class of material, liquid crystal elastomers are noteworthy due to their ability to react to various stimuli. In this chapter, we developed a discrete shell model to explore the effects of illumination on photoactive liquid crystal elastomer shells. We use a discrete shell kinematics that

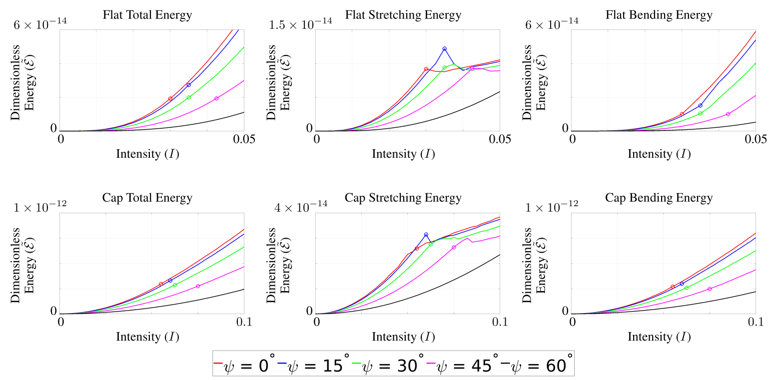

Figure 3.12: The dimensionless energy is plotted against illumination intensity for various illumination angles (see legend for orientation). The point of bifurcation is indicated with a circle at the corresponding illumination value. While the total energy monotonically increases with illumination for both the flat sheet and spherical cap, decomposing the total energy into the stretching and bending contributions reveals interesting behavior. The bending energy exhibits a kink at bifurcation and increases at a greater rate post-bifurcation. However, the stretching energy exhibits a sharp increase followed by a decline. This trend can be explained by the shell bifurcation, where the deformation minimizes the total energy by reducing the stretching energy at the cost of increasing the bending energy. Additionally, the stretching energy comprises a smaller fraction of the total energy for the spherical cap compared to the flat sheet.

enables the stretching and bending to be computed solely from nodal positions, and therefore provides computational simplicity and efficiency compared to traditional shell models that require higher order discretization.

We utilized this model to examine the deformations of various films and shells under illumination. For an axisymmetric structure with a clamped center, large bending deformations arise from illumination, causing the shell to bifurcate into a cylindrical or conical shape. Furthermore, these deformations align with the direction of light. If the clamped center is replaced with a universal joint, the shell can rotate to better align with the illumination direction; the degree of bending deformation relative to the degree of rotational motion can be tuned, allowing strong control over how elastic energy is partitioned between bending and rotation. For liquid crystalline sheets in the nematic state, director orientation can be a substitute for linearly polarized light to achieve directional bending deformations. For a non-axisymmetric structure, like a cylindrical shell, the photo-responsive behavior and reference geometry compete to influence the deformation alignment.

With these modeling capabilities, we can explore a greater scope of problems. We

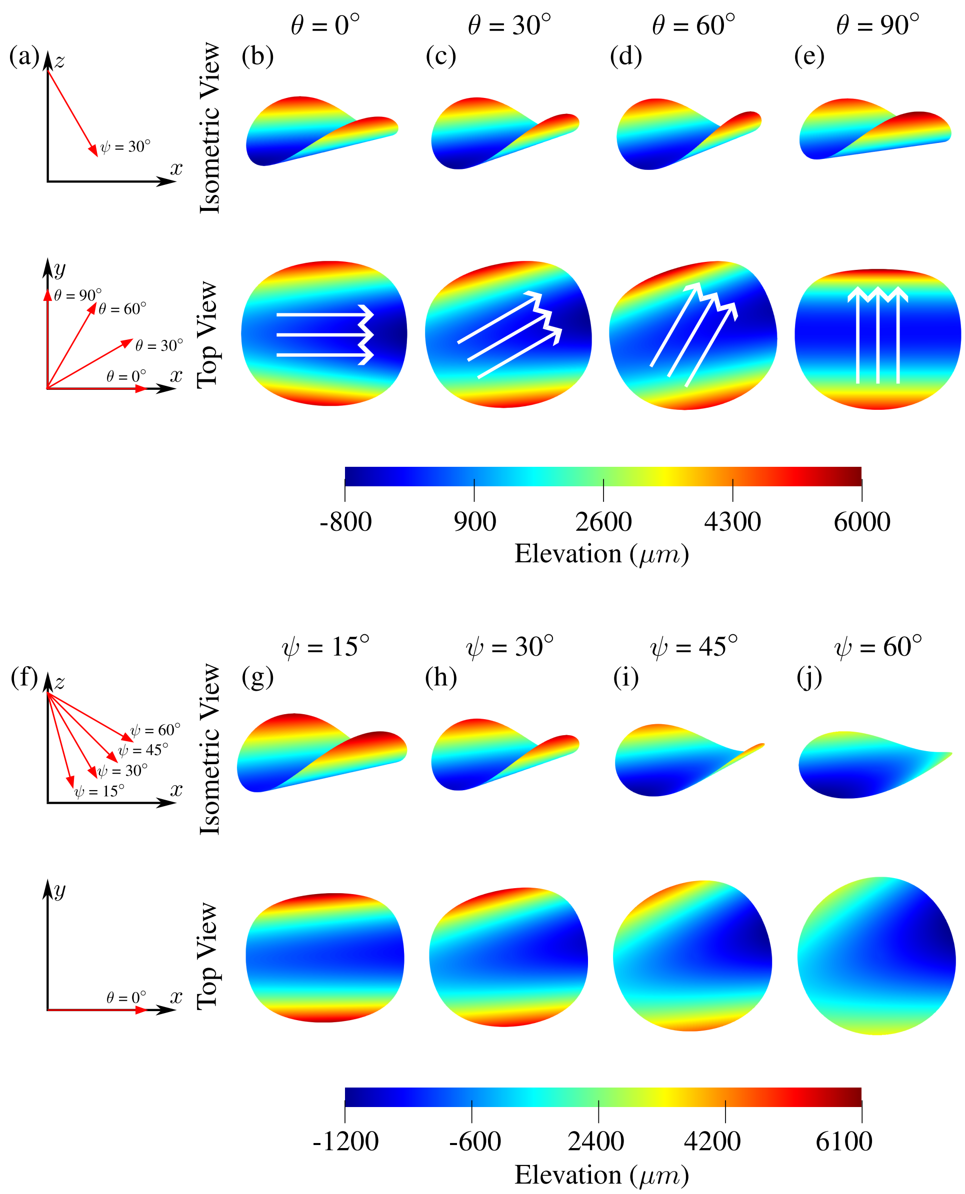

Figure 3.13: A cylindrical shell is illuminated from the (a) given orientation, corresponding to states (b)-(e). Further, (b)-(e) show an isometric view of the deformed states as well as a top-down view of the corresponding deformations. The in-plane $x - y$ component of the illumination is represented by the white arrows. The deformation aligns along the (b) 0°, (c) 30°, (d) 60°, and (e) 90° in-plane angle θ. The light intensity and vertical angle are $I = 1.0$ and $\psi = 30°$ respectively. A cylindrical shell is illuminated from the (f) given orientation, corresponding to states (g)-(j). Further, (g)-(j) show an isometric view of the deformed states as well as a top-down view of the corresponding deformations. The vertical angle from the z axis is given for (g) $\psi = 15°$, (h) $\psi = 30°$, (i) $\psi = 45°$, and (j) $\psi = 60°$. The light intensity and in-plane angle are $I = 1.0$ and $\theta = 0°$ respectively.

have already adapted this model for thermal stimulation in stimuli-responsive materials, and have observed great agreement with experimental observations. Moreover, we can apply this discrete shell model to rapidly simulate passive materials, which lends itself to being a powerful tool in optimization algorithms. This model helps capture behavior of liquid crystal elastomers, and enhancing these design capabilities can provide greater engineering freedom when designing actuators and self-aligning structures.

References

[1] Mark Warner and Eugene Michael Terentjev. *Liquid crystal elastomers*. Oxford: Oxford University Press, 2003.

[2] D Corbett and M Warner. "Nonlinear photoresponse of disordered elastomers". In: *Physical Review Letters* 96 (2006), p. 237802.

[3] Timothy J White. *Photomechanical Materials, Composites, and Systems*. Wireless Transduction of Light into Work. John Wiley & Sons, 2017.

[4] Ruobing Bai and K Bhattacharya. "Photomechanical coupling in photoactive nematic elastomers". In: *Journal of the Mechanics and Physics of Solids* 144 (Aug. 2020), p. 104115.

[5] Emre Kizilkan et al. "Influence of the porosity on the photoresponse of a liquid crystal elastomer". In: *Royal Society Open Science* (2016). DOI: `10.1098/rsos.150700`. URL: `https://royalsocietypublishing.org/doi/10.1098/rsos.150700`.

[6] M. Warner and L. Mahadevan. "Photoinduced Deformations of Beams, Plates, and Films". In: *Physical Review Letters* (2004). DOI: `0.1103/PhysRevLett.92.134302`. URL: `https://journals.aps.org/prl/pdf/10.1103/PhysRevLett.92.134302`.

[7] Yanlei Yu, Makoto Nakano, and Tomiki Ikeda. "Directed bending of a polymer film by light". In: *Nature* 425.145 (2003). DOI: `10.1038/425145a`. URL: `https://www.nature.com/articles/425145a`.

[8] Kevin Korner et al. "A nonlinear beam model of photomotile structures". In: *Proceedings of the National Academy of Sciences* 117.18 (2020), pp. 9762–9770. DOI: `10.1073/pnas.1915374117`. URL: `https://www.pnas.org/doi/abs/10.1073/pnas.1915374117`.

[9] Ameneh Maghsoodi and Kaushik Bhattacharya. "Optical penetration depth and periodic motion of a photomechanical strip". In: *Extreme Mechanics Letters* to appear (2024).

[10] Anne Helene Gelebart et al. "Making waves in a photoactive polymer film". In: *Nature* 546 (2017). DOI: `10.1038/nature22987`. URL: `https://www.nature.com/articles/nature22987`.

[11] Carl Friedrich Gauss. *Disquisitiones generales circa superficies curvas*. Dieterich, 1827.

[12] Carl D Modes, Kaushik Bhattacharya, and Mark Warner. "Disclination-mediated thermo-optical response in nematic glass sheets". In: *Physical Review E* 81 (2010), p. 060701.

[13] C D Modes, K Bhattacharya, and M Warner. "Gaussian curvature from flat elastica sheets". In: *Proceedings of the Royal Society A-Mathematical Physical And Engineering Sciences* 467 (2011), pp. 1121–1140.

[14] Taylor H. Ware et al. "Voxelated liquid crystal elastomers". In: *Science* 347.6225 (2015), pp. 982–984. DOI: 10.1126/science.1261019. URL: https://www.science.org/doi/abs/10.1126/science.1261019.

[15] Cedric P. Ambulo et al. "Four-dimensional printing of liquid crystal elastomers". In: *ACS Applied Materials & Interfaces* 9 (2017).

[16] Hillel Aharoni et al. "Universal inverse design of surfaces with thin nematic elastomer sheets". In: *Proceedings of the National Academy of Sciences* 115.28 (2018), pp. 7206–7211. DOI: 10.1073/pnas.1804702115. eprint: https://www.pnas.org/doi/pdf/10.1073/pnas.1804702115. URL: https://www.pnas.org/doi/abs/10.1073/pnas.1804702115.

[17] Daniel Corbett, Chen Xuan, and Mark Warner. "Deep optical penetration dynamics in photobending". In: *Physical Review E* 92 (2015). DOI: PhysRevE.92.013206. URL: https://journals.aps.org/pre/pdf/10.1103/PhysRevE.92.013206.

[18] Jürgen Küpfer and Heino Finkelmann. "Liquid crystal elastomers: Influence of the orientational distribution of the crosslinks on the phase behaviour and reorientation processes". In: *Macromolecular chemistry and physics* 195.4 (1994), pp. 1353–1367.

[19] Martin L Dunn. "Photomechanics of mono-and polydomain liquid crystal elastomer films". In: *Journal of applied physics* 102.1 (2007).

[20] Tayler S. Hebner et al. "Leaping liquid crystal elastomers". In: *Science Advances* 9.3 (2023), eade1320. DOI: 10.1126/sciadv.ade1320. eprint: https://www.science.org/doi/pdf/10.1126/sciadv.ade1320. URL: https://www.science.org/doi/abs/10.1126/sciadv.ade1320.

[21] Michael E McConney et al. "Topography from topology: photoinduced surface features generated in liquid crystal polymer networks". In: *Advanced Materials* 25.41 (2013), pp. 5880–5885.

[22] Anne Helene Gelebart et al. "Mastering the photothermal effect in liquid crystal networks: a general approach for self-sustained mechanical oscillators". In: *Advanced Materials* 29.18 (2017), p. 1606712.

[23] Benjamin A. Kowalski et al. "Voxel resolution in the directed self-assembly of liquid crystal polymer networks and elastomers". In: *Soft Matter* 13 (24 2017), pp. 4335–4340. DOI: 10.1039/C7SM00663B. URL: http://dx.doi.org/10.1039/C7SM00663B.

[24] J.S. Biggins, M. Warner, and K. Bhattacharya. "Elasticity of polydomain liquid crystal elastomers". In: *Journal of the Mechanics and Physics of Solids* 60.4 (2012), pp. 573–590. ISSN: 0022-5096. DOI: https://doi.org/10.1016/j.jmps.2012.01.008. URL: https://www.sciencedirect.com/science/article/pii/S0022509612000166.

[25] Junuthula Narasimha Reddy. *Theory and analysis of elastic plates and shells*. CRC press, 2006.

Chapter 4

TAPE SPRINGS

4.1 Introduction

Tape springs are thin cylindrical shells with an open cross-section, widely used as deployable booms in space structures owing to their high stiffness-to-weight ratio. Under opposite-sense bending, a localized fold forms via snap-through buckling, enabling reversible switching between a compact folded configuration and a stiff deployed state [1, 2]. This multistability, driven by geometric nonlinearity and a rich energy landscape, makes tape springs a natural test case for multi-equilibrium design: performance requirements span two geometrically distinct configurations, and the transition between them involves a snap-through event inaccessible to linear or single-equilibrium methods.

Initial theoretical analyses of the tape-spring fold trace back to Wuest [3], who treated a tape-spring under uniform longitudinal bending as an axisymmetric cylindrical shell and derived a non-monotonic moment-rotation curve. Calladine [4] obtained a simpler closed-form plateau moment $(1 + \nu)D\alpha$ by assuming a perfectly flat fold cross-section. Seffen and Pellegrino [1] synthesized these analyses, showing that this closed-form plateau agrees with a Maxwell equal-area construction on Wuest's $M(\theta)$ curve, and Seffen [2] later combined the opposite-sense and equal-sense plateau expressions into a single formula $M^* = DR\alpha[\kappa_l + \nu\kappa_t]$. Canales [5] provided a recent finite-element benchmark for the opposite-sense response on this geometry, and Mallikarachchi and Pellegrino [6] characterized composite tape-spring hinges experimentally, validating finite-element predictions against measured moment-rotation profiles.

Equal-sense bending has proven more demanding for shell finite-element approaches. Seffen and Pellegrino [1] used arc-length continuation and noted that seeding initial geometric imperfections is needed to capture bifurcation points; Hoffait et al. [7] reported that arc-length continuation failed to converge through the equal-sense flexural-torsional bifurcation and resorted to pseudo-dynamic simulation with large numerical damping. Soykasap [8] similarly relied on artificial damping for snap-through tracking in a related tape-spring hinge simulation. Reduced-order strategies have also been pursued: Canales [5] applied proper orthogonal decomposition with

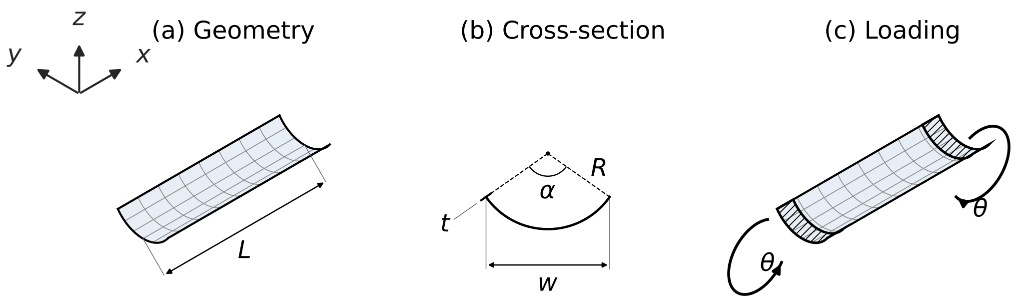

Figure 4.1: Tape-spring geometry and loading. (a) Isometric view with length L and coordinate axes. (b) Cross-section: circular arc of radius R subtending an angle α, with chord width $w = 2R\sin(\alpha/2)$ and shell thickness t. (c) Both ends clamped over a two-row band (hatched) and rotated through an equal and opposite angle θ. The sign of θ determines the loading mode: opposite-sense (against natural curvature) versus equal-sense (with natural curvature).

hyper-reduction to the opposite-sense response, and Bourgeois et al. [9] bypassed shell discretization entirely with a four-parameter rod model for planar buckling. To our knowledge, capturing the equal-sense bifurcation without imperfection seeding, artificial damping, or arc-length continuation has not been demonstrated computationally.

This chapter applies the discrete Kirchhoff-Love framework of Chapter 2 to the canonical tape-spring forward problem in both bending modes. The opposite-sense plateau matches both the inextensional-fold limit and Wuest's axisymmetric-shell prediction, and notably, the equal-sense flexural-torsional bifurcation is recovered under direct adaptive Newton-Raphson. The resulting framework supplies the equilibrium machinery on which Chapter 5 builds for inverse design.

4.2 Forward Problem: Bending Response

We first solve the forward problem to understand the bending response of an unmodified tape spring. This serves two purposes: it demonstrates that the framework captures the nonlinear snap-through physics that motivates the multi-equilibrium design problem, and it validates our approach against published tape-spring results. We first focus on opposite-sense bending: the loading mode in which the moment imposed on the tape acts to flatten the natural cross-section curvature, producing a localized fold via snap-through buckling.

The geometry and loading, shown in Figure 4.1, are parameterized by the tape length L, the cross-section radius R and subtended angle α, and the shell thickness t. To

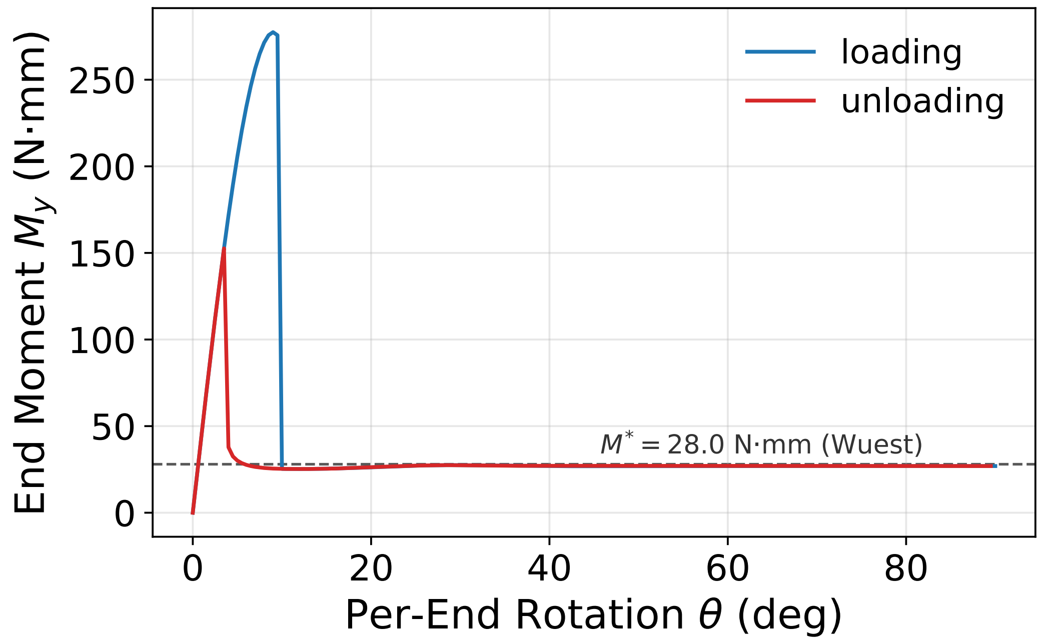

Figure 4.2: The moment-rotation response under opposite-sense bending. Loading and unloading branches are plotted in blue and red, respectively. The hysteresis loop reflects the energy dissipated in forming and recovering the localized fold. The peak moment of 277N·mm occurs pre-snap at $\theta = 9°$, and the plateau moment is ≈ 27 N·mm.

benchmark against published results, we use the values of Canales [5]: $L = 300$ mm, $R = 10$ mm, $\alpha = 110°$, $t = 0.1$ mm, $E = 131$ GPa, $\nu = 0.3$. The cross-section rise $R(1 - \cos(\alpha/2)) = 4.26$ mm sets the out-of-plane depth of the undeformed shell.

Both ends are clamped over a two-row band (the same convention as Section 2.4) and rotated through an equal and opposite angle θ at each end, as indicated in Figure 4.1(c). The relative rotation between the two clamped ends is thus 2θ. This clamped-end convention is shared with Canales [5] (direct BCs on the end cross-sections, their Table 3.1) and Seffen and Pellegrino [1] and Seffen [2] (reference-node kinematic coupling, [1] p. 1015). Those implementations fix one end longitudinally and allow only the other to slide, whereas ours allows both ends to slide symmetrically; the two setups give equivalent responses under symmetric loading. Each end is rotated by 0.5° per step (the relative rotation between ends thus grows by 1° per step), for 180 loading steps ($\theta : 0° \to 90°$ per end) followed by 180 unloading steps, with equilibrium solved at each step.

Figure 4.2 plots the moment-rotation curve $M(\theta)$ computed on a mesh with ~767k

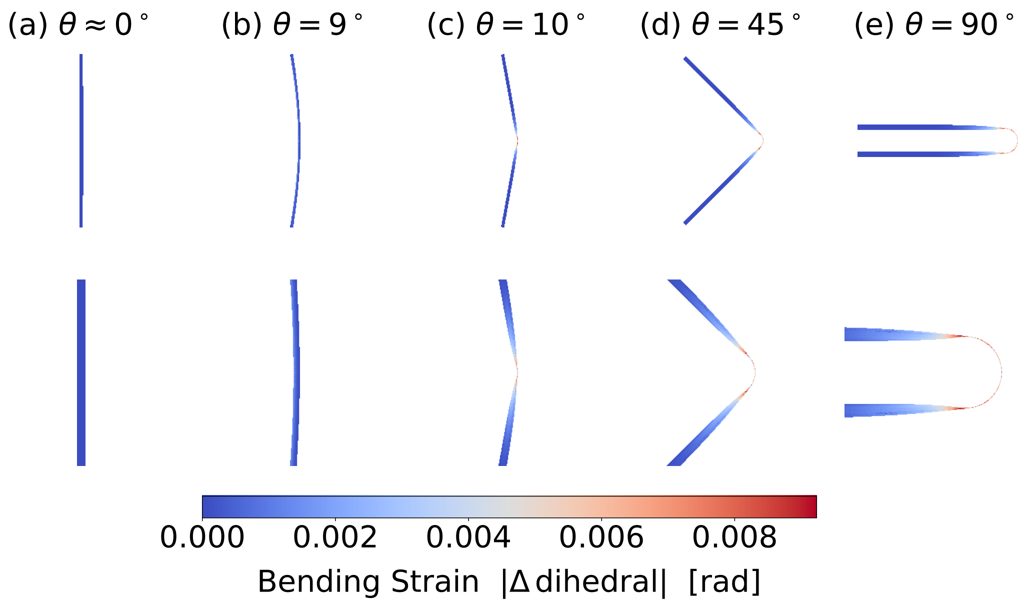

Figure 4.3: The deformed configurations are shown at five values of θ: (a) near-reference, (b) pre-snap bending ($\theta = 9°$), (c) immediately post-snap ($\theta = 10°$), (d) further folded buckled shape ($\theta = 45°$), and (e) fully folded structure ($\theta = 90°$). The top row shows the full strip side view and the bottom row zooms into the central fold region of each panel. Faces are colored by the bending strain $|\Delta\,\text{dihedral}|$, the absolute change in adjacent-face dihedral angle relative to the rest configuration.

DOFs. The response exhibits the canonical tape-spring signature [1, 4]: a near-linear elastic rise to a peak moment, a snap-through instability, a steady-state propagation plateau held across the mid-range of θ, and a hysteretic unloading branch that returns to the flat reference configuration. For our parameters, the computed peak moment is 277 N·mm at $\theta \approx 9°$, the plateau is 27 N·mm held across $10° \lesssim \theta \leq 90°$, and the hysteresis loop represents 45 mJ of energy dissipated over a complete load-unload cycle of the fold (twice the loop area in Figure 4.2, since the plot uses per-end θ), approximately 33% of the loading work. The corresponding deformation sequence (Figure 4.3) progresses from the near-reference configuration (a), through a pre-snap bending state (b), to the immediately post-snap configuration (c) , to a post-snap localized fold (d), to the fully folded configuration at $\theta = 90°$ (e). This quantitative reproduction of the canonical signature demonstrates that the framework captures the snap-through physics; the detailed comparisons against shell theory and published fold geometries follow in the next paragraphs.

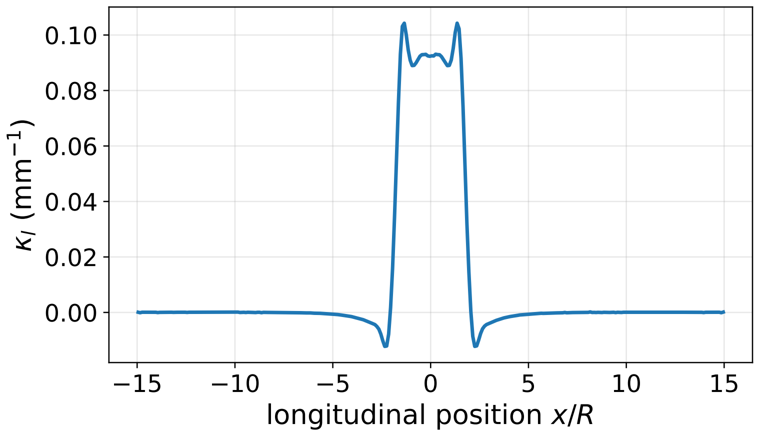

Figure 4.4: Centerline longitudinal curvature $\kappa_l(x)$ at $\theta = 90°$, normalized by the cross-section radius R, the natural in-plane length scale of the tape. The fold is localized within $|x/R| < 2.5$, with the plateau reaching $\kappa_l = 0.104$ mm^{-1}, matching the Seffen [1] prediction $\kappa_l = 1/R = 0.100$ mm^{-1} to 4.3%. Each plotted κ_l is the median over faces straddling the undeformed centerline $y = 0$ within a 1-mm bin along x.

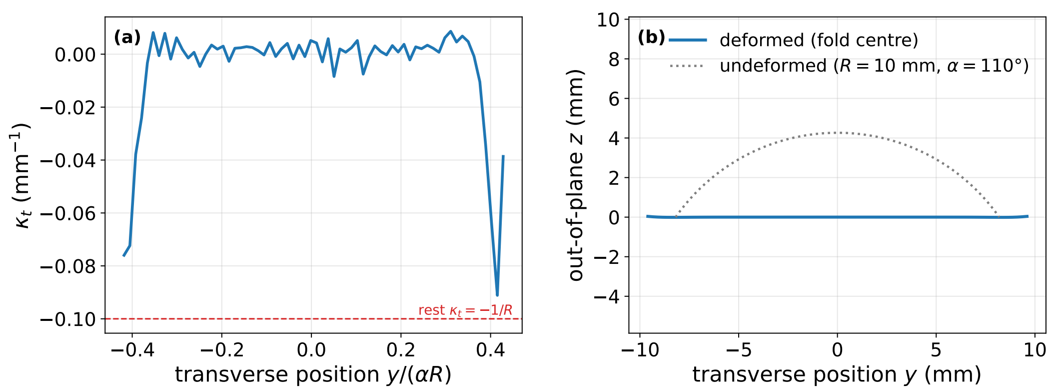

Figure 4.5: Cross-section flattening at the fold center ($x = 0$, $\theta = 90°$). (a) Transverse curvature κ_t across the width. Inside the fold ($|y/(\alpha R)| < 0.2$), $\kappa_t \approx 0$; at the cross-section edges it relaxes toward the rest value $-1/R = -0.100$ mm^{-1} (dashed). (b) Deformed cross-section (solid) compared with the undeformed arc $R = 10$ mm, $\alpha = 110°$ (dotted) along the transverse coordinate y.

Fold Geometry at Full Load

Beyond the M-θ response, classical fold theory [1, 4] predicts specific local features of the fully folded state: the longitudinal curvature κ_l should be uniform at $1/R$ inside a localized band and near zero elsewhere, and the transverse curvature κ_t should collapse from the natural rest value $-1/R$ to nearly zero within that band. Matching both would confirm that the discrete shell reproduces the correct fold mechanism, not just the correct propagation moment. Both curvatures are read directly from the discrete second fundamental form (Appendix A), the native curvature tensor of the formulation. Figure 4.4 shows that the centerline longitudinal curvature rises abruptly to $\kappa_l = 0.104\ \mathrm{mm}^{-1}$ within a band $|x/R| < 2.5$ and essentially vanishes elsewhere, matching the Seffen prediction $\kappa_l = 1/R = 0.100\ \mathrm{mm}^{-1}$ to 4.3%. Within the localized fold, the cross-section flattens almost completely. Figure 4.5(a) shows the transverse curvature κ_t along the width. The curvature is $-0.072\ \mathrm{mm}^{-1}$ at the cross-section edges (about 72% of the rest value $-1/R = -0.100\ \mathrm{mm}^{-1}$) and rises to $+0.002\ \mathrm{mm}^{-1}$ across $|y/(\alpha R)| < 0.2$ at the center, a 98% reduction. The deformed cross-section at the fold center, depicted in Figure 4.5(b), is nearly flat relative to the 4.26 mm arc rise of the undeformed section. This matches the nearly-flat cross-section reported in [1] Figure 13(b) and [5] Figure 4.8. This local fold geometry is established by the snap-through itself. At the immediate post-snap configuration ($\theta = 10°$, panel (c) of Figure 4.3), the centerline curvature already reaches $\kappa_l \approx 1/R$ at $x = 0$ within a band of $\approx 1R$ width. Continued loading from $\theta = 10°$ to $\theta = 90°$ propagates this band outward along the tape spring length to $\approx 4R$ without further sharpening the local curvature. Together, the matched propagation moment and the matched fold geometry establish that the discrete shell reproduces the correct opposite-sense fold physics: the right energetics and the right kinematics.

Moment Plateau and Peak Comparison

Table 4.1: Comparison of the discrete shell's computed moment against analytical and published-FEA references for the canonical Canales [5] geometry. The plateau (against Wuest's Maxwell construction and Calladine's $(1 + \nu)D\alpha$) and the peak moment / peak rotation (against Canales' FEA) all agree to within $\sim 5 - 10\%$.

Quantity	Reference value	Source	Computed
Plateau M^*	28.0 N·mm	Wuest [3] (Maxwell equal-area)	27 N·mm
Plateau M^*	30 N·mm	Calladine [4] $(1 + \nu)D\alpha$	27 N·mm
Peak $M_{\max}$	$\approx$ 290 N·mm	Canales [5] Fig. 3.3 (FEA)	277 N·mm
θ at peak	$\approx 10°$	Canales [5] Fig. 3.3	9°

We analyze the plateau moment using two analytical references. Table 4.1 compares our computed moments against the analytical and published-FEA references. The simpler is the Calladine [4] inextensional-fold result $M^* = (1 + \nu)D\alpha$, where $D = \frac{Et^3}{12(1-\nu^2)}$ is the bending stiffness: assuming the fold cross-section is perfectly flat ($u = 0$ in the notation of Seffen & Pellegrino [1] §3) makes the stretching energy zero, and integrating the bending moment over the flattened cross-section yields the above formula (their Eqs. 3.15-3.16). The same derivation with the opposite sign of the transverse curvature change ($\kappa_t = -1/R$ in the fold, rather than $+1/R$) yields a companion plateau formula $(1 - \nu)D\alpha$. The two are combined in Seffen [2] Eq. (1a), $M^* = DR\alpha[\kappa_l + \nu\kappa_t]$, with the sign of κ_t selecting between them. Our computed plateau sits 10% below the Calladine $(1 + \nu)D\alpha$ kinematic upper bound. A refined prediction comes from Wuest [3], who treated the tape under uniform longitudinal bending as a slightly-distorted axisymmetric cylindrical shell (Seffen & Pellegrino [1] Eqs. 3.4-3.14); the cross-section is allowed to deform and both bending and membrane contributions are retained. Wuest's $M(\theta)$ curve under uniform longitudinal bending (Seffen & Pellegrino [1] Fig. 16) is non-monotonic: it rises to a peak, drops to a trough, then rises again. The steady-state propagation moment is the horizontal line $M = M^*$ chosen such that the area of the curve above the line (pre-peak region) equals the area below it (post-trough region), known as the Maxwell (equal-area) construction (derivation in Appendix C.1). Physically, M^* is the moment at which the fold can grow or shrink along the tape at no net energy cost, so once the fold has formed the simulation settles to M^* regardless of further rotation. For our geometry the Maxwell construction yields 28.0 N·mm, in close agreement with our computed plateau of 27 N·mm (within $\sim$ 4%). Calladine's simpler closed-form $(1+\nu)D\alpha$ (30 N·mm) provides a quick kinematic upper-bound, which is consistent with our plateau, which sits about 10% below it. This match, combined with the fold geometry agreement in Figures 4.4 and 4.5, confirms that the discrete shell captures the correct physics post snap-through.

The peak moment also agrees well with the published literature. Our computed peak of 277 N·mm at $\theta = 9°$ sits within 5% of Canales [5]'s value ($\approx$ 290 N·mm at $\theta \approx 10°$) for the same geometry. Figure 4.6 shows this peak is approximately mesh-converged across four refinement levels spanning 13k to 767k DOFs. Together with the matched plateau, the framework reproduces both characteristic features of the canonical opposite-sense tape-spring signature quantitatively.

Equal-Sense Bending Response

Tape springs do not behave the same way under reversed bending. When the natural cross-sections curl against the imposed bending rather than with, the response is qualitatively different. The behavior is more unstable and imperfection sensitive, exhibiting a lower peak moment, lower propagation moment, and different fold-formation sequence. We characterize this equal-sense bending response on the same geometry as Section 4.2, both to round out the framework's treatment of the

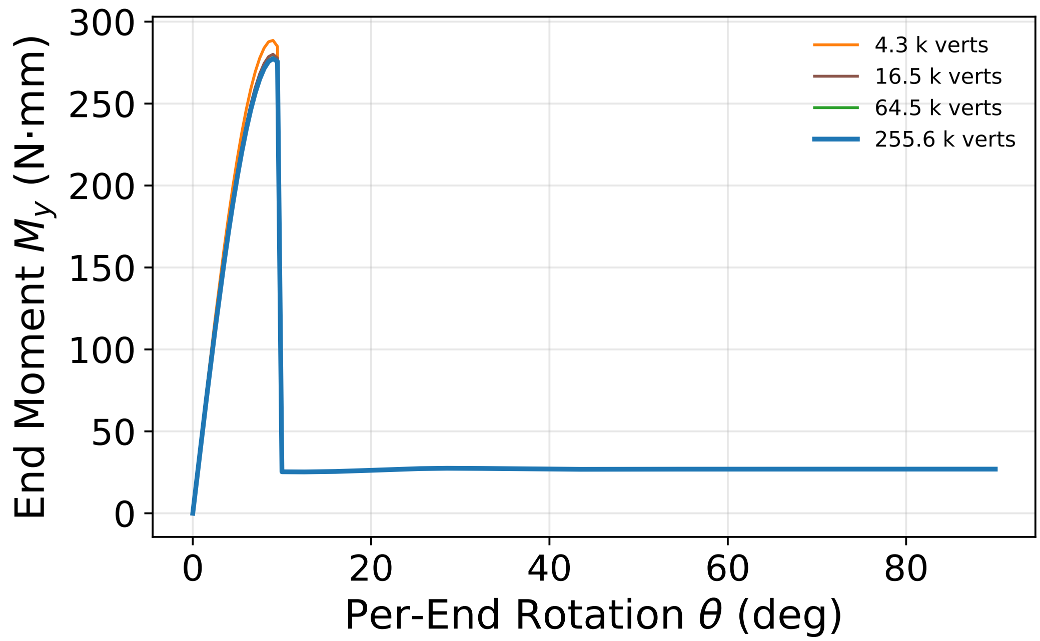

Figure 4.6: Moment-rotation loading branches for four mesh densities. Labels indicate the vertex count; DOFs scale as 3× vertices. Peaks converge monotonically to 277 N·mm across a ~ 40× refinement in element size.

canonical tape-spring loading modes and as a numerically demanding test of the discrete-shell solver.

We re-run the protocol as before with the bend direction reversed, on a 149k-vertex mesh (~447k DOFs). The step schedule is adaptive: starting at 0.125° per end (relative rotation between ends grows by 0.25° per step), the increment doubles after each three consecutive Newton-Raphson convergence successes up to a maximum of 0.5° per end (matching the opposite-sense step size), and halves on any Newton-Raphson convergence failure down to a floor of 0.002° per end. The finer initial step accommodates the sharper equal-sense bifurcation. The equilibrium equation is solved using Newton-Raphson iteration at each step with an initial guess taken to be the prior step's converged configuration. We do not seed an explicit imperfection or use arc-length continuation; the solver tracks the primary bifurcation directly under the imposed end rotations, and the discrete shell model is capable of solving for the post bifurcated equilibrium.

The equal-sense response is shown in Fig. 4.7 and differs qualitatively from opposite-sense. The initial rise to a peak of 147 N·mm at $\theta \approx 3.5°$ is the only near-linear segment of the curve; the peak transition marks a single discrete event, dropping

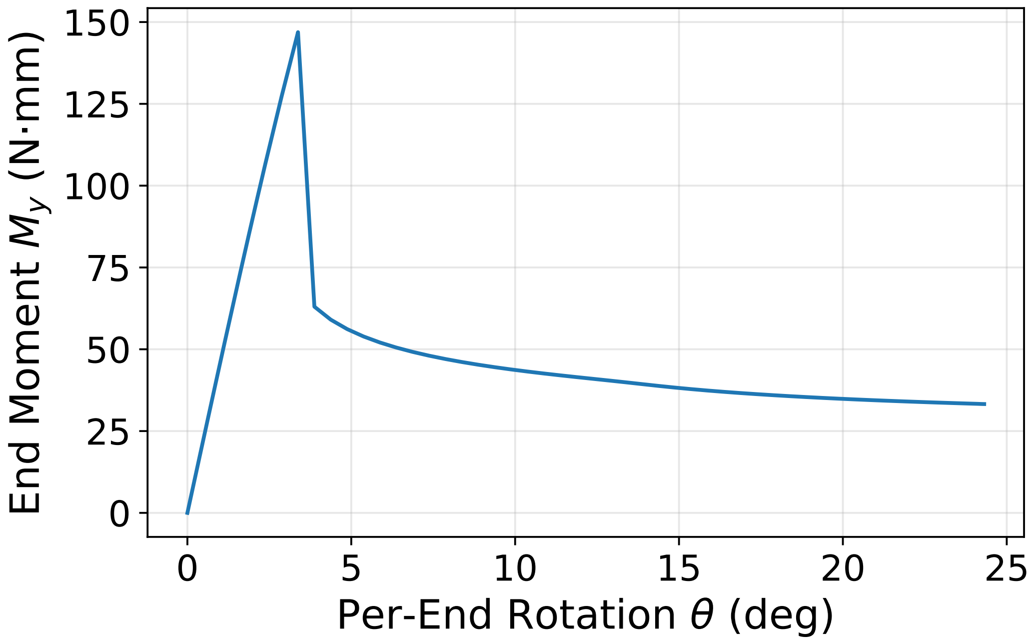

Figure 4.7: The equal-sense bending moment response is shown for a 149k-vertex mesh, plotted from $\theta = 0$ to the truncation point at $\theta \approx 24°$ per end. The moment increases until a discrete event occurs, resulting in a sharp drop at $\theta \approx 3.5°$, where the moment drops from 147 to 63 N·mm in one step. The moment continues to decrease thereafter, seemingly approaching an asymptotic limit.

the moment by 84 N·mm in one step. Past this transition the moment continues to soften smoothly through the tracked range, descending from 63 N·mm immediately post-snap to 33 N·mm at $\theta \approx 24°$, where tracking terminates. Fig. 4.8 provides a detail view of the peak transition with before/after deformation snapshots, alongside the opposite-sense response on the same axes for comparison. The peak moment is a factor of 1.9 below the opposite-sense peak (277 N·mm).

Peak Transition

The peak is identified in previous works as a flexural-torsional bifurcation marking the gradual onset of asymmetric twist-folds [1, 7, 8]. Our solver recovers a similar event: a single localized V-fold forms near the strip center in one converged step. The before/after snapshots in Fig. 4.8 show that the cross-section change across this step is subtle, in contrast to the dramatic shape change accompanying the opposite-sense snap. With further rotation the fold deepens monotonically through the remainder of the tracked range. We note that the bifurcation is recovered under direct adaptive Newton-Raphson without the seeded geometric imperfections, artificial forces and

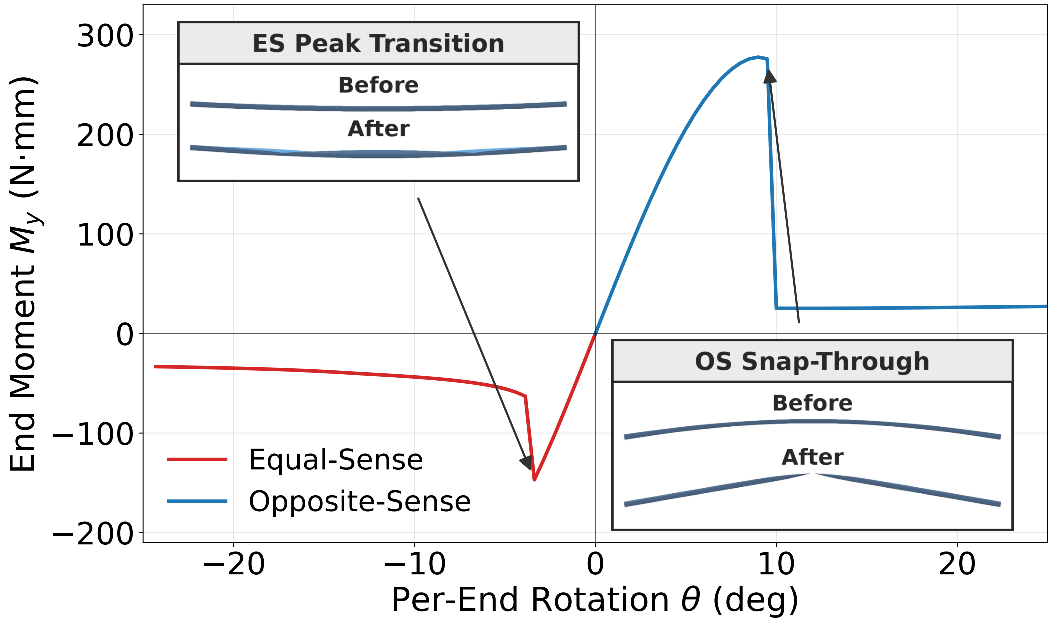

Figure 4.8: A detail view of the opposite-sense and equal-sense responses on the same structure is plotted with signed per-end θ and signed end-moment M_y. Opposite-sense (blue) occupies the positive quadrant; equal-sense (red) is mirrored into the negative quadrant. Two events are annotated with before/after snapshots of the deformed shape: the equal-sense peak transition at $\theta \approx -3.5°$ and the opposite-sense snap-through at $\theta \approx +9°$. Each before/after pair spans 1° in per-end θ.

dampening, or arc-length continuation that prior methods have required [1, 7]; the cross-section's natural curvature provides sufficient symmetry-breaking on its own and the geometric nonlinearity is resolved by this model.

4.3 Conclusion

This chapter uses the discrete shell framework of Chapter 2 to model the canonical tape-spring forward problem, in both opposite-sense and equal-sense bending. We used Newton-Raphson without imperfection seeding, arc-length continuation, or artificial damping to realize post-bifurcated states in both cases.

Under opposite-sense bending, the framework both quantitatively and qualitatively reproduces the full snap-through signature behavior from Canales' [5] benchmark geometry. The computed peak moment of 277 N·mm at $\theta = 9°$ sits within 5% of Canales' FEA values. The propagation plateau of 27 N·mm matches Wuest's [3] Maxwell-equal-area construction and sits 10% below the Calladine [4] inextensional bound. The local fold geometry matches Seffen-Pellegrino's [1] predictions: longitudinal curvature $\kappa_l = 0.104$ mm^{-1} within a fold band $|x/R| \lesssim 2.5$, transverse curvature collapsing to near zero within the same band.

Under equal-sense bending, the framework recovers a single discrete bifurcation at $\theta \approx 3.5^\circ$ with a peak moment of 147 N·mm, roughly half the opposite-sense peak. Prior finite-element treatments of this loading have required arc-length continuation, seeded geometric imperfections, or artificial damping to resolve the flexural-torsional bifurcation [1, 7, 8]. However, our framework tracks the bifurcation directly using adaptive Newton-Raphson, with the cross-section's natural curvature providing the symmetry breaking. We attribute this directly to the framework's purely positional configuration space, which is naturally suited to the strongly geometric instabilities characteristic of thin-shell snap-through: positions, fundamental forms, and energy gradients all live in a single set of coordinates, with no auxiliary parameterization for the solver to navigate. This is the chapter's principal methodological contribution.

With both bending modes validated, Chapter 5 embeds this solver as the inner loop of a multi-equilibrium topology optimization, minimizing deployed-state compliance subject to a folded-state moment constraint.

References

[1] K. A. Seffen and S. Pellegrino. "Deployment dynamics of tape springs". In: *Proceedings of the Royal Society of London. Series A: Mathematical, Physical and Engineering Sciences* 455.1983 (1999), pp. 1003–1048. DOI: 10.1098/rspa.1999.0347. URL: https://royalsocietypublishing.org/doi/10.1098/rspa.1999.0347.

[2] K. A. Seffen. "On the behavior of folded tape-springs". In: *Journal of Applied Mechanics* 68.3 (2001), pp. 369–375. DOI: 10.1115/1.1365153. URL: https://asmedigitalcollection.asme.org/appliedmechanics/article-abstract/68/3/369/462849.

[3] W. Wüst. "Einige Anwendungen der Theorie der Zylinderschale". In: *Zeitschrift für Angewandte Mathematik und Mechanik (ZAMM)* 34.12 (1954), pp. 444–454.

[4] C. R. Calladine. *Theory of Shell Structures*. Cambridge University Press, 1983.

[5] Fabricio Canales. "Numerical analysis of folding and deployment dynamics of thin shell structures with localized folds". PhD thesis. California Institute of Technology, 2023.

[6] Chinthaka Mallikarachchi and Sergio Pellegrino. “Quasi-Static Folding and Deployment of Ultrathin Composite Tape-Spring Hinges”. In: *Journal of Spacecraft and Rockets* 48 (Jan. 2011). DOI: 10.2514/1.47321.

[7] S. Hoffait et al. “Dynamic analysis of the self-locking phenomenon in tape-spring hinges”. In: *Acta Astronautica* 66 (2010), pp. 1125–1132.

[8] Ömer Soykasap. “Analysis of tape spring hinges”. In: *International Journal of Mechanical Sciences* 49 (2007), pp. 853–860.

[9] S. Bourgeois et al. “Buckling analysis of tape springs using a rod model with flexible cross-sections”. In: *European Journal of Computational Mechanics* 21.3-6 (2012), pp. 184–194.

Chapter 5

TOPOLOGY OPTIMIZATION

5.1 Introduction

Chapter 4 characterized the forward bending response of an unmodified tape spring. We now turn to the inverse problem: designing the tape-spring topology so that the resulting structure can maintain performance in both the deployed and folded configurations simultaneously. Deployed-state stiffness and folded-state moment are competing requirements: cross-sectional designs that improve the deployed stiffness tend to store more bending energy in the fold, raising the pinning moment in the folded configuration. Optimizing for either state alone yields designs that perform poorly in the other. This design challenge motivates a multi-equilibrium formulation in which the objective and constraints are evaluated across two geometrically distinct equilibrium configurations, with adjoint sensitivities computed through both. Casting the problem this way enables the optimizer to discover designs that satisfy both stable states simultaneously.

Modern density-based topology optimization originated with Bendsøe [1], who formulated structural design as a material-distribution problem with a density-based interpolation scheme that has become the standard formulation [2]. The Method of Moving Asymptotes [3] supplies the gradient-based update machinery, and density filters [4] yield well-posed designs. The framework has been extended to design problems well beyond linear compliance minimization, including compliant mechanisms [5] and nano-photonics [6], with accessible Matlab implementations [7] broadening its use. Extensions to geometrically nonlinear problems where finite deformation enters the equilibrium response have been developed [8, 9], and Bruns and Sigmund [10] extended the formulation to designing mechanisms that exhibit snap-through. Feng et al. [11] recently demonstrated DDG-based topology optimization on thin shells, restricted to the single-equilibrium setting. Akerson et al. [12] formulated optimal design of responsive structures with objectives depending on compliances at both the stimulated and unstimulated states - a multi-state formulation, though within linear elasticity and corresponding to material activation rather than distinct geometric equilibria.

However, for the deployable boom design challenge, we require: nonlinear topology optimization of a thin shell with adjoint sensitivities computed through two geometrically distinct equilibria simultaneously. Feng et al. [11] is the closest precedent in the discrete-shell setting, but evaluates performance at a single equilibrium configuration. To our knowledge, multi-equilibrium topology optimization of this type has not been developed.

This chapter formulates a multi-equilibrium topology optimization, using the discrete Kirchhoff-Love framework of Chapter 2, computing adjoint sensitivities through the deployed and folded equilibria simultaneously. The design problem minimizes deployed-state compliance subject to a bound on the folded-state reaction moment. A parameter sweep over volume fraction, design-region size, and folded-moment threshold reveals non-intuitive topologies that single-state optimizers cannot access.

5.2 Theory

Multi-Equilibrium Inverse Design using Topology Optimization

As a prototypical problem, consider the design of a deployable boom that is folded in half for storage and then deployed in the un-folded or straight configuration. We have two equilibrium states: the folded state where it is in equilibrium against a force, and the deployed state. We would like to limit or constrain the total moment that is applied in the folded state to minimize any potential damage to the structure, but maximize the stiffness (minimize the compliance) in the deployed state. We study a concrete problem in Section 5.3.

We cast the design problem as a multi-equilibrium topology optimization: find the material layout over a fixed domain that minimizes a compliance objective in one equilibrium state subject to a constraint on a quantity of interest in a second equilibrium state. The local density $\rho_e \in [0,1]$ at each element serves as the design variable. Gradient-based sensitivities are computed via the adjoint method and used to iteratively update the design.

The key feature of this formulation is that equilibrium must be evaluated in two geometrically distinct configurations. We formulate separate forward problems for the two states, each with its own boundary conditions and loading, and solve both at each design iteration. We index the states by $n \in \{1,2\}$, with equilibrium solutions $\overline{r}^{(1)}$ and $\overline{r}^{(2)}$ respectively. The objective is compliance in state 1; the constraint binds a quantity of interest evaluated at the state-2 equilibrium.

Compliance Optimization across Multiple Equilibrium Constraints

Consider a bounded region $\Omega \subset \mathbb{R}^2$ occupied by our structure, with state-dependent Dirichlet boundary $\partial_u\Omega$ and loaded boundary $\partial_f\Omega$. We introduce state-indexed tractions $f^{(n)}$, with $f^{(1)} = f$ (the applied load in state 1) and $f^{(2)} = 0$ (state 2 is loaded purely through prescribed displacements on $\partial_u\Omega$). The state-dependent energy functional is

$$\mathcal{E}^{(n)}(r,\rho) = \int_\Omega \rho(W_s + W_b)\, d\Omega - \int_{\partial_f\Omega} f^{(n)} \cdot (r - R)\, dS, \tag{5.1}$$

where $\rho \in [0,1]$ is the material density field, with $\rho = 0$ representing void and $\rho = 1$ representing solid. The equilibrium displacement field $\overline{r}^{(n)}$ in each state satisfies

$$\overline{r}^{(1)} = \underset{r-R\in\mathcal{U}_1}{\arg\min}\, \mathcal{E}^{(1)}(r,\rho), \tag{5.2}$$

$$\overline{r}^{(2)} = \underset{r-R\in\mathcal{U}_2}{\arg\min}\, \mathcal{E}^{(2)}(r,\rho), \tag{5.3}$$

where

$$\mathcal{U}_n = \left\{ u \in H^1(\Omega) \mid u \text{ satisfies the state-}n\text{ Dirichlet boundary conditions} \right\} \tag{5.4}$$

Given the state-2 equilibrium $\overline{r}^{(2)}$, the constrained quantity of interest is denoted $P(\overline{r}^{(2)},\rho)$. This could be a reaction at a clamped boundary as in the prototypical example, or any other functional of the equilibrium configuration.

Compliance is defined as

$$C(\rho) = \int_{\partial_f\Omega} f^{(1)} \cdot r^{(1)}(\rho)\, dS - \int_{\partial_f\Omega} f^{(1)} \cdot R\, dS. \tag{5.5}$$

We seek to minimize state 1 compliance subject to a bound on the state 2 quantity of interest:

$$\begin{aligned} \inf_{\rho_e\in\mathcal{D}_\rho} C(\rho) = \inf_{\rho_e\in\mathcal{D}_\rho} &\int_{\partial_f\Omega} f^{(1)} \cdot r^{(1)}\, dS \\ \text{Subject to: } \overline{r}^{(1)} &= \underset{r-R\in\mathcal{U}_1}{\arg\min}\, \mathcal{E}^{(1)}(r,\rho) \\ \overline{r}^{(2)} &= \underset{r-R\in\mathcal{U}_2}{\arg\min}\, \mathcal{E}^{(2)}(r,\rho) \\ P(\overline{r}^{(2)},\rho) &\le T \end{aligned} \tag{5.6}$$

where T is the bound on P and $\mathcal{D}_\rho$ is the admissible design space

$$\mathcal{D}_\rho = \left\{ \rho : \Omega \longrightarrow [0,1],\ \frac{1}{\|\Omega\|} \int_\Omega \rho\, d\Omega \le V_f \right\}, \tag{5.7}$$

with V_f being the maximum allowable volume fraction. The corresponding discrete formulation is

$$
\begin{aligned}
\inf_{\rho_e \in \mathcal{D}_\rho^{disc}} C(\rho) = \inf_{\rho_e \in \mathcal{D}_\rho^{disc}} \sum_{i \in \partial_f \Omega} f_i r_i(\rho) \\
\text{Subject to: } \bar{r}^{(1)} = \arg\min_{r - R \in \mathcal{U}_1} \mathcal{E}^{(1)}(r, \rho) \\
\bar{r}^{(2)} = \arg\min_{r - R \in \mathcal{U}_2} \mathcal{E}^{(2)}(r, \rho) \\
P(\bar{r}^{(2)}, \rho) \leq T
\end{aligned}
\tag{5.8}
$$

with

$$
\mathcal{D}_\rho^{disc} = \left\{ \rho_e : \Omega \longrightarrow [\rho_{min}, 1],\ \frac{1}{A_{total}} \sum_{e=1}^{E} A_e \rho_e \leq V_f \right\} \tag{5.9}
$$

Note that $A_{total} = \|\Omega\|$. For force-controlled loading, the weak form of equilibrium requires that $\bar{r}^{(n)}$ satisfies

$$
\int_\Omega \left[\frac{\partial W_s}{\partial g} : \delta g + \frac{\partial W_b}{\partial \tilde{h}} : \delta \tilde{h} \right] dA - \int_{\partial_f \Omega} f^{(n)} \cdot \delta r \, dS = 0. \tag{5.10}
$$

We solve equilibrium via Newton-Raphson, compute adjoint sensitivities for each state, update design variables via MMA, and apply a density filter to ensure regularity of the design field.

5.3 Problem Setup

We apply the multi-equilibrium topology optimization framework of Section 5.2 to tape-spring design. State 1 is the deployed configuration with tip load F applied at the free end; state 2 is the folded configuration, with no external traction and symmetric 90° rotations imposed at each end. The constrained quantity $P(\bar{r}^{(2)}, \rho)$ is the reaction moment at the clamped end of the folded state. We minimize deployed-state compliance subject to a bound on this folded-state moment.

These two quantities target the two operational requirements of a deployable boom. Deployed-state compliance measures the structure's stiffness under its operational load: a stiffer (lower-compliance) tape spring deflects less when a tip-mounted payload is applied, which is the primary mechanical function in service. Folded-state moment is the moment that a locking mechanism must continuously resist while the boom is stowed: a lower folded moment means less stored elastic energy resisting the desired folded shape, allowing a lighter locking mechanism and reducing the energy released at deployment. These requirements compete: denser cross-sections improve deployed-state stiffness but also store more bending energy in the fold, raising the folded-state moment. Optimizing either alone yields designs that perform poorly on the other, motivating the proposed multi-equilibrium formulation.

Geometry and Boundary Conditions

The tape-spring geometry follows Canales [13]: length $L = 300$ mm, thickness $t = 0.1$ mm, arc radius $R = 10$ mm, subtended angle $\alpha = 110°$, Young's modulus $E =$ 131 GPa, and Poisson's ratio $\nu = 0.3$. The reference configuration is parameterized with $x \in [-1, 1]$ along the length (non-dimensionalized by $L/2 = 150$ mm) and $y \in [-w/2, w/2]$ across the width in physical mm, where $w = 2R\sin(\alpha/2) = 16.4$ mm is the chord width. The z-coordinate of the arc cross-section is

$$z = R\cos(\alpha/2) - \sqrt{R^2 - y^2}, \tag{5.11}$$

placing the rim at $z = 0$ and the arch bottom at $z = -R\,(1 - \cos(\alpha/2)) = -4.26$ mm. The triangulated mesh consists of 16,800 vertices.

For the deployed configuration, the left edge ($x = -1$) and the immediately adjacent row of nodes are clamped, providing a two-row band clamp; a total line load $F = 0.13$ N in the $-z$ direction is distributed uniformly across the right-edge nodes ($x = 1$), chosen so the deployed-state tip deflection stays within the linear regime. For the folded configuration, both end blocks are held at a symmetric 90° rotation at each end (total relative rotation 180°). Nodes are constrained to not move in the y and z directions, and displacement in the x direction is fixed at one end, and constrained to translate as a rigid block at the other end via an augmented Lagrangian. The folded equilibrium is solved by adaptive rotation continuation from the reference flat state.

Design Problem

We choose to optimize over several different design regions, which are central slabs defined by $|x| \leq d$, with density fixed at $\rho = 1$ outside. We examine the results for four design regions with $d \in \{0.25, 0.50, 0.75, 1.00\}$. The sweep spans from a localized middle slab to the entire tape spring, so the parameter study tests how design-region size affects reachable trade-offs. A symmetry constraint is imposed on the design field about $x = 0$, ensuring the net transverse force in the folded configuration vanishes, resulting in a pure moment as the clamp reaction. We do a parameter study over different volume fractions $V_f \in \{0.60, 0.70, 0.80, 0.90\}$, applied locally to the design region, yielding a total structural volume fraction of

$V_f d + (1 - d)$. The range spans a range of mass-reduction targets, from 40% material removed at $V_f = 0.60$ down to 10% at $V_f = 0.90$, and stays clear of the void-dominant regime in which pinning equilibrium becomes unstable. The pinning metric constrained is of the form: $P(\bar{r}^{(2)}, \rho) = \frac{1}{2}\|M\|^2$, where M is the reaction moment vector at the clamped end. We choose the squared norm to have a smooth and differentiable constraint for the adjoint sensitivity. Equivalently, the bound $P \leq T$ caps the moment magnitude itself at $\|M\| \leq \|M\|_{\max} = \sqrt{2T}$, and we report this bound $\|M\|_{\max}$ in the tables and figures below. The threshold T is varied to produce designs satisfying different constraints; we span from T matching the unconstrained baseline moment (constraint inactive) down to the lowest T at which the optimizer still converges to a feasible design. Equilibrium is solved via Newton-Raphson, sensitivities are computed by the adjoint method, and design variables are updated using MMA with a density filter.

5.4 Results

We present results in five parts: (i) a detailed study of the optimal design for representative cases, (ii) moment unconstrained designs and parameter study, (iii) moment constrained designs and parameter study, (iv) compliance-moment Pareto front, and (v) heuristic analysis of the designs.

Detailed Study of the Optimal Design for Two Representative Cases

The unconstrained design for volume fraction $V_f = 0.90$ and design region $d = 1.00$ is shown in Figure 5.1(a). This design concentrates material into two continuous longitudinal ribs running along the cross-section's stiffest fibers (those farthest from the neutral axis), maximizing deployed bending stiffness without regard for folded-state behavior. The design for the same volume fraction and design region, but with the folded state moment constrained to $\|M\| \leq 3$ N·mm, is shown in Figure 5.1(b). The optimizer produces a fundamentally different topology: that same material is redistributed away from the rib structure to form two localized hourglass-shaped pockets that act as compliant hinges in the folded state, with the rest of the design region left nearly solid. This ~10% increase in compliance (C : 0.385 $\rightarrow$ 0.423 mJ) achieves a ~86% reduction in folded moment ($\|M\|$: 21.03 $\rightarrow$ 3.00 N·mm), demonstrating that the multi-state framework can drive substantial topological changes to satisfy cross-configuration constraints at small cost to the primary objective, generating designs that single-state approaches would not discover. The heuristic analysis below explores in greater detail why these two morphologies arise from the cross-section

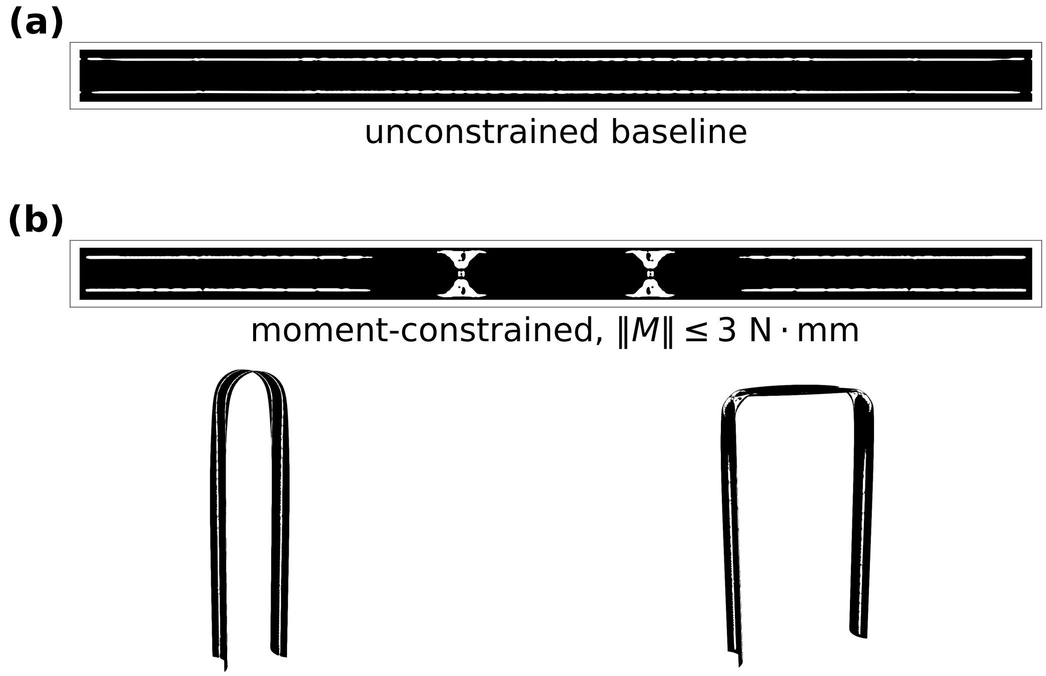

Figure 5.1: Optimized tape spring at $V_f = 0.90$, $d = 1.00$. Panel (a) shows the top view of the unconstrained design ($C = 0.385$ mJ, $\|M\| = 21.03$ N·mm), and panel (b) shows the top view of the moment-constrained design with $\|M\| \leq 3$ N·mm ($C = 0.423$ mJ, $\|M\| = 3.00$ N·mm). The bottom figures show the corresponding folded shapes: unconstrained on the left, moment-constrained on the right. Dark regions indicate high density.

Table 5.1: Moment-unconstrained design performance. Compliance C [mJ] and folded-state moment $\|M\|$ [N·mm] across the $V_f \times d$ sweep for the moment-unconstrained case (reported as C / $\|M\|$).

	$d = 0.25$	$d = 0.50$	$d = 0.75$	$d = 1.00$
$V_f = 0.90$	0.380 / 22.3	0.381 / 21.4	0.383 / 21.2	0.385 / 21.0
$V_f = 0.80$	0.383 / 18.7	0.389 / 17.4	0.395 / 16.3	0.402 / 16.2
$V_f = 0.70$	0.391 / 15.6	0.404 / 12.9	0.420 / 12.4	0.438 / 11.8
$V_f = 0.60$	0.402 / 11.6	0.430 / 9.8	0.464 / 9.4	0.501 / 9.0

geometry and the moment constraint.

Two facts from cross-section mechanics guide the interpretation. First, material contributes to the bending stiffness $I(x)$ in proportion to the square of its distance from the cross-section's neutral axis (the I-beam principle), so material near the neutral axis is structurally inefficient in the deployed state. Second, for the tape spring's arched profile the neutral axis lies between the rim and the arch bottom, so two horizontal bands across the width sit close to it.

Moment-Unconstrained Designs and Parameter Study

With no folded-state moment constraint, we optimize compliance across the 16 (volume fraction, design region) combinations. Table 5.1 reports the resulting compliance and folded-state moment for each case. The top row of Figures D.1-D.16 in Appendix D.1 shows the corresponding designs. The unconstrained designs share the same material-distribution strategy across the sweep: density drops in two longitudinal bands running the length of the design region, located at $y \approx \pm w/(2\sqrt{3})$ across the width (the neutral-axis locations of the arc cross-section, derived in Appendix D; their significance is explained in the first-principles analysis below), framed by material-rich regions at the rim and the arch bottom (the classical I-beam pattern). The degree of material reduction along these horizontal lines scales with the material removed. At $V_f = 0.90$, the density reductions are subtle and the designs appear nearly solid with many struts along the slit. However, at $V_f = 0.60$, the two lines are clearly resolved, with the voids growing larger and the number of struts decreasing, behavior which holds regardless of design region d. The consistency of this pattern indicates that, absent the moment constraint in the folded state, the optimizer is driven entirely by maximizing the cross-sectional second moment of area, independent of the available volume fraction or design-region length.

Compliance spans 0.380 mJ ($V_f = 0.90$, $d = 0.25$) to 0.501 mJ ($V_f = 0.60$, $d = 1.00$), a 32% range. The folded moment $\|M\|$ resulting from no constraint spans 9.0 to 22.3 N·mm, with the minimum at ($V_f = 0.60, d = 1.00$) and the maximum at ($V_f = 0.90, d = 0.25$). These baseline moments set the feasibility ceiling for the constrained family. Specifically, at any pair (V_f, d), a moment threshold above the unconstrained baseline value leaves the constraint inactive, a pattern visible in several cells of the galleries in Appendix D.1.

Moment-Constrained Designs and Parameter Study

Activating the folded-state moment constraint drives a qualitative departure from the previous moment-unconstrained designs. The detailed designs are shown in Figures D.1-D.16 in Appendix D.1. The resulting compliances are given in Table 5.2.

At tight moment thresholds, material is redistributed into hourglass-shaped pockets, each wide near the neutral axis and narrowing to a thin material bridge connecting the two flanges. This pattern is visible at ($V_f = 0.90, d = 1.00, \|M\| \leq 3$) in Figures 5.1 and 5.2c. The number of pockets tends to grow as the design region

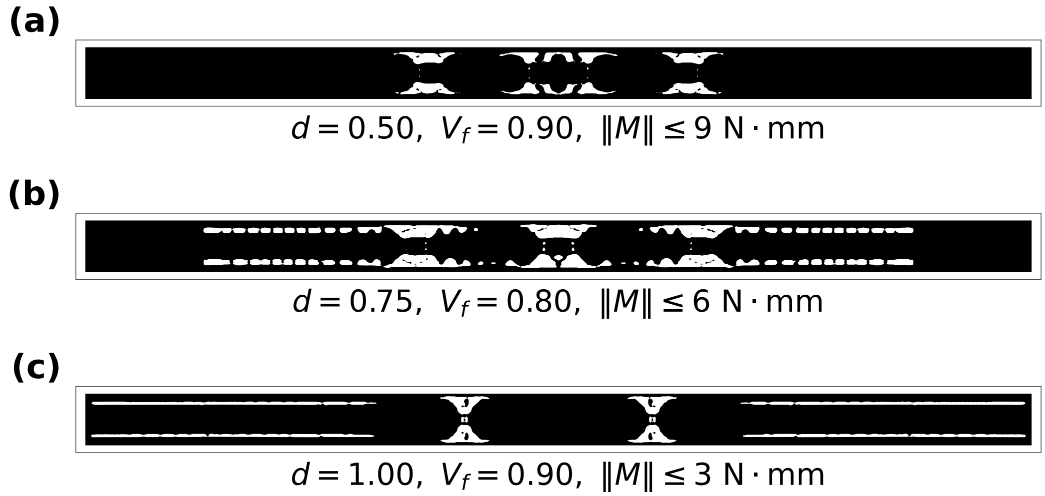

Figure 5.2: Three moment-constrained designs are shown at design-region widths $d \in \{0.50, 0.75, 1.00\}$, with V_f and $\|M\|$ also varying between panels as labeled. The number of hourglass pockets grows with d, and additional perforations appear along the flanges at $d = 1.00$.

widens, e.g., $(V_f = 0.90, d = 0.50, \|M\| \leq 9)$ and $(V_f = 0.80, d = 0.75, \|M\| \leq 6)$ in Figure 5.2a,b. This is a tendency rather than a strict rule, as the optimization is non-convex and the optimizer can land in different local minima at neighboring $(V_f, d, \|M\|)$ cells.

At the extremes of the design-region sweep, the pocket morphology is modified, as shown in Figure 5.3. At $d = 0.25$ the design region is too narrow to hold well-formed pockets: hourglass features are compressed at high V_f, e.g., $(V_f = 0.90, \|M\| \leq 9)$ (panel a), and shift to rows of elongated voids separated by thin bridges along each neutral-axis line at lower V_f, e.g., $(V_f = 0.70, \|M\| \leq 9)$ (panel b). At $d = 1.00$ the pockets persist at high V_f but are accompanied by additional perforations distributed along the length, e.g., $(V_f = 0.90, \|M\| \leq 3)$ (panel c), while at lower V_f the hourglass pocket pair gives way to two perforated flange bands above and below a central spine, with voids of irregular size and thin necks between the remaining lumps, e.g., $(V_f = 0.60, \|M\| \leq 8)$ (panel d).

The tradeoffs these topologies enable are substantial. At $(V_f = 0.90, d = 1.00)$ in Figure D.13, the tightest constraint $\|M\| \leq 3$ N·mm yields $C = 0.423$ mJ against an unconstrained baseline of 0.385 mJ, which is a 10% compliance penalty for an 86% reduction in folded moment (21.0 $\rightarrow$ 3.0 N·mm). The pattern is evident at other design regions as well. At $(V_f = 0.70, d = 0.50, \|M\| \leq 6)$, a 6%

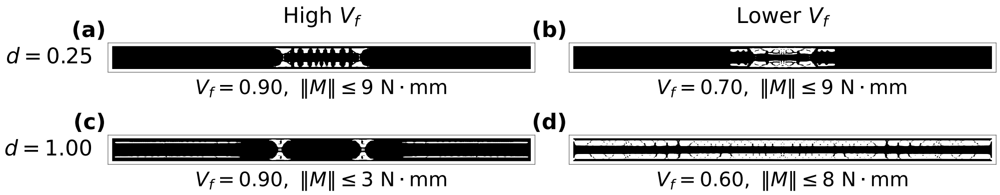

Figure 5.3: Four moment-constrained designs are shown at the corners of the design-region sweep, contrasting narrow ($d = 0.25$) and wide ($d = 1.00$) regions at high and lower V_f. The pocket morphology shifts substantially across the four corners.

compliance penalty enables a 54% moment reduction (12.9 → 6.0 N·mm), and similar ratios appear at every (V_f, d) cell where the constraint is active. A small compliance budget reliably converts into substantial moment reductions across the design space, a tradeoff that a single-state optimizer with access only to the deployed configuration has no mechanism to identify. This is the power of multi-objective topology optimization.

The sweep also exposes a stability pattern across the design-region size d. At $d = 0.25$, almost every $(V_f, \|M\|)$ cell converges and every V_f reaches the tightest threshold $\|M\| \le 3$ N·mm. The narrow design region keeps the total volume fraction $V_{f,\text{total}} = V_f\, d + (1 - d)$ high (between 0.90 and 0.975) and concentrates design freedom near the strip center, where the optimizer has the least cross-sectional moment of inertia to remove. As d widens to 0.50 and 0.75, infeasibility climbs and only a subset of cells converge, as the optimizer has more material to redistribute over a longer region and the folded-state mechanics become harder to satisfy at tight $\|M\|$. At $d = 1.00$ infeasibility drops back and most V_f again reach $\|M\| \le 3$, but at much lower $V_{f,\text{total}}$. We interpret this as the non-convex optimizer happening to find feasible minima at this extreme rather than the high-$V_{f,\text{total}}$ mechanism that stabilizes $d = 0.25$. This trend is qualitative rather than strict, given the non-convex optimization and the complex folded-state mechanics.

Compliance-Moment Pareto Front

We now study the compliance-moment Pareto front to make the insights from the previous studies concrete. Figure 5.4 plots the compliance-moment pairs $(C, \|M\|)$ across the completed cells of the sweep, with each point colored by the total volume fraction $V_{f,\text{total}} = V_f\, d + (1 - d)$ of its design. The unconstrained baselines (squares) sit at the upper edge of the cloud. From there, a trajectory down and to the right falls from each baseline, trading compliance for moment reduction. Notably, there

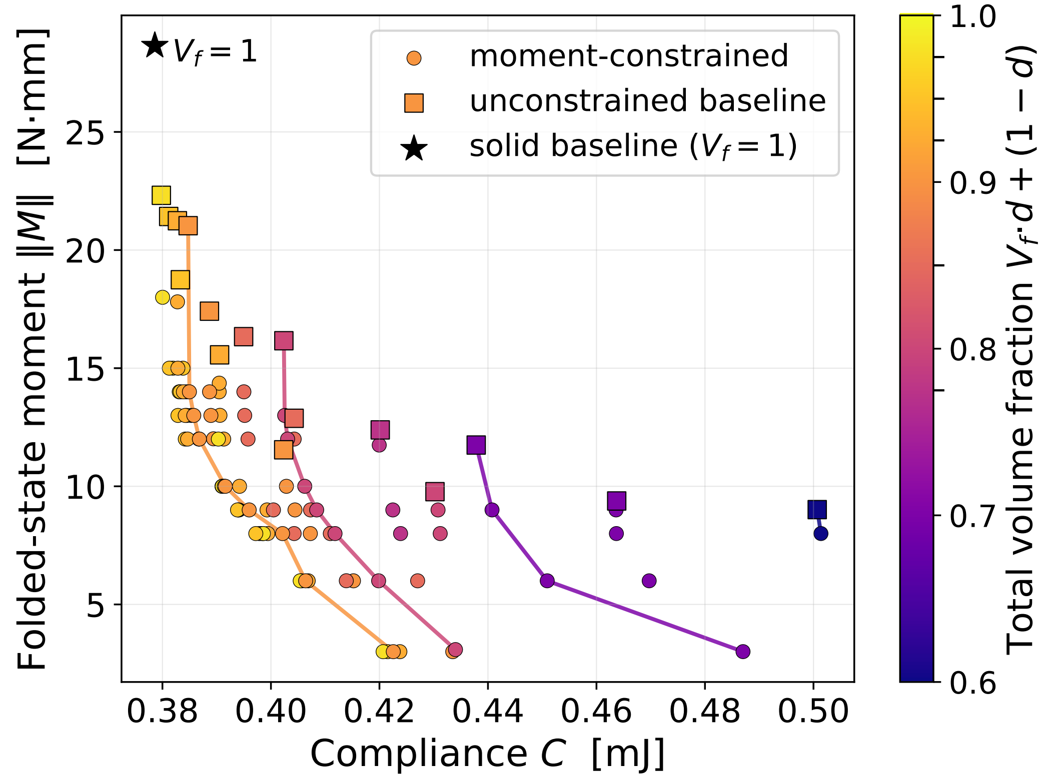

Figure 5.4: The compliance C is plotted against the folded-state moment $\|M\|$ across the TopOpt sweep over volume fraction V_f, design-region fraction d, and moment threshold $\|M\|_{\max}$. The squares correspond to unconstrained baselines (no moment constraint), and the circles correspond to moment-constrained designs. The black star at the upper-left is the solid-baseline reference ($V_f = 1$, with no material removed). The marker color encodes the total volume fraction $V_{f,\text{total}} = V_f\, d + (1 - d)$, the fraction of the entire strip occupied by material, which is distinct from the local design-region V_f used in the gallery captions. Across the sweep, $V_{f,\text{total}}$ takes 9 distinct values: $\{0.60, 0.70, 0.775, 0.80, 0.85, 0.90, 0.925, 0.95, 0.975\}$, indicated by the minor tick marks on the colorbar. The trajectory lines connect the unconstrained square to its moment-constrained children for the four $d = 1.00$ cells, where the constraint sweep covers the widest moment range; analogous trajectories for $d \in \{0.25, 0.50, 0.75\}$ are implicit through the cloud of markers. Constrained runs whose moment threshold exceeds the unconstrained baseline, where the constraint never binds, are omitted to keep the figure focused on active-constraint designs.

is more downward motion relative to the trend to the right, because the structures are able to significantly decrease the moment for a relatively small compliance penalty, as discussed previously.

The converged designs are local-minima-dependent: the topology optimization is non-convex, and neighboring thresholds can land the optimizer in topologically distinct local minima. The infeasibility cluster at intermediate d noted in the previous paragraph is one consequence. The four $d = 1.00$ trajectories drawn in Figure 5.4 most clearly illustrate the compliance-moment trade because each spans the full constraint sweep from baseline down to $\|M\| \leq 3$ N·mm.

The cloud is organized primarily by total volume fraction. Darker (lower-$V_{f,\text{total}}$) points reach lower moments at the cost of higher compliance, with the lowest moments in the sweep around $\|M\| \approx 3$ N·mm. Beyond this main trend, the Pareto exposes that material placement matters independently of material amount. For example, at $V_{f,\text{total}} = 0.90$, the $(V_f = 0.60, d = 0.25)$ unconstrained design sits at $(C, \|M\|) \approx (0.402 \text{ mJ}, 11.6 \text{ N·mm})$, whereas the $(V_f = 0.90, d = 1.00)$ unconstrained design reaches only $(0.385 \text{ mJ}, 21.0 \text{ N·mm})$ at the same total material usage.

Heuristic Analysis of the Optimized Designs

To interpret the optimized designs, we appeal to classical beam mechanics, treating the tape spring as a rough analogy to a cantilever. For a cantilever with a tip load force F, the bending moment at cross-section x is $M(x) = F(1 - x)$. Additionally, the flexure formula gives the bending stress at a fiber located a signed distance $c(y) = z(y) - z_{\text{NA}}$ from the neutral axis:

$$\sigma(x, y) = \frac{M(x)\, c(y)}{I(x)}, \tag{5.12}$$

where $I(x) = \int (z - z_{\text{NA}})^2 \, dA$ is the second moment of area. The strain energy stored in bending integrates to $U = \int M(x)^2/(2EI(x))\, dx$, so compliance satisfies $C \propto \int M(x)^2/I(x)\, dx$. To find where material placement is most effective, we differentiate with respect to the density field $\rho(x, y)$. The second moment of area at cross-section x depends on ρ through:

$$I(x) = \int_{-w/2}^{w/2} \rho(x, y)\, c(y)^2\, t\, dy, \tag{5.13}$$

so adding a unit of density at position (x, y) increases $I(x)$ by $\partial I/\partial \rho = c(y)^2 t$. Differentiating $C \propto \int M^2/I\, dx$ via the chain rule then gives:

$$\frac{\partial C}{\partial \rho(x, y)} \propto M(x)^2 \cdot \frac{\partial}{\partial \rho}\left[\frac{1}{I(x)}\right] = -\frac{M(x)^2\, c(y)^2}{I(x)^2} = -\sigma(x, y)^2. \tag{5.14}$$

This is a noteworthy result: the compliance sensitivity equals $-\sigma^2$ at each point, meaning material is most effective where the bending stress is highest. This is intuitively true from an energy standpoint as well. High stress areas store more strain energy, so reinforcing these areas results in the greatest compliance reduction per unit mass. Material is most effective at reducing compliance where σ^2 is largest, corresponding to higher moments M and higher distance from the neutral axis $|c|$.

Interestingly, these two factors are independent: $M(x)$ is determined by x-position along the length, while $c(y)$ is determined by y-position across the width through the cross-sectional geometry. Therefore, we can try to understand the given optimized topologies from this first-principles reasoning.

For the tape spring's arch cross-section, the neutral axis z_{NA} (the center of mass of the cross-section in the depth direction) lies between the arch bottom and the rim, closer to the arch bottom (see Appendix D for the derivation). As a result, the arch surface crosses the neutral axis at $y \approx \pm w/(2\sqrt{3})$. We can therefore say that $|c(y)|$ is largest near the rim ($y \approx \pm w/2$), passes through zero at $y \approx \pm w/(2\sqrt{3})$, and remains small near the arch bottom ($y = 0$). Since $\sigma^2 \propto c(y)^2$, material far from the neutral axis contributes most to I and is most effective at reducing compliance; material near the neutral axis contributes little regardless of how much is placed there. This is precisely the I-beam principle: remove material near the neutral axis (the slender center) and concentrate it far from the neutral axis (the flanges).

Unconstrained Designs With no moment constraint, the optimizer seeks to maximize $I(x)$ at every cross-section. Since $M(x) > 0$ throughout the design region, every cross-section benefits from the same strategy: concentrate material far from the neutral axis (large $|c|$, near the rim at $y \approx \pm w/2$) and remove it near the neutral axis (small $|c|$, near $y \approx \pm w/(2\sqrt{3})$). The result is a family of topologies with material removed near the neutral axis, a direct application of the I-beam principle to the tape spring cross-section.

Constrained Designs The moment constraint forces a departure from the unconstrained topology. In the unconstrained designs, the neutral-axis void spans continuously along the full length, a single void lane at $y \approx \pm w/(2\sqrt{3})$ running from one end of the design region to the other. Constrained designs concentrate these voids into discrete, hourglass-shaped pockets at specific locations. Each void pocket is wide near the neutral axis and narrows to a thin central bridge of material that connects the two flanges, maintaining structural continuity at that location. Between void pockets, the cross-section is more fully solid.

This redistribution has different consequences in the two configurations. In the folded state, the hourglass void pockets help to essentially form compliant hinges (Figure 5.1): the thin central bridge at each pocket has low local bending stiffness and can flex, reducing the structure's global resistance to folding and substantially lowering the reaction moment at the clamp. In the deployed state, the hourglass patches retain the flanged cross-section profile at their locations, resulting in a small increase in compliance, but in turn, reducing the reaction moment by a much larger factor.

5.5 Conclusion

This chapter formulated and demonstrated multi-equilibrium topology optimization of a deployable tape-spring boom, computing adjoint sensitivities through the deployed and folded equilibria simultaneously. With the discrete-shell framework of Chapter 2 as the forward solver, we minimized deployed-state compliance subject to a bound on the folded-state reaction moment, across a sweep over different design parameters: volume fraction V_f, design region d, and moment threshold $\|M\|_{\max}$.

Without a moment constraint, the optimizer reproduces a classical I-beam pattern: material is removed along longitudinal bands at the cross-section's neutral-axis locations ($y \approx \pm w/(2\sqrt{3})$). Across the sweep, unconstrained designs typically vary in the depth of these voids. Activating the moment constraint drives a qualitative departure. The dominant topologies that emerge under the constraint are discrete hourglass pockets, each acting as a compliant hinge that flexes in the folded state and modestly stiffens in the deployed state. The morphologies shift at the extremes of the design-region sweep, toward elongated voids on the neutral-axis lines at narrow d and perforated flange bands at wide d and low V_f. Across these designs, when the constraint is active, a small compliance increase reliably converts into a substantial moment reduction: at ($V_f = 0.90, d = 1.00$), a 10% compliance penalty yields an 86% moment reduction ($\|M\| : 21.0 \rightarrow 3.0$ N·mm). A first-principles compliance sensitivity ($\partial C/\partial \rho \propto -\sigma^2$) explains the neutral-axis-band placement directly from the cross-section geometry.

Designing the structure for performance across both configurations is a significant challenge: the snap-through and geometric nonlinearity make the design problem impractical for conventional approaches. A single-state optimizer with access only to the deployed configuration has no mechanism to account for the folded-state response, typically returning the longitudinal-rib topology. The multi-state framework makes this class of problems tractable: by enforcing equilibrium across both configurations and computing adjoint sensitivities for each, the optimizer can discover non-intuitive topologies, like the hourglass and strut combinations, which are superior under cross-configuration constraints. While demonstrated here on the tape spring, the approach extends to any multistable shell structure with performance requirements spanning multiple equilibrium configurations.

Designing the equilibrium endpoints leaves the deployment path between them as an open question, and the path itself is an important design consideration. The energy barrier height between the states controls the work an actuator must supply to deploy the structure. The deployment dynamics also depend on this path, including whether the structure unfolds gradually or snaps through abruptly, and whether it can lock partway through deployment or stowage. These considerations are all governed by the nonlinear energy landscape between the two equilibria. Chapter 6 characterizes this landscape with the discrete shell framework for a canonical bistable structure, a spherical cap, computing the minimum-energy paths and the saddles that set the activation barrier.

References

[1] Martin P Bendsøe. "Optimal shape design as a material distribution problem". In: *Structural optimization* 1.4 (1989), pp. 193–202.

[2] Martin Philip Bendsøe and Ole Sigmund. *Topology Optimization: Theory, Methods, and Applications*. Berlin: Springer, 2004. DOI: 10.1007/978-3-662-05086-6.

[3] Krister Svanberg. "The method of moving asymptotes — a new method for structural optimization". In: *International Journal for Numerical Methods in Engineering* 24.2 (1987), pp. 359–373. DOI: 10.1002/nme.1620240207. URL: https://onlinelibrary.wiley.com/doi/abs/10.1002/nme.1620240207.

[4] Blaise Bourdin. "Filters in topology optimization". In: *International Journal for Numerical Methods in Engineering* 50.9 (2001), pp. 2143–2158. DOI: 10.1002/nme.116. URL: https://onlinelibrary.wiley.com/doi/abs/10.1002/nme.116.

[5] Ole Sigmund. "On the design of compliant mechanisms using topology optimization". In: *Journal of Structural Mechanics* 25.4 (1997), pp. 493–524.

[6] Jakob Søndergaard Jensen and Ole Sigmund. "Topology optimization for nano-photonics". In: *Laser & Photonics Reviews* 5.2 (2011), pp. 308–321.

[7] Ole Sigmund. "A 99 line topology optimization code written in Matlab". In: *Structural and multidisciplinary optimization* 21.2 (2001), pp. 120–127.

[8] Thomas Buhl, Claus BW Pedersen, and Ole Sigmund. "Stiffness design of geometrically nonlinear structures using topology optimization". In: *Structural and Multidisciplinary Optimization* 19.2 (2000), pp. 93–104.

[9] Mathias Wallin, Niklas Ivarsson, and Daniel Tortorelli. "Stiffness optimization of non-linear elastic structures". In: *Computer Methods in Applied Mechanics and Engineering* 330 (2018), pp. 292–307. ISSN: 0045-7825. DOI: https://doi.org/10.1016/j.cma.2017.11.004. URL: https://www.sciencedirect.com/science/article/pii/S0045782517307089.

[10] TE Bruns and Ole Sigmund. "Toward the topology design of mechanisms that exhibit snap-through behavior". In: *Computer Methods in Applied Mechanics and Engineering* 193.36-38 (2004), pp. 3973–4000.

[11] Fan Feng et al. "Nonlinear topology optimization on thin shells using a reduced-order elastic shell model". In: *Thin-Walled Structures* 197 (2024), p. 111566. DOI: 10.1016/j.tws.2024.111566. URL: https://www.sciencedirect.com/science/article/abs/pii/S0263823124000119.

[12] Andrew Akerson, Blaise Bourdin, and Kaushik Bhattacharya. *Optimal Design of Responsive Structures*. 2021. DOI: 10.48550/ARXIV.2107.08895. URL: https://arxiv.org/abs/2107.08895.

[13] Fabricio Canales. "Numerical analysis of folding and deployment dynamics of thin shell structures with localized folds". PhD thesis. California Institute of Technology, 2023.

Table 5.2: Moment-constrained design performance: compliance C [mJ] across the $V_f \times d \times \|M\|$ sweep. Cells labeled *inactive* have a moment threshold above the unconstrained baseline (constraint never binds), and cells labeled *infeasible* correspond to designs where the optimizer was unable to converge.

	$d = 0.25$	$d = 0.50$	$d = 0.75$	$d = 1.00$
$\|M\| \leq 18$ N·mm				
$V_f = 0.90$	0.380	*infeasible*	0.383	*infeasible*
$V_f = 0.80$	*infeasible*	*inactive*	*inactive*	*inactive*
$V_f = 0.70$	*inactive*	*inactive*	*inactive*	*inactive*
$V_f = 0.60$	*inactive*	*inactive*	*inactive*	*inactive*
$\|M\| \leq 15$ N·mm				
$V_f = 0.90$	0.382	0.381	0.383	*infeasible*
$V_f = 0.80$	0.384	*infeasible*	*infeasible*	*infeasible*
$V_f = 0.70$	0.390	*inactive*	*inactive*	*inactive*
$V_f = 0.60$	*inactive*	*inactive*	*inactive*	*inactive*
$\|M\| \leq 12$ N·mm				
$V_f = 0.90$	0.390	0.384	0.385	0.387
$V_f = 0.80$	0.387	0.389	0.396	0.403
$V_f = 0.70$	0.391	0.404	0.420	*inactive*
$V_f = 0.60$	*inactive*	*inactive*	*inactive*	*inactive*
$\|M\| \leq 9$ N·mm				
$V_f = 0.90$	0.394	0.394	*infeasible*	0.396
$V_f = 0.80$	0.394	*infeasible*	0.400	0.408
$V_f = 0.70$	0.399	0.407	0.422	0.441
$V_f = 0.60$	0.404	0.431	0.464	*inactive*
$\|M\| \leq 8$ N·mm				
$V_f = 0.90$	0.399	0.397	*infeasible*	0.402
$V_f = 0.80$	0.398	0.398	0.404	0.412
$V_f = 0.70$	0.399	0.411	0.424	*infeasible*
$V_f = 0.60$	0.407	0.431	0.464	0.501
$\|M\| \leq 6$ N·mm				
$V_f = 0.90$	0.405	*infeasible*	*infeasible*	0.406
$V_f = 0.80$	0.406	*infeasible*	0.414	0.420
$V_f = 0.70$	0.407	0.427	*infeasible*	0.451
$V_f = 0.60$	0.415	*infeasible*	0.470	*infeasible*
$\|M\| \leq 3$ N·mm				
$V_f = 0.90$	0.421	*infeasible*	*infeasible*	0.423
$V_f = 0.80$	0.422	*infeasible*	*infeasible*	0.434
$V_f = 0.70$	0.424	*infeasible*	*infeasible*	0.487
$V_f = 0.60$	0.434	*infeasible*	*infeasible*	*infeasible*

Chapter 6

MINIMUM ENERGY PATHS

6.1 Introduction

The stable states of a multistable shell are only part of the picture. The transition paths between such configurations, and the energy barriers which separate them, also govern actuation force, deployment dynamics, and failure modes. A canonical example is the bistable spherical cap, which inverts via snap-through, similar to a popper toy. Predicting the inversion path is a numerical problem distinct from locating equilibria.

The nudged elastic band (NEB) method, introduced by Jónsson and Henkelman [1] and extended with the climbing-image variant by Henkelman et al. [2], computes minimum energy paths between two known stable states. This method constructs a chain of intermediate configurations between the two equilibria, and relaxes using a modified force constructed from the elastic energy and an artificial spring spacing term. This method was initially developed for atomic transitions in computational chemistry, but has recently been applied to bistable elastic systems. Wan et al. [3] integrated NEB in a finite-element framework to study bistable buckled beams and metamaterials. Zhou et al. [4] used NEB to identify minimum-energy folding paths in rigidly and elastically multistable origami.

For the bistable spherical cap, prior studies have focused on loaded regimes: asymmetric instabilities have been characterized under external loading [5–7], and treatments of bistability without external loading have largely been conducted under axisymmetric assumptions [8, 9]. The energy barrier of snap-through eversion in the absence of an applied indenter has not, to our knowledge, been computationally determined. Additionally, the existence of asymmetric instabilities under loading suggests that the unforced eversion path may itself break axisymmetry (for example, folding from the side), being energetically preferred over an axisymmetric path. However, no such asymmetric route has been quantified. NEB itself has not previously been applied within a discrete-shell framework.

This chapter applies the NEB method, integrated with the DDG framework of Chapter 2, to the bistable spherical cap, computing the minimum-energy path for snap-through eversion in the absence of external loading. The path passes through a non-axisymmetric saddle, a localized fold, with a barrier energy 25% below that of the axisymmetric eversion. Parameter sweeps in shell thickness and cap depth show that the barrier energy grows monotonically with both thickness and cap depth, at a rate with intermediate scaling relative to pure-stretching and pure-bending, reflecting the coupled curvature behavior governing the transition.

6.2 Theory

For deployable structures, the stable equilibrium configurations are not the only quantity of interest. The transition paths between stable states are also important to the deployment dynamics. The discrete-shell framework can be used to probe the energy landscape between two such configurations, using the nudged elastic band (NEB) method of Jónsson and Henkelman [1], applied in Section 6.3 to the eversion of a bistable spherical cap.

Consider the elastic energy as a high-dimensional landscape over the configuration space, with stable equilibria as valley floors. A continuous deformation from one stable state to the other traces a path through this landscape, and different paths cross different elevations. The easiest such route is characterized by the local gradient of the elastic energy being parallel to the path tangent. This path passes through one or more saddles - configurations at a local maximum along the path tangent, but at local minima in all perpendicular directions - and the highest such saddle defines the energy barrier between the two states. This barrier is a purely energetic quantity; the method resolves the energy landscape but not the dynamics of the transition, such as switching times.

Problem Setup

Let r denote a configuration (a complete set of nodal positions) and $\mathcal{E}(r)$ its elastic energy. The locally easiest path between two stable equilibria $\bar{r}_A$ and $\bar{r}_B$, called the minimum-energy path (MEP), is approximated by a chain of $K+1$ configurations $\{r_k\}_{k=0}^{K}$, with the endpoints $r_0 = \bar{r}_A$ and $r_K = \bar{r}_B$ fixed at the two minima and each interior image r_k for $k \in \{1, \dots, K-1\}$ a full configuration. A direct approach to finding such a chain might be minimizing $\mathcal{E}(r_k)$ independently at each interior configuration, but this would fail: with no coupling between configurations, every configuration would collapse to the endpoint minima or to an intermediate stable state, providing no resolution of the path. The NEB method overcomes this collapse by introducing an artificial spring along the path that maintains roughly uniform spacing between consecutive configurations within the configuration space. This spring, alongside the physical elastic force, drives each configuration toward the MEP. The intermediate configurations are initialized by interpolation between the endpoints, and then evolved under this modified force, whose construction is given in the next paragraph.

Force Decomposition

At each interior configuration r_k, the NEB force is constructed from two contributions. The physical elastic gradient $-\nabla\mathcal{E}(r_k)$ is projected perpendicular to the local path tangent $\hat{\tau}_k$, drawing each configuration toward the MEP without pushing it along the path:

$$F_k^{\perp} = -\nabla\mathcal{E}(r_k) + (\nabla\mathcal{E}(r_k) \cdot \hat{\tau}_k)\,\hat{\tau}_k. \tag{6.1}$$

A virtual spring of stiffness k_s connects neighboring configurations, projected along the tangent so that it controls only inter-configuration spacing along the chain:

$$F_k^{\|} = k_s\,(\|r_{k+1} - r_k\| - \|r_k - r_{k-1}\|)\,\hat{\tau}_k. \tag{6.2}$$

The path tangent $\hat{\tau}_k$ is a unit vector that approximates the path direction at r_k and is computed from the positions of the neighboring configurations, using the approach outlined in Appendix A of Zhou et al. [4]. The total NEB force is then:

$$\sigma_k = F_k^{\perp} + F_k^{\|} \tag{6.3}$$

The orthogonality of the two projections is required: the nonphysical spring (which sets inter-configuration spacing) and the physical elastic force (which pulls each configuration toward the MEP) act in transverse directions and do not compete. The force σ_k vanishes at every interior configuration precisely when the sequence of configurations lies on the MEP.

Saddle Resolution and Convergence

The chain is iterated by a descent algorithm on σ_k until $\max_k \|\sigma_k\|$ falls below a chosen tolerance, at which point the chain approximates the MEP. We use two such algorithms: the Fast Inertial Relaxation Engine (FIRE) of Bitzek et al. [10], a quasi-dynamics scheme with velocity-projected steps and adaptive time stepping, and the Quick-Min algorithm with adaptive time stepping [11], which re-projects the velocity onto the gradient direction each step. The choice in each application is given where it is used. To localize the saddle precisely along the path, we use the climbing-image variant of Henkelman et al. [2]: the highest-energy configuration has its tangential spring force removed and its tangential gradient force inverted, so

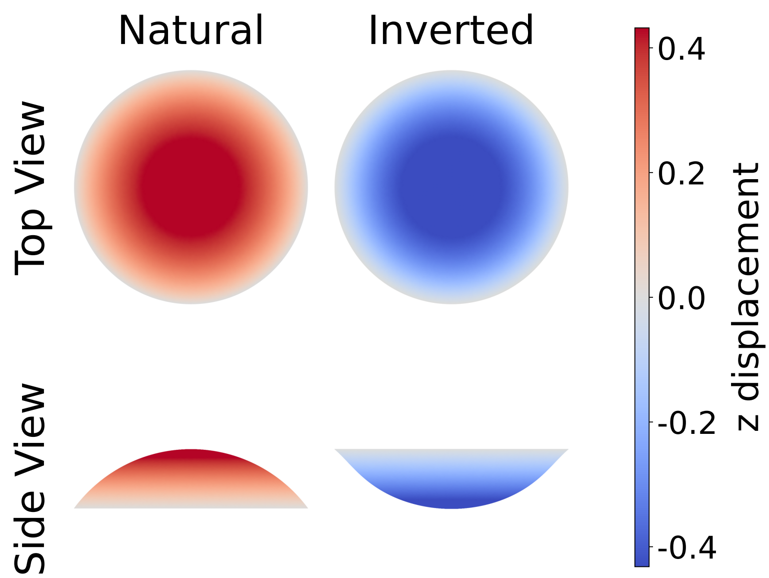

Figure 6.1: The two stable equilibrium configurations are shown for a bistable spherical cap, colored by signed z-displacement. The natural state $\bar{r}_A$ has positive z-displacement throughout (red), and the everted state $\bar{r}_B$ has negative z-displacement (blue), reflecting the curvature eversion. Canonical parameters: $R = 10$ mm, $\theta = 60°$, $t = 1$ mm, $E = 1.05$ MPa, $\nu = 0.49$.

that it climbs along the path toward the saddle while the remaining configurations continue to track the MEP.

6.3 Eversion of a Bistable Spherical Cap

We now demonstrate the use of the NEB method on a bistable spherical cap (for example, half a tennis ball), which has two stable shapes: an unstressed natural state and an everted state where the curvature has flipped. The transition between these states - snap-through eversion - involves large geometric deformations whose pathway need not preserve the axisymmetry of the equilibrium shapes.

Setup

We apply the NEB method of Section 6.2 to the bistable spherical cap. The geometry is a thin elastomeric spherical cap of curvature radius R and angular extent θ from pole to rim, with shell thickness t, clamped rim, and free interior. For the canonical case in this section, $R = 10$ mm, $\theta = 60°$, $t = 1$ mm, $E = 1.05$ MPa, $\nu = 0.49$, with the elastic constants chosen to be representative of the soft polyvinylsiloxane (PVS) elastomers used in experimental studies of bistable caps [8, 9]. The two endpoints $\bar{r}_A$ and $\bar{r}_B$ are the natural and everted equilibrium configurations.

Figure 6.1 shows these two states in top and side views. The band between them is discretized with $K+1 = 7$ configurations (five interior plus the two fixed endpoints).

Axisymmetric Saddle

The standard NEB initialization is a linear interpolation of nodal positions between the two endpoint configurations,

$$r_k(v) = (1 - s_k)\,\bar{r}_A(v) + s_k\,\bar{r}_B(v), \qquad s_k = \frac{k}{K}, \tag{6.4}$$

which preserves the rotational symmetry of the cap. The NEB algorithm relaxes from these positions, to find an axisymmetric band, with a saddle shown in Figure 6.2a (right).

Non-Axisymmetric Saddle

To probe whether a lower-barrier non-axisymmetric saddle exists, we re-run NEB from a perturbed band whose linear interpolation has been seeded with an asymmetry. The interpolation parameter s_k for configuration k is replaced by a vertex-dependent value

$$\tilde{s}_k(v) = \mathrm{clip}\left(s_k + \epsilon\left(1 - \frac{r_v}{R_{\max}}\right),\ 0,\ 1\right), \qquad r_v = \|\mathbf{x}_v - \mathbf{x}_0\|, \tag{6.5}$$

with offset $\mathbf{x}_0 = (0.5, 0)$ and bias amplitude $\epsilon = 0.25$. Vertices near $\mathbf{x}_0$ travel further along the eversion path than vertices far from it, seeding an off-axis depression in the initial band. The amplitude is small enough that the band shape is recognizable but large enough to break the cap's rotational invariance. After relaxation, this run converges to a qualitatively different saddle shown in Figure 6.2a (left). A fold appears from the left at the saddle.

Comparison of Axisymmetric and Non-Axisymmetric Barriers

The two saddles differ substantially in barrier energy (computed with Quick-Min): $E_{\max} = 2.80$ mJ for the non-axisymmetric saddle, versus 3.74 mJ for the axisymmetric one, which is a 25% reduction (Figure 6.2c). The non-axisymmetric eversion path is energetically favored over the axisymmetric one. The orientation of the non-axisymmetric dimple is set by the offset point, and the existence and energy of the lower-barrier basin are robust to the choice of minimizer; a separate NEB run with the FIRE algorithm [10] from the same perturbed initialization gives a qualitatively similar band, with $E_{\max} = 2.66$ mJ, within 5% of the 2.80 mJ above. This saddle was obtained from a single symmetry-breaking seed, however, so the energy landscape may contain other saddles and eversion paths not captured here.

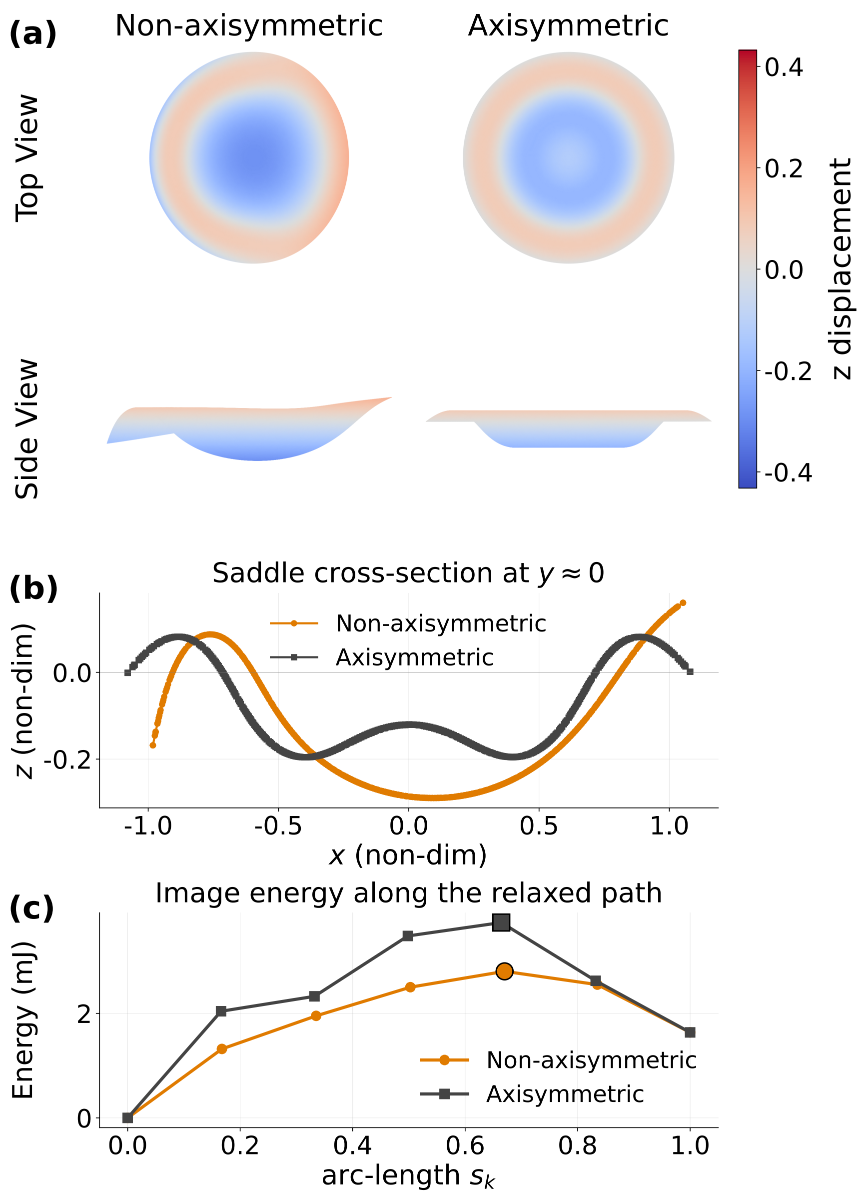

Figure 6.2: Panel (a) shows top and side views of both saddles, colored by z-displacement. Panel (b) shows cross-section profiles at $y \approx 0$. Panel (c) shows the configuration energy along each relaxed band, with the saddle marked at the highest-energy configuration. The non-axisymmetric path has 25% lower barrier energy than the axisymmetric one.

Barrier Scaling

We next examine how the non-axisymmetric saddle changes with the cap geometry and shell thickness; we compute these sweeps with the FIRE algorithm, so the canonical $t = 1$ mm, $\theta = 60^\circ$ barrier appears below as the FIRE value 2.66 mJ, within 5% of the 2.80 mJ Quick-Min value reported above. Figure 6.3 shows the

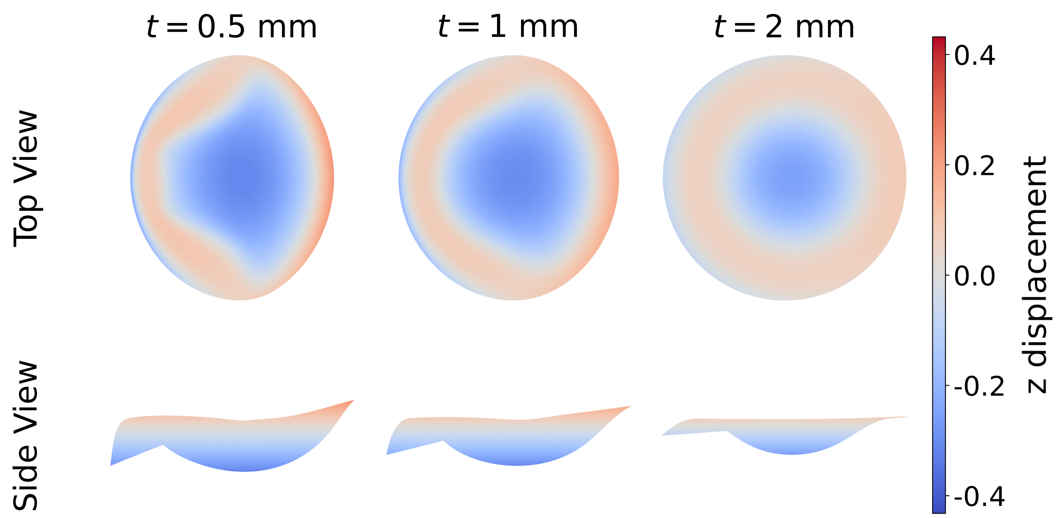

Figure 6.3: Top and side views of the non-axisymmetric saddle at three shell thicknesses t, with the cap depth $\theta = 60°$ fixed. The saddle becomes more rotationally symmetric as the shell thickens.

saddles at $t = 0.5, 1, 2$ mm with $\theta = 60°$ fixed. The barrier energy grows by roughly a factor of five to six per doubling of t, from $E_{\max} = 0.45$ mJ at $t = 0.5$ mm to 2.66 mJ at $t = 1$ mm to 13.8 mJ at $t = 2$ mm. This rate sits between the pure-bending scaling ($\propto t^3$, $\times 8$ per doubling) and pure-membrane scaling ($\propto t^1$, $\times 2$ per doubling) limits, closer to the bending-dominated end, indicating that the eversion path depends on the coupled stretching-bending behavior. The saddle shape also evolves with thickness. The thinnest cap shows the strongest off-axis asymmetry with a larger fold appearing, relative to the thicker cap, as shown in Figure 6.3. This bending-dominated scaling, together with the gradual loss of asymmetry at large t, supports the idea that breaking rotational symmetry is more beneficial in thin shells where bending is cheap relative to stretching. As the shell thickens, bending becomes relatively less energetically favorable, and the kinematic advantage of localizing the eversion into an asymmetric region diminishes.

We also vary the cap depth θ at fixed thickness $t = 1$ mm, and see a similar trend. Figure 6.4 shows the saddles at $\theta = 30°, 45°, 50°, 60°$. The barrier grows from $E_{\max} = 0.39$ mJ for the shallowest cap to 2.66 mJ for the deepest, a factor of about seven across the swept range; the saddle becomes both deeper and more pronounced as the cap deepens. The barrier energy also has implications for bistability: a shallower cap with $E_{\max} \approx 0.4$ mJ has only a small barrier holding the everted state against perturbations, while a deeper cap with $E_{\max} \approx 2.7$ mJ has a substantially

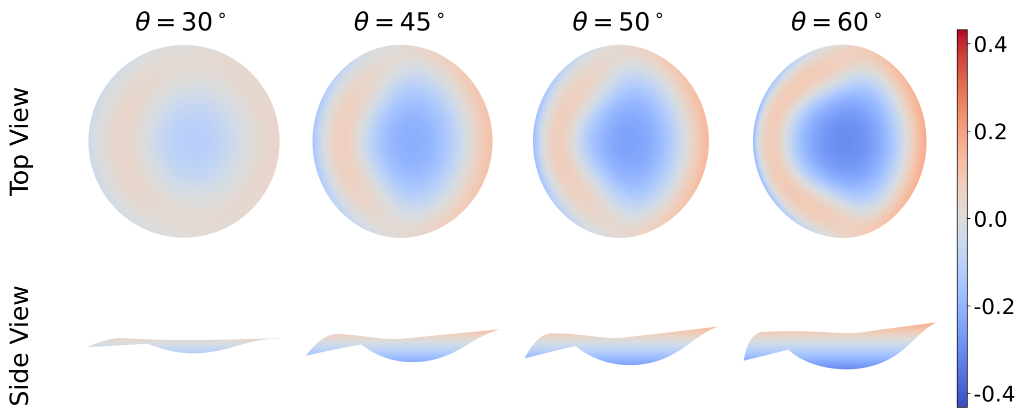

Figure 6.4: Top and side views of the non-axisymmetric saddle at four cap depths θ, with the shell thickness $t = 1$ mm fixed. The saddle becomes both deeper and more pronounced as the cap deepens.

larger barrier. We suspect this behavior occurs because cap bistability depends primarily on depth [8]: shallower caps approach the monostable limit where the everted state becomes harder to sustain.

6.4 Conclusion

This chapter applied the nudged elastic band method using the discrete-shell framework of Chapter 2 to compute the minimum-energy path for the unforced snap-through eversion of a bistable spherical cap.

We computed two candidate eversion paths: an axisymmetric path that holds the cap's rotational symmetry throughout, and a non-axisymmetric one. The non-axisymmetric path everts through a localized fold that forms on one side of the cap, and crosses a barrier 25% lower than the axisymmetric route (2.80 mJ and 3.74 mJ respectively). This asymmetric pattern follows from intuition. Consider inverting a popper toy or half tennis ball by hand: pushing from the side rather than the center is physically easier to fully invert the structure. A fold concentrates the deformation into bending along a narrow crease, mitigating the stretching resistance that a uniform axisymmetric eversion requires.

Parameter sweeps in shell thickness and cap depth show the barrier grows monotonically with both. It rises by roughly a factor of five to six per doubling of thickness, between the pure-membrane (×2) and pure-bending (×8) limits, confirming that the transition is governed by coupled stretching and bending. Consistent with the bending picture, the asymmetric fold is most pronounced in thin caps, where bending is much cheaper than stretching and localizing the eversion into a crease is energetically favorable. As the shell thickens, bending grows more costly relative to stretching, so the preferential advantage of the localized fold decreases, so the saddle becomes more axisymmetric. The barrier also grows with cap depth, which we theorize relates to bistability: shallow caps approach a monostable limit, where the everted state has a barrier too small to provide stability.

The eversion path itself has not, to our knowledge, been rigorously characterized. Prior work has examined the cap's stable states and its instabilities under external loading, and the majority of treatments do so under axisymmetric assumptions. Our results show that this assumption critically misses a lower-barrier route. The eversion path we compute breaks axisymmetry and crosses a lower barrier than the axisymmetric one. Computing this path through a discrete-shell NEB method and quantifying the barrier between the configurations is the central result of this chapter.

References

[1] Hannes Jónsson, Greg Mills, and Karsten W. Jacobsen. "Nudged elastic band method for finding minimum energy paths of transitions". In: *Classical and Quantum Dynamics in Condensed Phase Simulations*. Ed. by B. J. Berne, G. Ciccotti, and D. F. Coker. Singapore: World Scientific, 1998, pp. 385–404. DOI: 10.1142/9789812839664_0016.

[2] Graeme Henkelman, Blas P. Uberuaga, and Hannes Jónsson. "A climbing image nudged elastic band method for finding saddle points and minimum energy paths". In: *The Journal of Chemical Physics* 113.22 (2000), pp. 9901–9904. DOI: 10.1063/1.1329672. URL: https://pubs.aip.org/aip/jcp/article/113/22/9901/185050.

[3] Guangchao Wan et al. "Finding transition state and minimum energy path of bistable elastic continua through energy landscape explorations". In: *Journal of the Mechanics and Physics of Solids* 183 (2024), p. 105503. DOI: 10.1016/j.jmps.2023.105503. URL: https://www.sciencedirect.com/science/article/abs/pii/S0022509623003071.

[4] Hao Zhou et al. "Low energy fold paths in multistable origami structures". In: *International Journal of Solids and Structures* 265–266 (2023), p. 112125. DOI: 10.1016/j.ijsolstr.2023.112125. URL: https://www.sciencedirect.com/science/article/pii/S0020768323000239.

[5] L. Pauchard and S. Rica. "Contact and compression of elastic spherical shells: the physics of a 'ping-pong' ball". In: *Philosophical Magazine B* 78.2 (1998), pp. 225–233.

[6] Alice Nasto and Pedro M. Reis. "Localized Structures in Indented Shells: A Numerical Investigation". In: *Journal of Applied Mechanics* 81.12 (Oct. 2014), p. 121008. ISSN: 0021-8936. DOI: 10.1115/1.4028804. eprint: https://asmedigitalcollection.asme.org/appliedmechanics/article-pdf/81/12/121008/6080452/jam_081_12_121008.pdf. URL: https://doi.org/10.1115/1.4028804.

[7] Michael Gomez, Derek E Moulton, and Dominic Vella. "The shallow shell approach to Pogorelov's problem and the breakdown of 'mirror buckling'". In: *Proceedings of the Royal Society A: Mathematical, Physical and Engineering Sciences* 472.2187 (2016).

[8] Matteo Taffetani et al. "Static bistability of spherical caps". In: *Proceedings of the Royal Society A: Mathematical, Physical and Engineering Sciences* 474.2213 (2018).

[9] Lucia Stein-Montalvo et al. "Efficient snap-through of spherical caps by applying a localized curvature stimulus". In: *The European Physical Journal E* 45.1 (2022), p. 3.

[10] Erik Bitzek et al. "Structural Relaxation Made Simple". In: *Physical Review Letters* 97.17 (2006), p. 170201.

[11] Daniel Sheppard, Rye Terrell, and Graeme Henkelman. "Optimization methods for finding minimum energy paths". In: *The Journal of Chemical Physics* 128.13 (2008), p. 134106.

Chapter 7

CONCLUSION AND FUTURE DIRECTIONS

7.1 Conclusions

This thesis developed a discrete-shell framework that discretizes the Kirchhoff-Love shell energy on a triangular mesh, using only nodal positions as degrees of freedom. It supports the three classes of problem addressed here: forward simulation of shape change in responsive structures and deployable booms, inverse design across multiple equilibria, and characterization of the minimum-energy path between stable states.

Chapter 2 established this framework. The stretching energy is a Neo-Hookean function of the discrete first fundamental form and the bending energy is a quadratic function of the discrete second fundamental form, both assembled element-wise from nodal positions and mid-edge normals. The formulation carries no rotational degrees of freedom. The analytic gradients and tangent stiffness derived from this energy drive the equilibrium solution, adjoint sensitivities, and path-finding used in the subsequent chapters. We verified the framework on four classical shell benchmarks; it converged to established reference solutions under mesh refinement in each case.

Chapter 3 applied the framework to photoactive liquid crystal elastomer shells, where illumination induces a spontaneous curvature. Because a change in Gaussian curvature requires stretching, the shell deforms to minimize that change, producing complex shape changes. The model captured how flat sheets and curved shells deform under illumination; they bifurcate and reorient to track the light source. We reproduced experimental results and made analytical comparisons to further understand the deformation, and illustrated the competition in alignment stemming from reference curvature and illumination direction.

Chapter 4 turned to a second forward problem: the snap-through bending of bistable tape springs. The framework reproduced the opposite-sense moment-rotation behavior qualitatively and quantitatively, matching published finite-element and analytical references. Additionally, it tracked the more complex equal-sense flexural-torsional bifurcation directly under adaptive Newton-Raphson, without the imperfection seeding, arc-length continuation, or artificial damping that prior shell treatments required. In these examples, the deformation is characterized by geometric instability, demonstrating the framework's robustness to the large-deformation snap-through that governs multistable structures.

Chapter 5 built on the forward simulation of tape springs, and described the formulation and results of a multi-equilibria topology optimization problem. The inverse design challenge used the tape-spring solver, and minimized the deployed-state compliance subject to a moment constraint evaluated at the separate folded configuration, along with a mass constraint, computing adjoint sensitivities through both equilibria simultaneously. The optimizer discovered non-intuitive topologies, such as hourglass-shaped compliant hinges, that trade a small compliance penalty for a large reduction in folded-state moment, generating designs which single-state methods and conventional approaches cannot create. A first-principles beam-mechanics analysis explained the cross-sectional logic behind these topologies. The significance is that both operating states are designed at once: the deployed and folded behavior are shaped by a single optimization, rather than one being designed with no consideration for the other.

Chapter 6 characterized the transitions between stable configurations themselves, rather than treating just the equilibria. We integrated the nudged elastic band method with the framework, and computed the minimum-energy path for the unforced eversion of a bistable spherical cap. We found that the minimum-energy path breaks axisymmetry, everting through a localized fold 25% cheaper than the axisymmetric path. Parameter sweeps related the energy barrier to shell thickness and cap depth: the thickness dependence reflects the interplay between stretching and bending, while the depth dependence tracks the strength of bistability. This extended the framework beyond computing and designing equilibria to characterizing the paths between them.

The work across this thesis shows that our discrete-shell formulation, with kinematics built solely from nodal positions, is a robust computational tool for forward simulations, inverse design, and energy-landscape characterization. Multistability and geometric nonlinearity are often treated as obstacles to engineering analysis and design. This thesis instead treats them as a resource to be harnessed rather than avoided.

7.2 Future Directions

We consider several possible extensions of the topics studied in this thesis. We can extend the photoactive-shell model of Chapter 3 to dive deeper into spatially patterned director fields, or spatially non-uniform illumination, to target specific deformations. Additionally, we can extend this work to further stimuli, like thermal and electrical activation. Regarding the tape-spring forward problem of Chapter 4, we can extend the current quasi-static treatment into the dynamics regime to capture rate-dependent behavior like snap-back and deployment speed, which is relevant to the deployment behavior of full structures.

The topology optimization of Chapter 5 can be extended to incorporate manufacturing constraints, such as a minimum feature size for printability, or a minimum gap that keeps neighboring voids and struts sufficiently separate. The objective can also broaden beyond minimizing compliance under a single folded-state moment, to more accurately reflect complicated operating conditions. A deployable boom carries torsion from off-axis payloads, not only bending, so a torsional-stiffness constraint could penalize designs prone to twisting. Additionally, a slender deployed boom can buckle under compressive loads, motivating a buckling-stability constraint. One possible implementation for this constraint would be a bound on the smallest eigenvalue of the tangent stiffness at the deployed equilibrium.

There can also be extensions relevant to the folded-state configuration and the problem setup. The folded configuration could be simulated under boundary conditions used for a specific mission, rather than the ideal symmetric rotation considered in this work. Practical packaging limitations can also motivate more constraints: bounding the width of the pinched structure, for example, would penalize designs that reduce the moment by widening the folded configuration, as the hourglass hinges do in Figure 5.1. Additionally, bounding the peak folded-state stress rather than only the reaction moment could guard against material failure from repeated stowage. Finally, the formulation can be extended to more than two equilibria, to simulate structures that operate across several configurations.

A natural extension to the energy-path study of Chapter 6 is a sweep over the axisymmetry-breaking seed's location and amplitude. This would investigate how sensitive the minimum-energy path is to initialization. Furthermore, the single seed used here produces one dipole-like fold, but the landscape may contain paths with saddles of higher azimuthal symmetry, some with a lower-energy saddle than the current perturbed NEB method found. Both of the above investigations may depend on the cap thickness and depth; a more rigorous parameter sweep can investigate this dependence. The cap can also be loaded, as an actuator typically applies a prescribed pressure or contact force. This external load will assuredly affect the path, and potentially reshape it entirely from the unforced values determined in this thesis. Finally, a dynamic treatment incorporating inertia and viscoelasticity would move beyond the purely energetic barriers of the quasi-static regime to predict rate effects and switching times.

The previous extensions centered around individual chapters of this work. However, there are multiple exciting applications integrating multiple of the ideas presented.

One such idea is pairing the active-material model of Chapter 3 with the inverse-design machinery of Chapter 5. Because the framework already supports both spontaneous curvature and adjoint sensitivities, the topology-optimization loop used for passive tape springs could instead optimize the director field, illumination pattern, or material layout of a photoactive shell to actuate into a prescribed target shape. The material distribution and the active response could be co-designed at once, yielding programmable morphing structures that fold into a designed sequence of shapes under illumination. A particularly rich idea arises when considering this problem in three dimensions: the current model assumes every point sees the source, but we would need to account for self-shadowing, where one region of a deforming structure blocks the light reaching another. This would couple the illumination field and responsive behavior to the evolving geometry, and could drive sequential, self-organizing actuation.

The second combination of ideas would be topology optimization of the deployment path, rather than just the equilibrium endpoints. The topology optimization of Chapter 5 designed across the deployed and folded states, but left the path between them unconstrained; the nudged elastic band method of Chapter 6 could instead be placed inside the design loop, with the energy barrier or path shape entering the objective or constraints. This would let the optimizer design deployment kinematics directly, designing for a low activation barrier, controlled, gradual deployment, or elimination of stable intermediate states which could lock the deployment. However, the computational cost of integrating the methods 'as-is' would be prohibitive: each design iteration would require a full NEB solve within the topology optimization loop. A practical implementation would necessitate problems which can be solved on significantly coarser meshes, or use reduced-order models to simulate the forward problem. A less robust but potentially much faster alternative would track only the saddle, since it alone sets the barrier: climbing-image NEB could locate it once upon initialization, and then follow it across design iterations by warm-starting a single climbing image from the previous iterate, with robust interpolation across design updates, avoiding a full-band solve at every step. However, the central crux is the design sensitivity of the saddle energy, since the saddle is an implicitly defined stationary point. Additionally, the landscape can host multiple saddles, as found in Chapter 6, so tracking only one can miss others. Relatedly, once the density field has changed substantially over the optimization, the tracked saddle may no longer be the one that controls the barrier.

Finally, one possible area of research can integrate all three threads. A stimuli-responsive patch, potentially (but not necessarily) the photoactive material of Chapter 3, could be embedded in an otherwise passive bistable structure. The intention is that activating the patch reshapes the energy landscape itself, enabling several behaviors: lowering the barrier to trigger switching, raising it to lock a chosen state, or actuating the material between the existing states upon stimulation. Topology optimization would then determine the patch's location, size, or pattern, with an objective tied to any of these behaviors. This design problem could draw on the active-material model of Chapter 3, the inverse-design framework of Chapter 5, and the energy-landscape characterization of Chapter 6, enabling the design of shells whose multistability can be actively and selectively controlled. These directions are only a sample of what the framework makes possible; by unifying forward simulation, inverse design, and energy-landscape characterization in a single discrete-shell formulation, this work offers a powerful foundation for the broad and growing field of multistable and active shell structures.

Appendix A

APPENDIX FOR CHAPTER 2

For an element with nodes $\{a, b, c\}$ at positions $\{r^a, r^b, r^c\}$ in the current configuration and $\{R^a, R^b, R^c\}$ in the reference configuration, the discrete covariant bases are

$$E_1 = R^b - R^a, \quad E_2 = R^c - R^a, \quad e_1 = r^b - r^a, \quad e_2 = r^c - r^a. \tag{A.1}$$

The contravariant bases $\{E^\alpha\}$ satisfy $E_\alpha \cdot E^\beta = \delta_\alpha^\beta$ and are obtained from the inverse of the reference metric $A_{\alpha\beta} = E_\alpha \cdot E_\beta$. The element reference area is $A_e = \frac{1}{2}|E_1 \times E_2|$.

The first fundamental form components $a_{\alpha\beta} = e_\alpha \cdot e_\beta$ are

$$[a_{\alpha\beta}] = \begin{bmatrix} (r^b - r^a) \cdot (r^b - r^a) & (r^b - r^a) \cdot (r^c - r^a) \\ (r^c - r^a) \cdot (r^b - r^a) & (r^c - r^a) \cdot (r^c - r^a) \end{bmatrix}, \tag{A.2}$$

giving the per-element discrete stretch $g_e = \sum_{\alpha,\beta} a_{\alpha\beta}(E^\alpha \otimes E^\beta)$, the discrete analogue of the right Cauchy–Green tensor $C = F^T F$.

For curvature, edges are labeled by the opposite vertex. The mid-edge normal n^k ($k \in \{a, b, c\}$) is the unit bisector (normalized sum) of the outward face normals of the two elements sharing edge k. With $\{\xi^1, \xi^2\}$ the per-element parameterization introduced in Section 2.3 (running from node a to nodes b and c respectively), the mid-point triangle construction [1, 2] gives

$$\frac{\partial n}{\partial \xi^1} = -2(n^b - n^a), \quad \frac{\partial n}{\partial \xi^2} = -2(n^c - n^a). \tag{A.3}$$

The second fundamental form components $b_{\alpha\beta} = -e_\alpha \cdot (\partial n / \partial \xi^\beta)$ are

$$[b_{\alpha\beta}] = 2 \begin{bmatrix} (r^b - r^a) \cdot (n^b - n^a) & (r^b - r^a) \cdot (n^c - n^a) \\ (r^c - r^a) \cdot (n^b - n^a) & (r^c - r^a) \cdot (n^c - n^a) \end{bmatrix}, \tag{A.4}$$

giving the per-element discrete curvature $h_e = \sum_{\alpha,\beta} b_{\alpha\beta}(E^\alpha \otimes E^\beta)$, the discrete analogue of the (pulled-back) second fundamental form. The spontaneous curvature h_e^* is defined identically using reference-configuration normals and the reference metric; the relative-curvature tensor $\tilde{h}_e = h_e - h_e^*$ is the argument of the bending energy density W_b in the discrete energy (2.11).

References

[1] Clarisse Weischedel. "A discrete geometric view on shear-deformable shell models". PhD thesis. Universität Göttingen, 2012. URL: https://api.semanticscholar.org/CorpusID:119867289.

[2] Hsiao-Yu Chen et al. "Physical Simulation of Environmentally Induced Thin Shell Deformation". In: *ACM Transactions on Graphics* 37.4 (July 2018). ISSN: 0730-0301. DOI: 10.1145/3197517.3201395. URL: https://doi.org/10.1145/3197517.3201395.

Appendix B

APPENDIX FOR CHAPTER 3

B.1 Illumination Intensity Calculation

We aim to compute α, which is a material and geometry dependent constant which relates illumination intensity to spontaneous curvature. We take:

- Photocompliance: $c_p = 5.4 \times 10^{-5} \frac{m^2}{W}$ [1],
- Penetration Depth: $d = 0.56 \mu m$ [1],
- Thickness: $t = 30 \mu m$ (Film Dimension),

and compute the effective macroscopic coupling constant

$$\alpha = -\frac{12 c_p}{t^3} \int_{-\frac{t}{2}}^{\frac{t}{2}} exp\left(-\frac{\frac{t}{2} - z}{d}\right) z dz \tag{B.1}$$

to be

$$\alpha = 0.194 \frac{m}{W}. \tag{B.2}$$

When non-dimensionalizing (3.2), we can compute

$$\bar{I} = \frac{1}{\bar{x}\alpha} = \frac{1}{(0.01m)(0.194\frac{m}{W})} = 515 \frac{W}{m^2}, \tag{B.3}$$

where $\bar{I}$ corresponds to non-dimensional intensity $I = 1.0$ throughout the rest of this chapter.

References

[1] Kevin Korner et al. “A nonlinear beam model of photomotile structures”. In: *Proceedings of the National Academy of Sciences* 117.18 (2020), pp. 9762–9770. DOI: `10.1073/pnas.1915374117`. URL: `https://www.pnas.org/doi/abs/10.1073/pnas.1915374117`.

Appendix C

APPENDIX FOR CHAPTER 4

C.1 Wuest's Uniform-Bending Moment-Rotation Curve

The analytical plateau value $M^* = 28.0$ N·mm used in Section 4.2 comes from Wuest's [1] axisymmetric cylindrical-shell analysis, presented in detail by Seffen and Pellegrino [2] §3. We evaluate the framework at our geometry ($R = 10$ mm, $t = 0.1$ mm, $\alpha = 110°$, $E = 131$ GPa, $\nu = 0.3$).

Setup Under uniform longitudinal curvature κ_l imposed by equal and opposite end moments, the cross-section deforms from its reference natural arched shape. Let $u(s)$ denote the out-of-plane deflection of the cross-section as a function of the arc-length coordinate $s \in [-\alpha R/2, +\alpha R/2]$. The deformed transverse curvature is then the rest curvature $\frac{1}{R}$ plus the change due to deflection:

$$\kappa_t = u'' + 1/R. \tag{C.1}$$

Governing ODE $u(s)$ satisfies the fourth-order linear ODE ([2] Eqs. 3.4-3.10):

$$u'''' + K\,u = 0, \tag{C.2}$$

$$K = \frac{12(1-\nu^2)\,\kappa_l^2}{t^2}, \tag{C.3}$$

with symmetric conditions at the cross-section center ($u'(0) = u'''(0) = 0$) and zero transverse moment and shear at the free edges, which translate to $u''(\alpha R/2) = -(1/R + \nu\kappa_l)$ and $u'''(\alpha R/2) = 0$.

End Moment The end moment is obtained by integrating across the cross-section ([2] Eq. 3.13):

$$M(\kappa_l) = \int_{-\alpha R/2}^{+\alpha R/2} \big(m_{ys} - n_y\,u\big)\,ds, \tag{C.4}$$

with $m_{ys} = D[\kappa_l + \nu\kappa_t]$ the longitudinal bending moment per unit length, $n_y = -Et\kappa_l\,u$ the longitudinal membrane force per unit length, and $D = Et^3/[12(1-\nu^2)]$ the bending stiffness. Substituting m_{ys} and n_y into the integrand, we get:

$$M(\kappa_l) = \int_{-\alpha R/2}^{+\alpha R/2} \big(D[\kappa_l + \nu/R] + D\nu\,u'' + Et\kappa_l\,u^2\big)\,ds. \tag{C.5}$$

The constant term integrates to $D\alpha(\kappa_l R + \nu)$ across the arc length αR. This is the rigid contribution, which is equal to the moment if the cross-section does not deform ($u \equiv 0$). At $\kappa_l = 1/R$, this recovers Calladine's $(1+\nu)D\alpha$ [3]. The u'' term integrates to $2D\nu\, u'(\alpha R/2)$ by symmetry of $u(s)$, which is a bending correction tracking the Poisson coupling of the transverse curvature change u'' to the longitudinal direction. The u^2 term remains as a half-domain integral, $2Et\kappa_l \int_0^{\alpha R/2} u^2\, ds$, which is the membrane correction. At longitudinal curvature κ_l, an out-of-plane deflection $u(s)$ causes longitudinal stretching of the shell material with strain $\kappa_l u$ (u acts as a lever arm from the neutral axis), generating a membrane stress that contributes $Et\kappa_l u^2$ per unit area to the moment integrand. Collecting all these terms, we get

$$M(\kappa_l) = D\alpha(\kappa_l R + \nu) + 2D\nu\, u'(\alpha R/2) + 2Et\kappa_l \int_0^{\alpha R/2} u^2\, ds. \qquad \text{(C.6)}$$

Numerical Solution and Results We solve the BVP on the half-domain $s \in [0, \alpha R/2]$ using SciPy's BVP solver and sweep κ_l to evaluate $M(\kappa_l)$, which is non-monotonic; it rises to a peak, drops to a trough, and then rises again, matching the form in Seffen & Pellegrino [2] Fig. 16. The steady-state propagation moment M^* is the horizontal line such that the area above it up to the peak equals the area below it past the trough (Maxwell equal-area construction), found by a discrete search. Physically, M^* is the moment at which the fold can grow or shrink along the tape at no net energy cost: the work done crossing the peak balances the work returned past the trough. At our geometry:

- $M(\kappa_l = 1/R) = 30.0$ N·mm, within 0.2% of the Calladine inextensional bound $(1+\nu)D\alpha = 29.94$ N·mm.
- Maxwell propagation moment: $M^* = 28.0$ N·mm.

At Seffen and Pellegrino's geometry ($R = 14$ mm, $t = 0.1$ mm, $\alpha = 1.92$ rad, BeCu with $E \approx 131$ GPa), the same implementation gives $M^* = 27.97$ N·mm, within 1.2% of their Fig. 16 value $M^* = 28.3$ N·mm.

References

[1] W. Wüst. "Einige Anwendungen der Theorie der Zylinderschale". In: *Zeitschrift für Angewandte Mathematik und Mechanik (ZAMM)* 34.12 (1954), pp. 444–454.

[2] K. A. Seffen and S. Pellegrino. "Deployment dynamics of tape springs". In: *Proceedings of the Royal Society of London. Series A: Mathematical, Physical and Engineering Sciences* 455.1983 (1999), pp. 1003–1048. DOI: 10.1098/rspa.1999.0347. URL: https://royalsocietypublishing.org/doi/10.1098/rspa.1999.0347.

[3] C. R. Calladine. *Theory of Shell Structures*. Cambridge University Press, 1983.

Appendix D

APPENDIX FOR CHAPTER 5

We derive the neutral axis position and its crossing point with the arch surface for the tape spring cross-section used in Section 5.3.

Cross-Section Geometry The tape spring has a circular-arc cross-section of radius R and angular extent α (Section 5.3), with full chord width $w = 2R\sin(\alpha/2)$ spanning $y \in [-w/2, w/2]$. The z-coordinate is

$$z(y) = -\left(\sqrt{R^2 - y^2} - \sqrt{R^2 - (w/2)^2}\right), \tag{D.1}$$

so that $z(\pm w/2) = 0$ (the rim) and $z(0) = -(R - \sqrt{R^2 - (w/2)^2})$ (the arch bottom). For a shallow arch ($w/2 \ll R$), expanding to leading order gives

$$z(y) \approx -\frac{(w/2)^2 - y^2}{2R}. \tag{D.2}$$

Neutral Axis The neutral axis z_{NA} is the centroid of the cross-section in z, i.e., the z-position of its center of mass (for uniform thickness t and unit density):

$$z_{\mathrm{NA}} = \frac{\displaystyle\int_{-w/2}^{w/2} z(y)\,dy}{\displaystyle\int_{-w/2}^{w/2} dy} = \frac{1}{w}\int_{-w/2}^{w/2} z(y)\,dy. \tag{D.3}$$

Substituting the shallow-arch approximation (D.2):

$$z_{\mathrm{NA}} \approx -\frac{1}{w}\int_{-w/2}^{w/2} \frac{(w/2)^2 - y^2}{2R}\,dy = -\frac{1}{2wR}\left[(w/2)^2\,y - \frac{y^3}{3}\right]_{-w/2}^{w/2} = -\frac{1}{2wR}\cdot\frac{w^3}{6} = -\frac{w^2}{12R}. \tag{D.4}$$

Since $|z_{\mathrm{NA}}| = w^2/(12R) < w^2/(8R) = |z(0)|$, the neutral axis lies between the rim ($z = 0$) and the arch bottom ($z \approx -w^2/(8R)$), closer to the arch bottom.

Neutral Axis Crossing The fiber distance from the neutral axis is $c(y) = z(y) - z_{\mathrm{NA}}$. Setting $c(y) = 0$ gives the y-positions where the arch surface crosses the neutral axis:

$$z(y) = z_{\mathrm{NA}} \implies -\frac{(w/2)^2 - y^2}{2R} = -\frac{w^2}{12R} \implies (w/2)^2 - y^2 = \frac{w^2}{6} \implies y^2 = \frac{w^2}{12}, \tag{D.5}$$

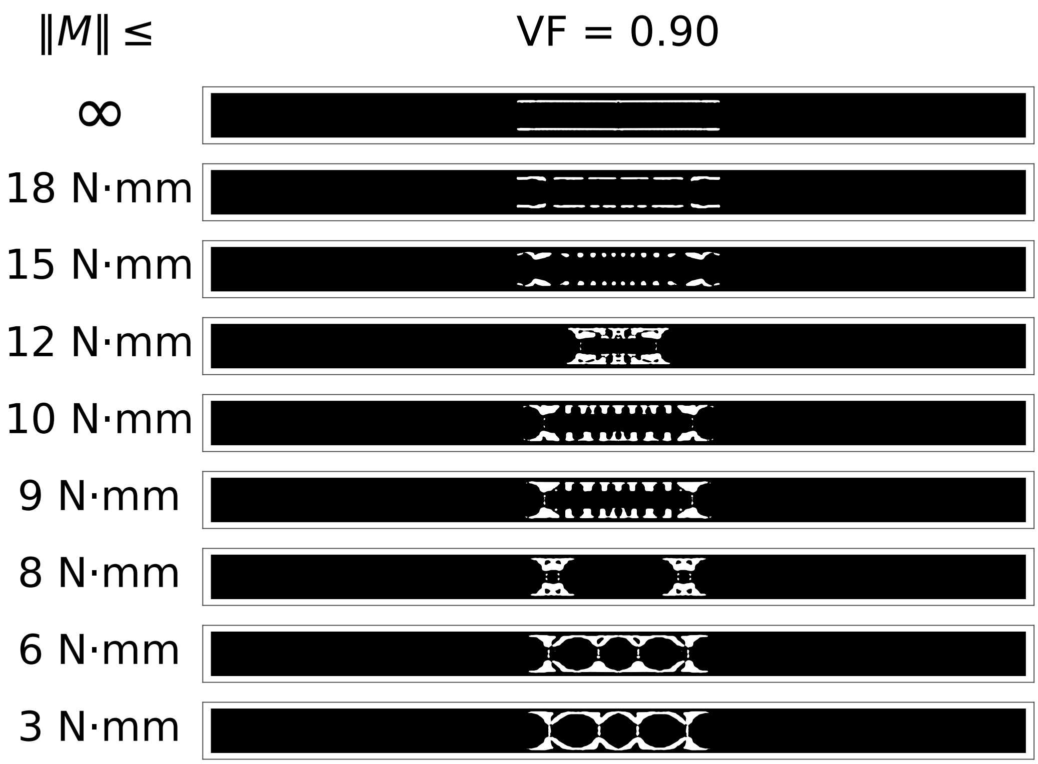

Figure D.1: Optimized designs for design-region fraction $d = 0.25$ at volume fraction $V_f = 0.90$. Each row corresponds to a moment threshold $\|M\|_{\max}$ as labeled, with the unconstrained baseline (∞) at the top and tightening downward. Black denotes material and white denotes void. Non-design regions ($|x| > d$) are solid by construction. Gap cells labeled *constraint inactive* mark thresholds already satisfied by the unconstrained design (the moment constraint is above the resultant moment from the unconstrained, single-state optimizer). *infeasible* corresponds to designs where the optimizer was unable to converge.

so

$$y = \pm\frac{w}{2\sqrt{3}} \approx \pm 0.289\, w. \tag{D.6}$$

For $|y| > w/(2\sqrt{3})$ (toward the rim), $c(y) > 0$ and increases toward $c(\pm w/2) = w^2/(12R)$. For $|y| < w/(2\sqrt{3})$ (toward the arch bottom), $c(y) < 0$ and remains small, with $c(0) = -w^2/(24R)$. The rim therefore sits farthest from the neutral axis, making it the most efficient location for material placement in bending.

D.1 Optimized Tape Design

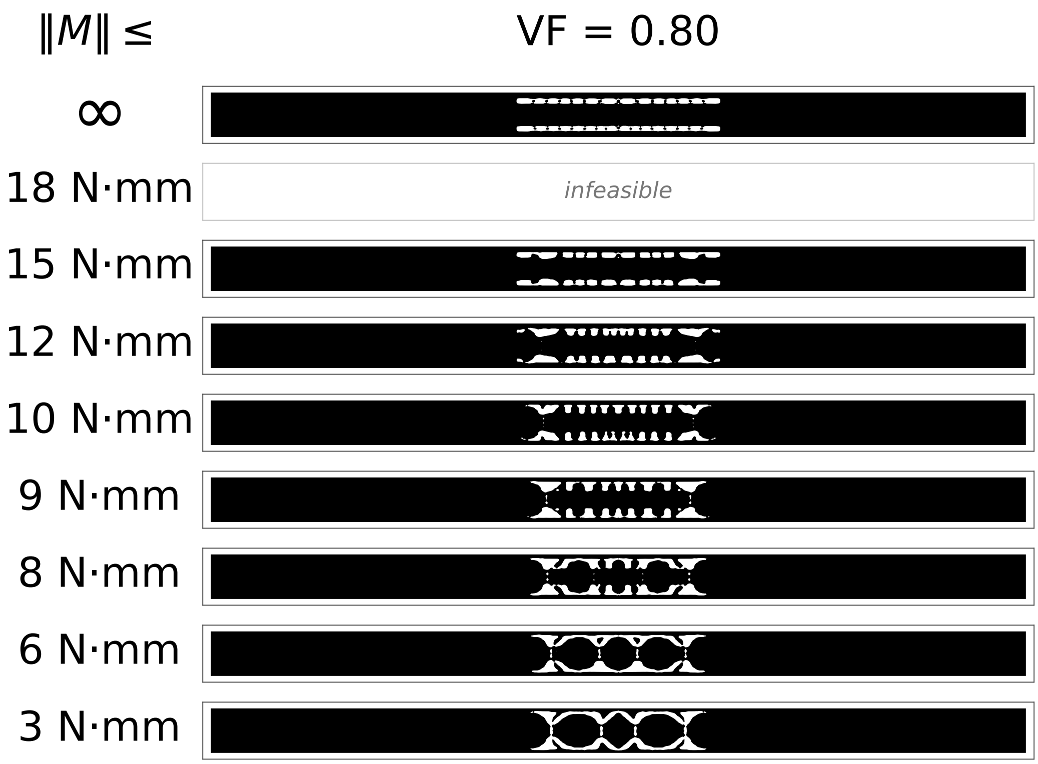

Figure D.2: Optimized designs for $d = 0.25$ at $V_f = 0.80$. The same grid and rendering conventions apply as in Figure D.1.

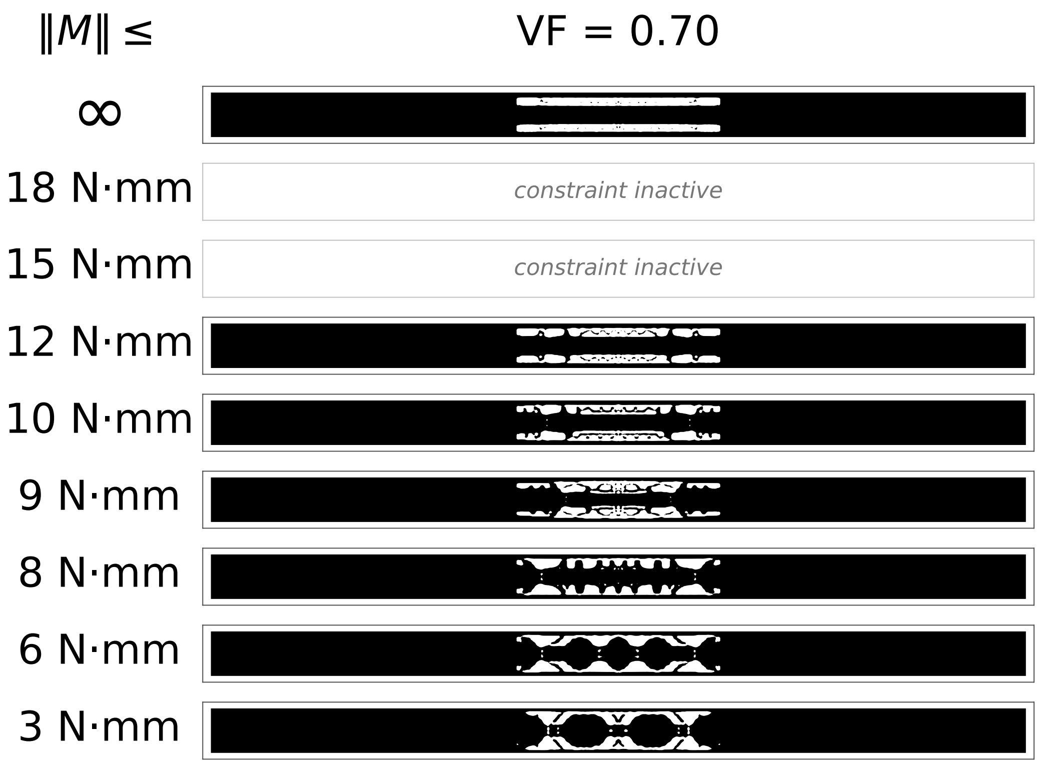

Figure D.3: Optimized designs for $d = 0.25$ at $V_f = 0.70$. The same grid and rendering conventions apply as in Figure D.1.

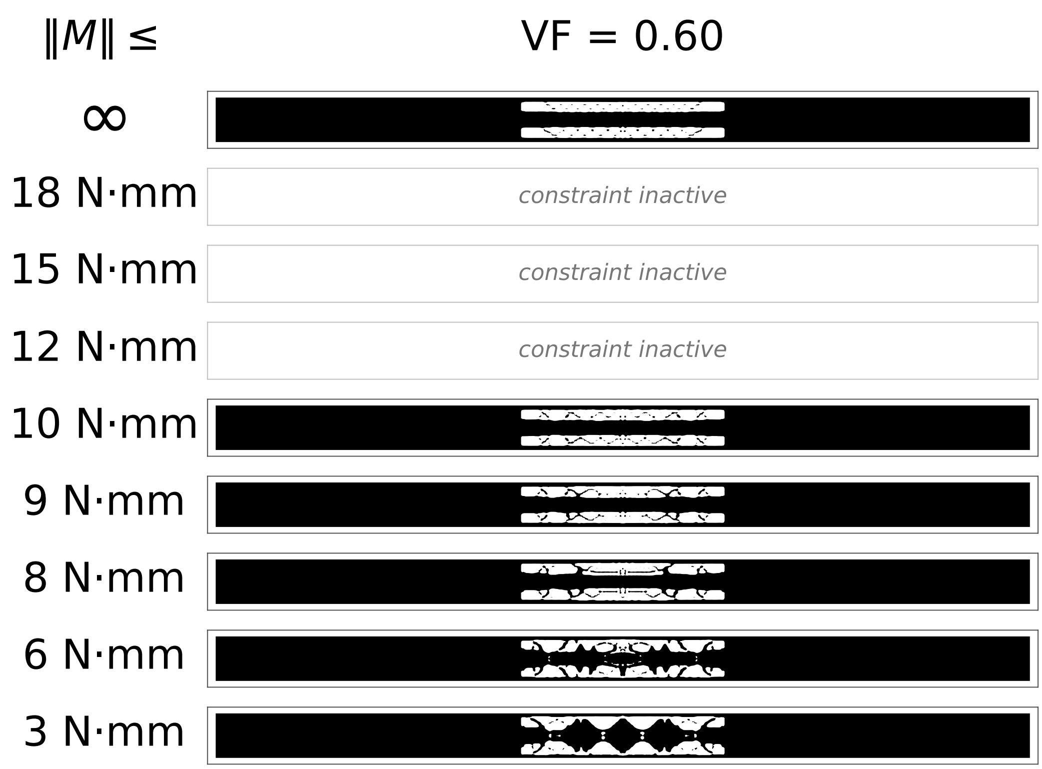

Figure D.4: Optimized designs for $d = 0.25$ at $V_f = 0.60$. The same grid and rendering conventions apply as in Figure D.1.

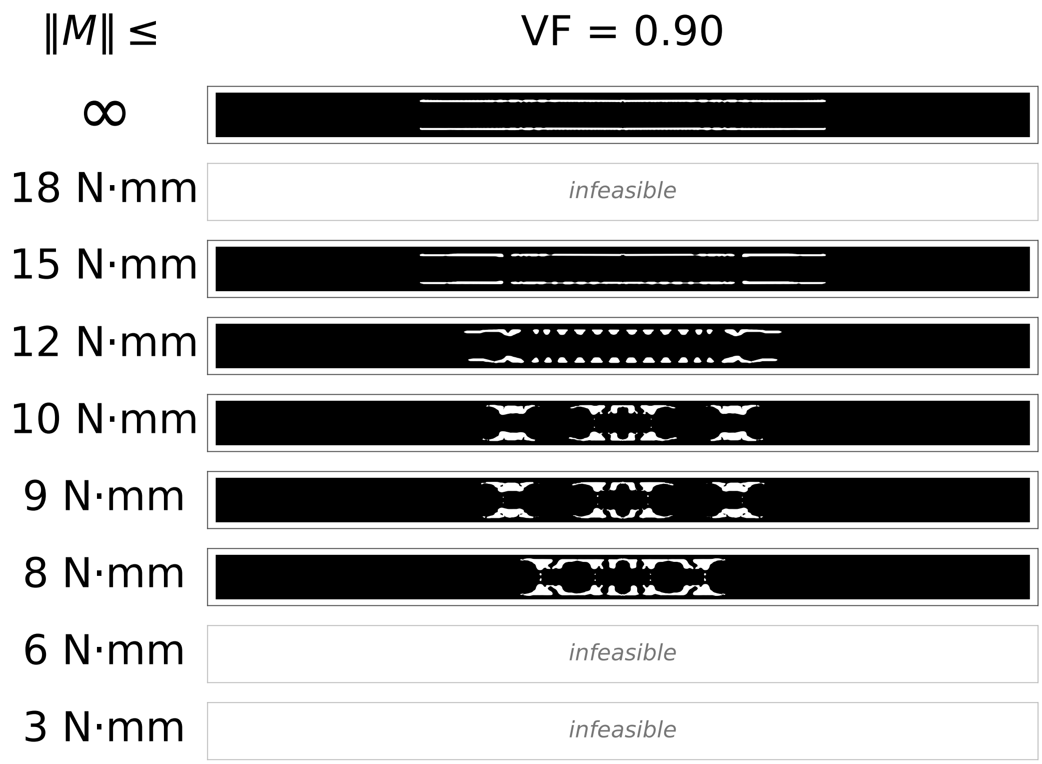

Figure D.5: Optimized designs for $d = 0.50$ at $V_f = 0.90$. The same grid and rendering conventions apply as in Figure D.1.

Figure D.6: Optimized designs for $d = 0.50$ at $V_f = 0.80$. The same grid and rendering conventions apply as in Figure D.1.

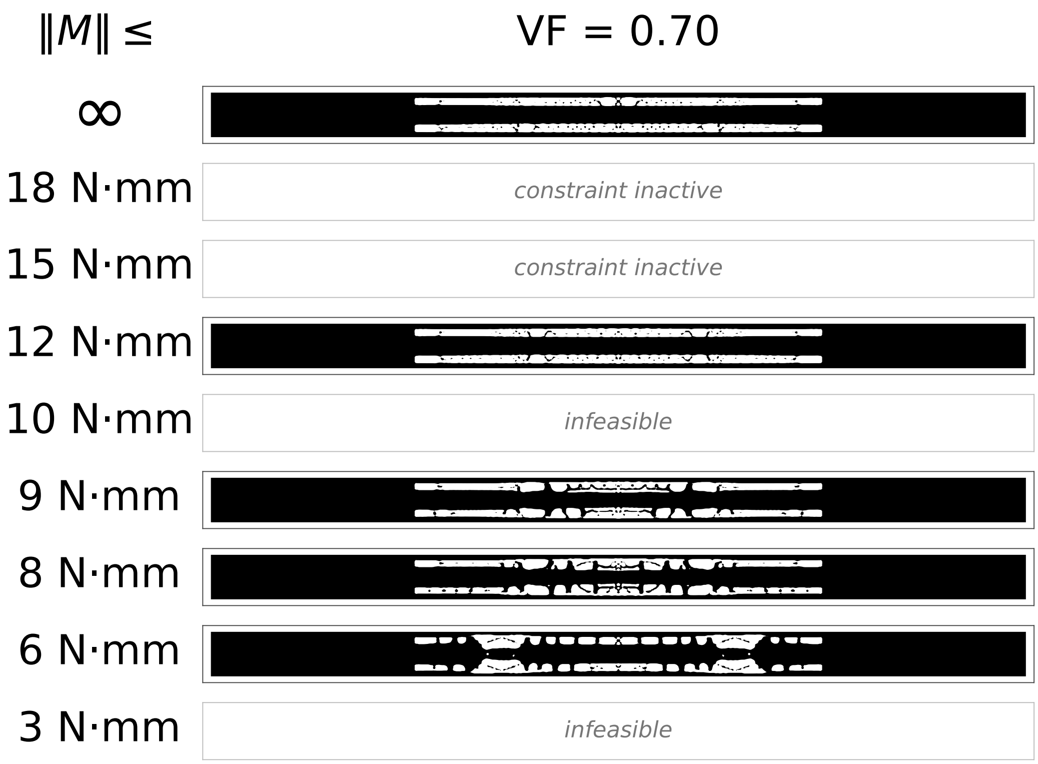

Figure D.7: Optimized designs for $d = 0.50$ at $V_f = 0.70$. The same grid and rendering conventions apply as in Figure D.1.

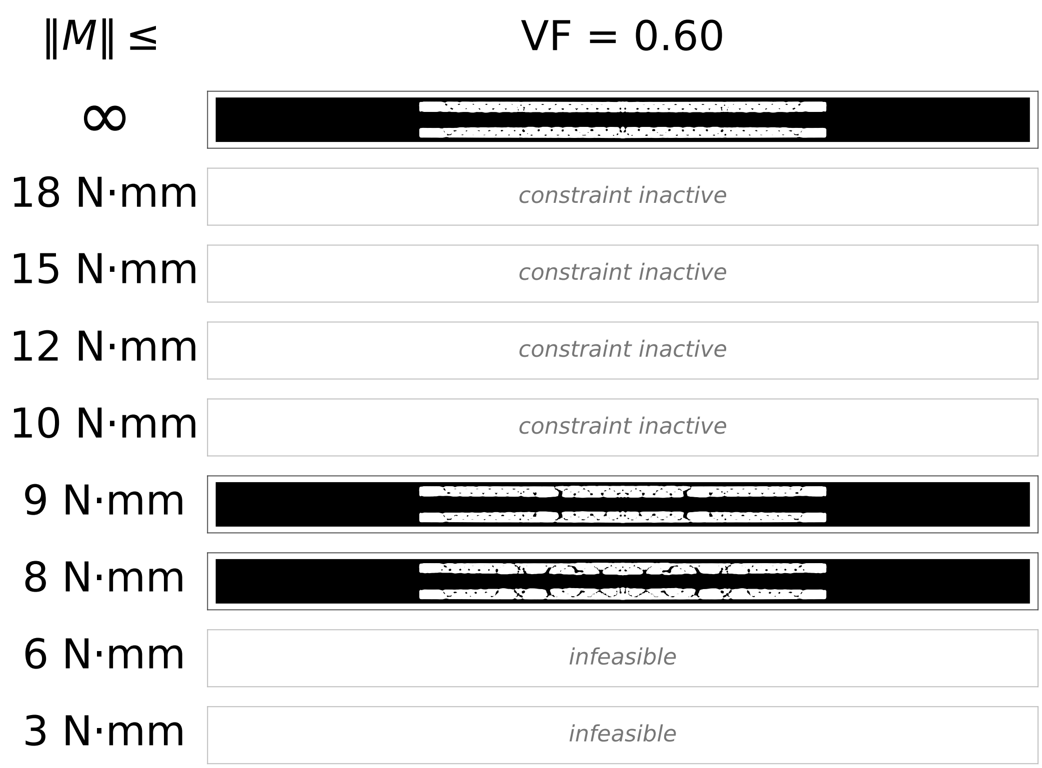

Figure D.8: Optimized designs for $d = 0.50$ at $V_f = 0.60$. The same grid and rendering conventions apply as in Figure D.1.

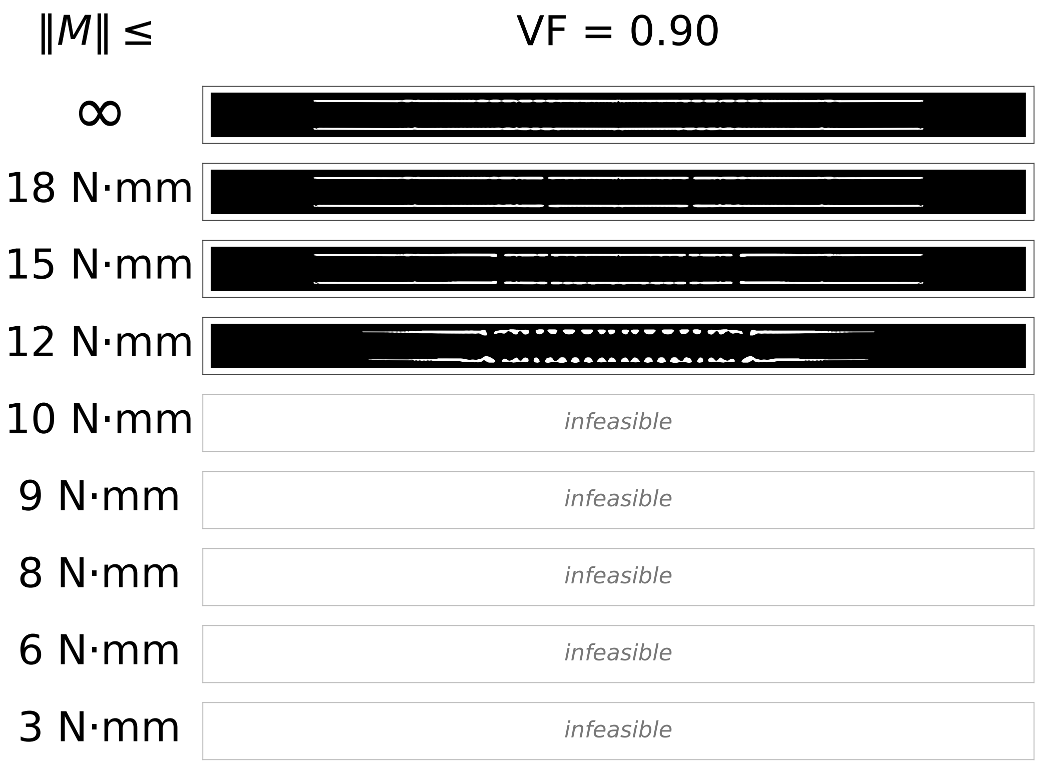

Figure D.9: Optimized designs for $d = 0.75$ at $V_f = 0.90$. The same grid and rendering conventions apply as in Figure D.1.

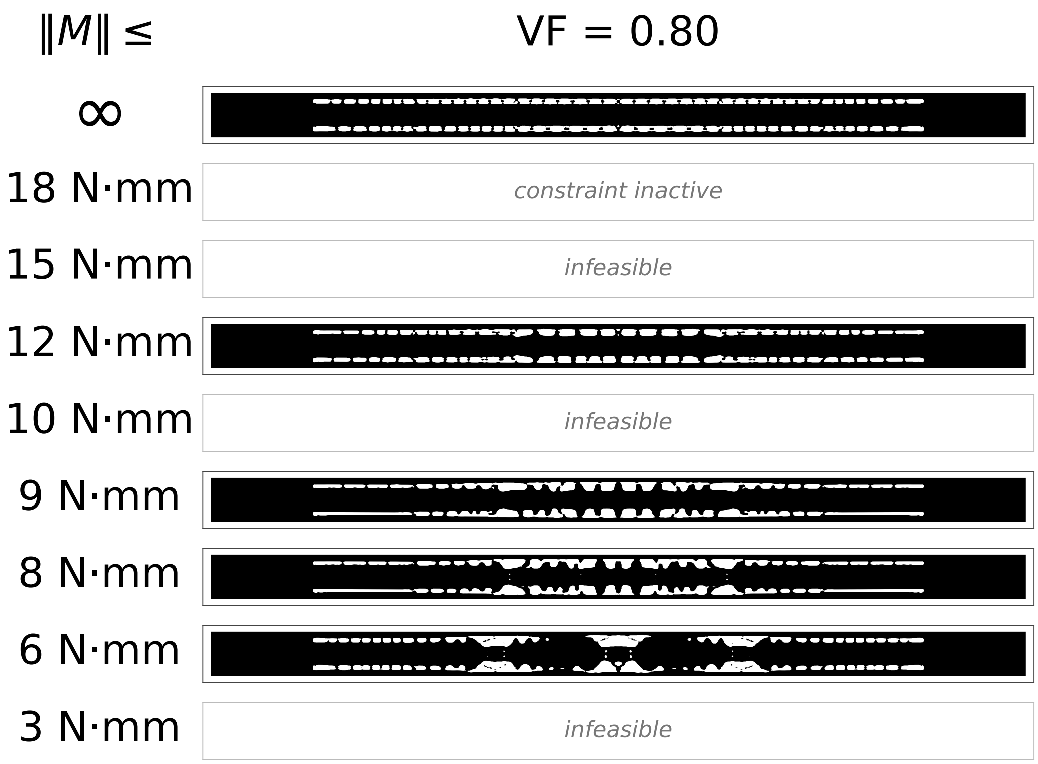

Figure D.10: Optimized designs for $d = 0.75$ at $V_f = 0.80$. The same grid and rendering conventions apply as in Figure D.1.

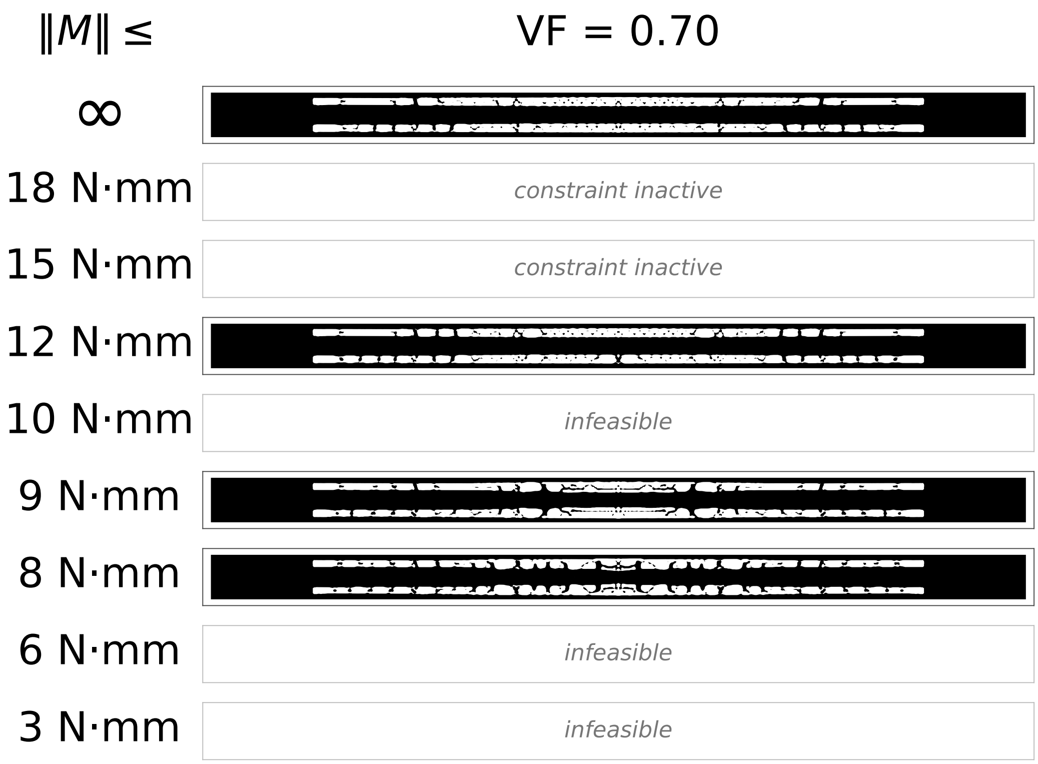

Figure D.11: Optimized designs for $d = 0.75$ at $V_f = 0.70$. The same grid and rendering conventions apply as in Figure D.1.

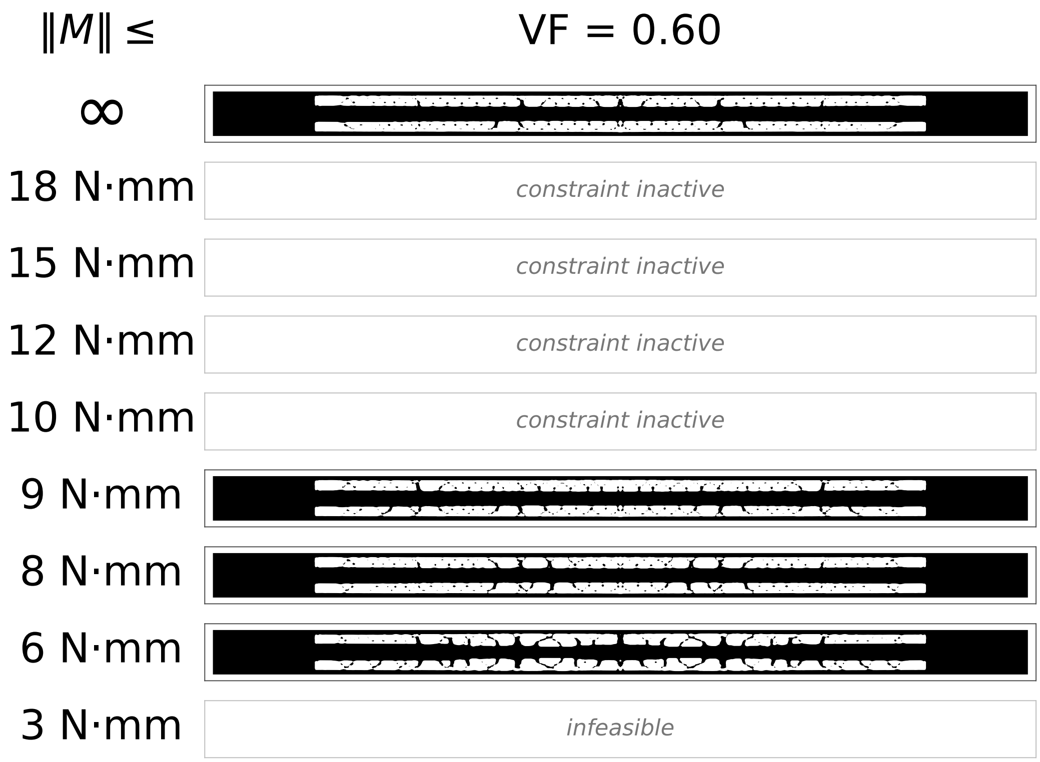

Figure D.12: Optimized designs for $d = 0.75$ at $V_f = 0.60$. The same grid and rendering conventions apply as in Figure D.1.

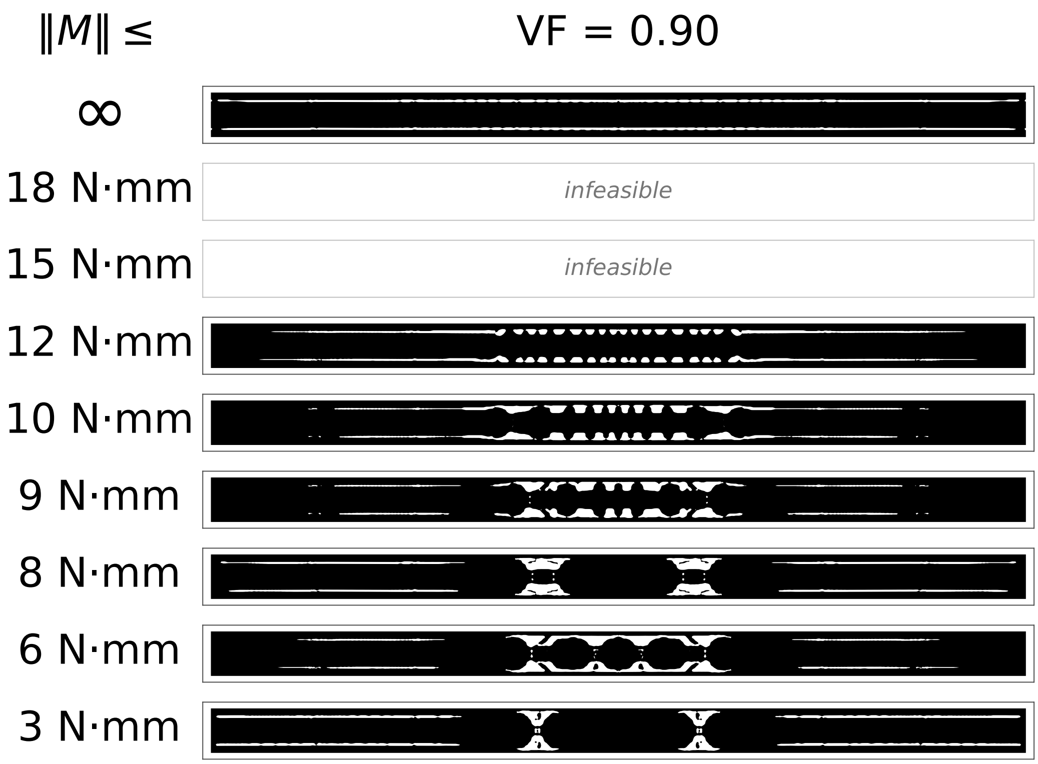

Figure D.13: Optimized designs for d = 1.00 (full-strip design region) at V_f = 0.90. The same grid and rendering conventions apply as in Figure D.1.

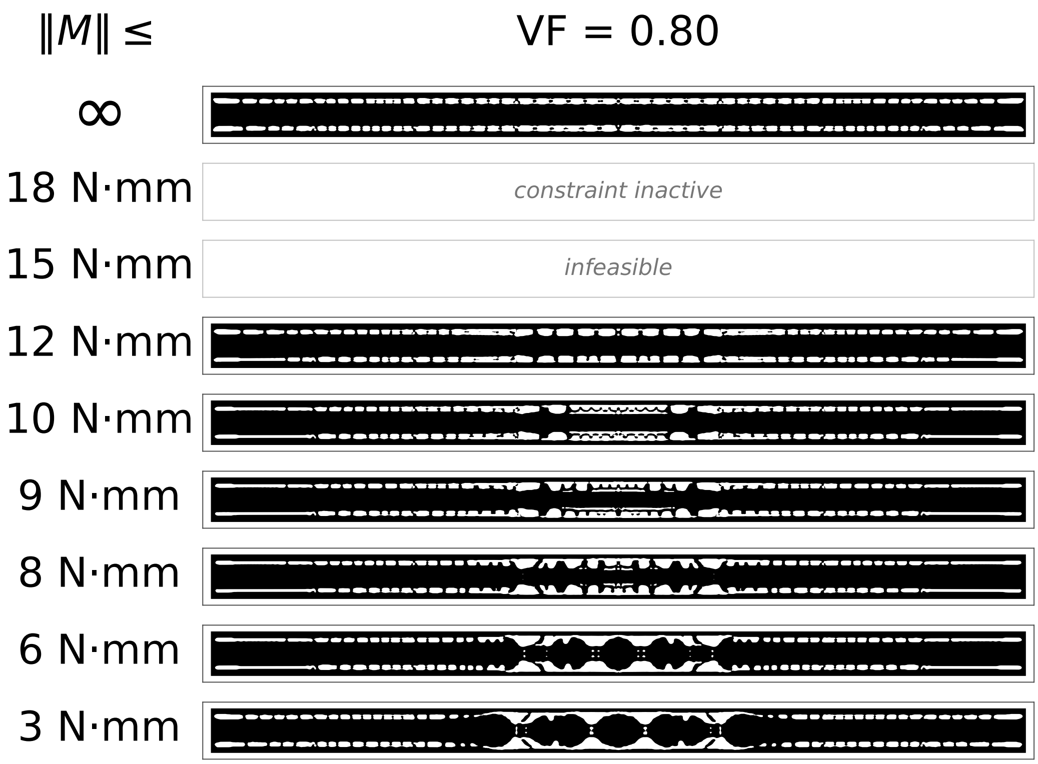

Figure D.14: Optimized designs for $d = 1.00$ (full-strip design region) at $V_f = 0.80$. The same grid and rendering conventions apply as in Figure D.1.

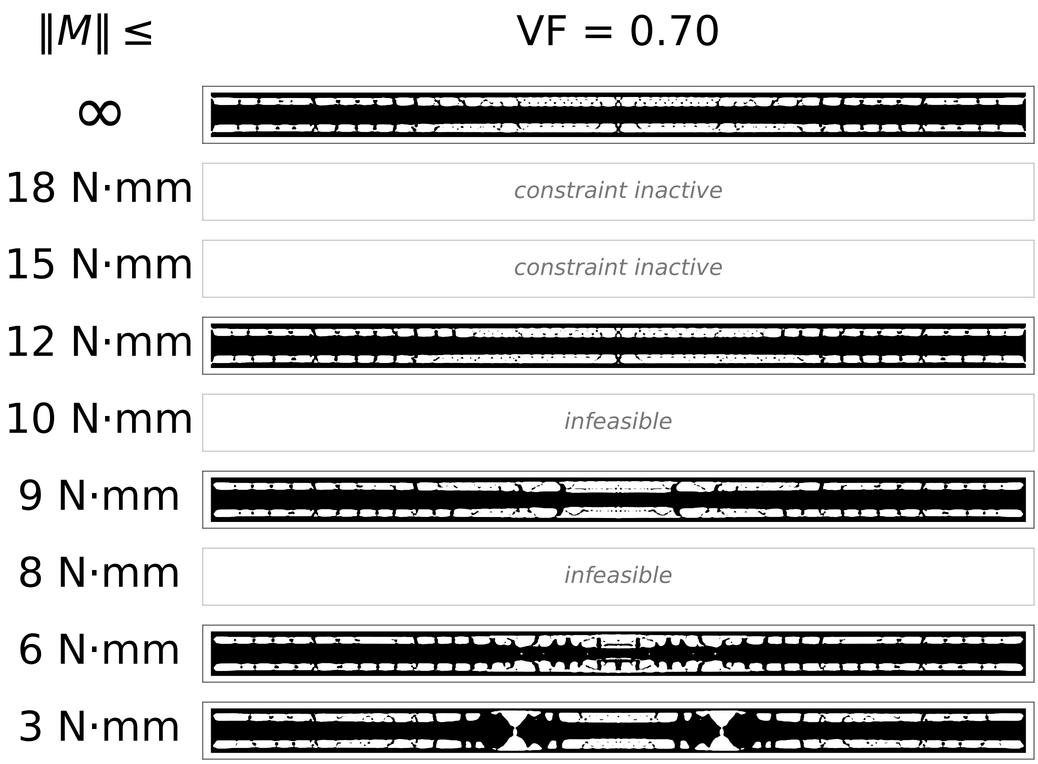

Figure D.15: Optimized designs for $d = 1.00$ (full-strip design region) at $V_f = 0.70$. The same grid and rendering conventions apply as in Figure D.1.

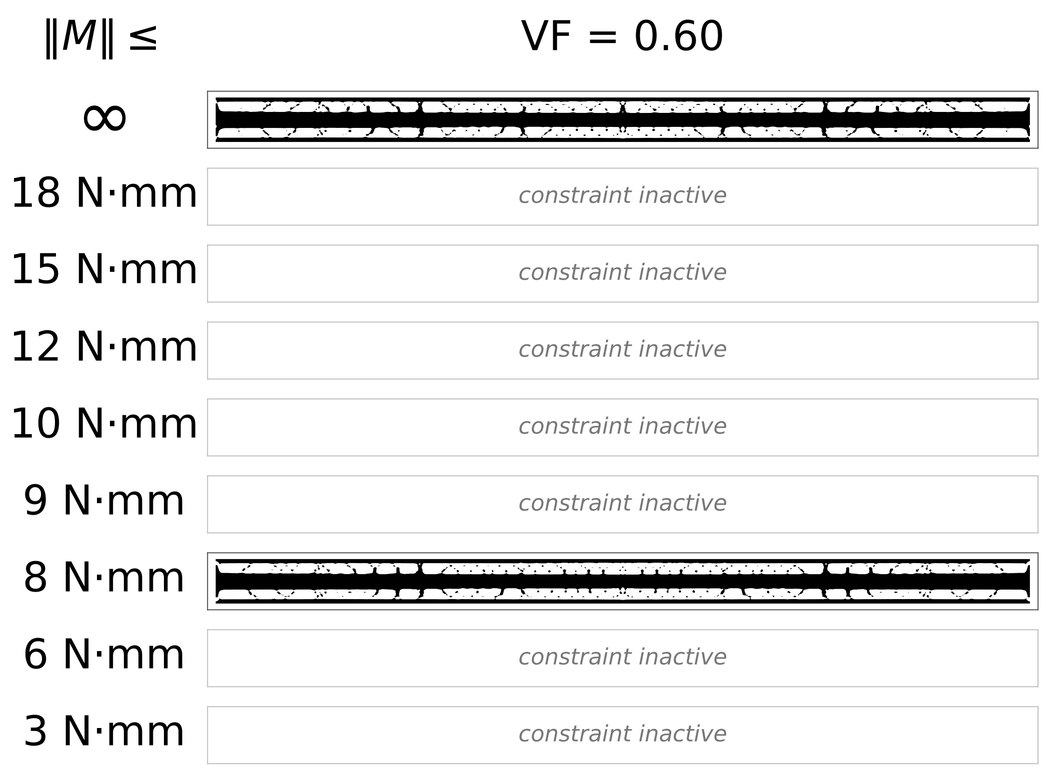

Figure D.16: Optimized designs for $d = 1.00$ (full-strip design region) at $V_f = 0.60$. The same grid and rendering conventions apply as in Figure D.1.